UNIVERSITÄTSKLINIKUM HAMBURG-EPPENDORF

Institut für Klinische Chemie und Laboratoriumsmedizin

Prof. Dr. Dr. Thomas Renné

Molecular Processes of Neutrophil Extracellular Trap Formation in Thrombo-Inflammation

Dissertation

zur Erlangung des Doktorgrades PhD
an der Medizinischen Fakultät der Universität Hamburg

vorgelegt von:

Hanna Englert
aus Mainz

Hamburg 2023

Angenommen von der
Medizinischen Fakultät der Universität Hamburg am: 12.04.2024

Veröffentlicht mit Genehmigung der
Medizinischen Fakultät der Universität Hamburg

Prüfungsausschuss, der/die Vorsitzende: Prof. Dr. Dr. Thomas Renné

Prüfungsausschuss, zweite/r Gutachter/in: PD Dr. Mathias Gelderblom

Prüfungsausschuss, dritte/r Gutachter/in: PD Dr. Leo Nicolai

Table of Contents

Scientific papers presented in this thesis

This thesis is based on the following peer-reviewed scientific publications:

1) **<u>Englert, H.</u>**, Rangaswamy, C., Deppermann, C., Sperhake, J. P., Krisp, C., Schreier, D., Gordon, E., Konrath, S., Haddad, M., Pula, G., Mailer, R. K., Schlüter, H., Kluge, S., Langer, F., Püschel, K., Panousis, K., Stavrou, E. X., Maas, C., Renné, T., Frye, M. *Defective NET clearance contributes to sustained FXII activation in COVID-19-associated pulmonary thrombo-inflammation.* EBioMedicine. 2021 May;67:103382. doi: 10.1016/j.ebiom.2021.103382. (1)

2) Fogarty, H., Townsend, L., Morrin, H., Ahmad, A., Comerford, C., Karampini, E., **<u>Englert, H.</u>**, Byrne, M., Bergin, C., O'Sullivan, J. M., Martin-Loeches, I., Nadarajan, P., Bannan, C., Mallon, P. W., Curley, G. F., Preston, R. J. S., Rehill, A. M., McGonagle, D., Ni Cheallaigh, C., Baker, R. I., Renné, T., Ward, S. E., O'Donnell, J. S., Irish COVID-19 Vasculopathy Study (iCVS) investigators. *Persistent endotheliopathy in the pathogenesis of long COVID syndrome.* J Thromb Haemost. 2021 Oct;19(10):2546-2553. doi: 10.1111/jth.15490. (2)

3) Greinacher, A., Selleng, K., Palankar, R., Wesche, J., Handtke, S., Wolff, M., Aurich, K., Lalk, M., Methling, K., Völker, U., Hentschker, C., Michalik, S., Steil, L., Reder, A., Schönborn, L., Beer, M., Franzke, K., Büttner, A., Fehse, B., Stavrou, E. X., Rangaswamy, C., Mailer, R. K., **<u>Englert, H.</u>**, Frye, M., Thiele, T., Kochanek, S., Krutzke, L., Siegerist, F., Endlich, N., Warkentin, T. E., Renné, T. *Insights in ChAdOx1 nCoV-19 vaccine-induced immune thrombotic thrombocytopenia.* Blood. 2021 Dec 2;138(22):2256-2268. doi: 10.1182/blood.2021013231. (3)

4) **<u>Englert, H.</u>**, Göbel, J., Khong, D., Omidi, M., Wolska, N., Konrath, S., Frye, M, Mailer, R. K., Beerens, M., Gerwers, J. C., Preston, R. J. S., Odeberg, J., Butler, L. M., Maas, C., Stavrou, E. X., Fuchs, T. A., Renné, T. *Targeting NETs using dual-active DNase1 variants.* Front. Immunol. 2023 May;14:1181761. doi: 10.3389/fimmu.2023.1181761. (4)

1. Introduction

1.1 Inflammation

Inflammation is a part of the body's defense mechanism to fight pathogens but it also contributes to the resolution of injuries. Yet, in the case of uncontrolled and unresolved inflammation, tissue damage continues to surge, which can have detrimental effects on the host (5). The acute phase reaction orchestrates the release of pro-inflammatory cytokines and the activation of immune and vascular systems as the first reaction to infection, trauma, and inflammatory processes. However, excessive release of pro-inflammatory cytokines as a cytokine storm may lead to a hyperactive host immune response which can cause multi-organ failure and eventually death (6).

1.2 Neutrophils

Neutrophils are the most abundant leukocytes in circulation and key players of the innate immune response. Neutrophils efficiently fight pathogens during acute inflammatory responses and have been shown to be involved in chronic inflammatory processes (7). Due to their immune functions and short lifespan of 6-8 h in the circulation, neutrophils are continuously produced in the bone marrow at a rate of about 10^{11} cells per day in humans, in a process termed granulopoiesis (8).

Granulopoiesis is the part of haematopoiesis that leads to the production of blood cells including neutrophils, eosinophils, and basophils (9). During maturation of neutrophils, the neutrophil precursors myeloblasts, promyelocytes, and young myelocytes proliferate, whereas cell division ceases at later stages during the transition of myelocytes and metamyelocytes (9). Neutrophil granules emerge in a stepwise process with azurophilic (primary) granules appearing at first in myeloblasts and promyelocytes, which contain a large, round nucleus (9). In the next step, specific (secondary) granules are produced in myelocytes and metamyelocytes and the round nucleus changes into a kidney-like shape (9). Gelatinase (tertiary) granules form during the transition from metamyelocytes to band (or rod-nucleated) neutrophils, with the nucleus forming a band-like shape (9). During the final step of granulopoiesis, ficolin-1 granules and secretory vesicles develop and the neutrophil acquires its characteristic segmented polymorphic nucleus (9). Mature, fully differentiated neutrophils are

released into circulation under physiological conditions, orchestrated by the signaling of the endogenous cytokine granulocyte colony stimulating factor (G-CSF) (8, 10). Band neutrophils may also be released into the circulation during acute inflammation (11). G-CSF induces the egression of mature neutrophils from the bone marrow by the inhibition of C-X-C motif chemokine ligand (CXCL) 12 on bone marrow stromal cells and a reduced expression of C-X-C chemokine receptor (CXCR) 4 on myeloid cells (8). During an inflammatory response, G-CSF expression is upregulated to increase recruitment of neutrophils to the site of injury (12). Neutrophil activation during acute inflammation aids in tissue regeneration, whereas persistent activation may cause prolonged inflammation and collateral damage to the host (13). Neutrophils enhance pro-inflammatory processes through degranulation, release of reactive oxygen species (ROS), interactions with platelets, and the formation of Neutrophil Extracellular Traps (NETs), a process also termed NETosis (5).

1.3 Neutrophil Extracellular Traps

1.3.1 NET composition

NET formation was first described in 2004 by Brinkmann and colleagues. The process is characterized as the release of nuclear derived DNA fibers, decorated with histones and granular proteins, into the extracellular space to entrap and neutralize invading pathogens (14). The structure of NETs in scanning electron microscopy images appears as 15-17 nm stretches of double-stranded DNA (dsDNA) and histones, intermitted by 25 nm sections of comprising granular proteins (14, 15). The nucleosomal regions contain the core histones H2A, H2B, H3, and H4, which make up around 70% of all NET-associated proteins. Only trace amounts of the linker histone H1 are bound to NETs, reflecting the decondensed state of the chromatin (14, 15). Granular proteins make up 20% of proteins attached to NETs and are derived from neutrophil azurophilic granules, i.e., myeloperoxidase (MPO), and neutrophil elastase (NE), as well as secondary and tertiary granules, containing e.g., lactoferrin and gelatinase (14).

Upon an inflammatory response, the host must promptly remove NETs due to the locally high concentration of active, toxic molecules that, besides eliminating pathogens, can damage the tissue. The resolution of uncontrolled inflammation is necessary to maintain or recover homeostasis and prevent systemic inflammatory and

autoimmune reactions. Clinical and experimental models suggest that NETs contribute to the pathogenesis of cystic fibrosis (16, 17), systemic lupus erythematosus (SLE) (18), rheumatoid arthritis (19), cancer metastases (20, 21), atherosclerosis (22), thrombotic microangiopathies (23), and acute coronary syndrome (24).

1.3.2 NET formation

Neutrophil stimulation for $\geq$ 2 h with PMA activates lytic NETosis and led to the initial discovery of NETs (**Fig. 1**, lower panel) (14, 25). There are many experimental stimuli that are capable of triggering lytic NETosis including immune complexes (26), cholesterol crystals (27), calcium ionophores ionomycin (28) or the Ca^{2+}-ionophore A23187 (29), *Candida albicans* (*C. albicans*) hyphae (30), or lipopolysaccharide (LPS) from bacterial sources (29). Stimulation with A23187 catalyzes the transfer of Ca^{2+} from the extra- into the intracellular space, and mobilizes Ca^{2+} from the endoplasmic reticulum, resulting in an increase of cytoplasmatic $[Ca^{2+}]_i$. Increase in $[Ca^{2+}]_i$ as well as PMA stimulation leads to protein kinase C (PKC) activation. PKC activation stimulates the mitogen-activated protein kinase (MAPK)- extracellular-signal-regulated kinase (ERK) and the nicotinamide adenine dinucleotide phosphate hydrogen (NADPH) oxidase signaling pathways resulting in ROS generation (31). Additionally, Ca^{2+} accumulation in the mitochondrial matrix of the neutrophil activates mitochondrial pores that release mtROS (32). ROS and mtROS in turn activate PAD4, NE, and MPO, which propagate chromatin decondensation by citrullination and cleavage of histones, as well as break-down of the nuclear membrane (33).

NET formation is divided into two main processes, vital NET release or lytic NET formation resulting in cell death (34). In contrast to vital NET formation, lytic NETosis is dependent on ROS generation, requires prolonged stimulation (hours range) and results in cell death. The stimulus determines which NET-mechanism is initiated. Lytic NETosis is mostly triggered by stimulation with the plant-derived mitogen phorbol-12-myristate-13-acetate (PMA), whereas vital NETosis has primarily been associated with microbial specific stimuli (35). Vital NET release was described more recently and can be induced within minutes independently of cell death (36, 37) (**Fig. 1**, upper panel). Gram-positive bacteria, e.g., live *Staphylococcus aureus* (*S. aureus)* induce vital NET release *in vivo* via both Toll-like receptor (TLR) 2 and complement receptor 3 (36).

Gram-negative bacteria and their bacterial cell wall component LPS also induce vital NET formation (35). Vital NET release was first described in a system where LPS-activated platelets activated neutrophils in a TLR4-dependent manner (38). Additionally, platelets trigger NET formation through the binding of platelet P-selectin to P-selectin glycoprotein ligand-1 (PSGL-1) on neutrophils (39). During vital NETosis, NETs get packaged into vesicles which are released into the extracellular space (36). Released NET vesicles ensnare bacteria in the extracellular environment and the vital neutrophil may still perform certain functions, e.g., phagocytosis and chemotaxis even to the point of becoming anuclear (37).

Vital NET formation has been described to proceed independently of oxidants, although recent studies suggested the involvement of different sources of reactive oxygen species (ROS) (36). A study found that vital NET formation may be dependent on ROS production by mitochondria (mtROS) and Ca^{2+} influx via the small-conductance calcium-activated potassium (SK) channel member 3 (SK3), but the exact role of mtROS in NET formation has not been completely elucidated (40). Peptidyl-arginine deiminase 4 (PAD4) gets activated downstream of TLRs and complement receptors and catalyzes the conversion of arginine to citrulline residues resulting in the citrullination of histones. Citrullination reduces the net positive charge of histones and amplifies chromatin decondensation by lowering charge-charge interaction between histones and DNA (41-43). However, the importance of PAD4 in NET formation seems to be stimulus- and species-dependent (29, 30, 44). Additionally, NE is released from azurophilic granules into the cytosol, where it translocates into the nucleus and aids in further unfolding of the chromatin by histone cleavage (45, 46).

Binding of pathogens or pathogenic antigens induce signaling via TLRs and the attached adaptor protein myeloid differentiation factor 88 (MYD88) which acts as a central hub for inflammatory responses (47, 48). TLRs and MYD88 activation augments ROS generation as a response to infectious stimuli in macrophages and neutrophils (49, 50). The TLR-MYD88 pathway activates the MAPK and nuclear factor kappa-light-chain-enhancer of activated B cells (NF-κB) signaling pathways (51). NF-κB translocates to the nucleus and regulates the transcription of components of the inflammasome, pro-interleukin (IL)-1ß, pro- IL-18 and pro-Gasdermin D, which then are cleaved by caspases resulting in their active forms (52, 53). Gasdermin D

(GSDMD) was identified as the key executioner of programmed lytic cell death (pyroptosis) in macrophages. Upon activation of the canonical (mediated by nucleotide-binding domain–like receptors (NLRs), absent in melanoma 2–like receptors, pyrin, and caspase-1) or non-canonical inflammasome (driven by caspases-4/5 in humans or caspase-11 in mice) (54) GSDMD gets proteolytically cleaved at a proteolysis-sensitive linker region between the N- and C-terminal domain (55). The N-terminal GSDMD fragment translocates to the plasma membrane to form pores, resulting in membrane rupture and pyroptotic cell death (56). Inflammasome and GSDMD activation contribute to membrane breakdown during lytic NET release in bacterial and viral infection models (57-59). The prevailing view is that GSDMD aids in the breakdown of intracellular membranes and the plasma membrane (58, 60, 61). Consequently, the decondensed chromatin decorated with granular enzymes and cytosolic proteins extrudes as NETs into the extracellular space. However, another study found that GSDMD deficient murine neutrophils formed NETs to the same extent as wild-type (WT) mouse neutrophils, challenging the importance of GSDMD for NETosis (62). It has not yet been identified whether GSDMD contributes to vital NET release. It is hypothesized that upon nuclear envelope budding, NET-filled vesicles are released into the extracellular space by exocytosis where they can ensnare bacteria despite maintaining their structure and cellular integrity (36, 37). Vital NET formation seems to be more important for fighting infections than resolving sterile injury, because neutrophils stay alive and functional, performing classical functions in host response, including phagocytosis and chemotaxis (63).
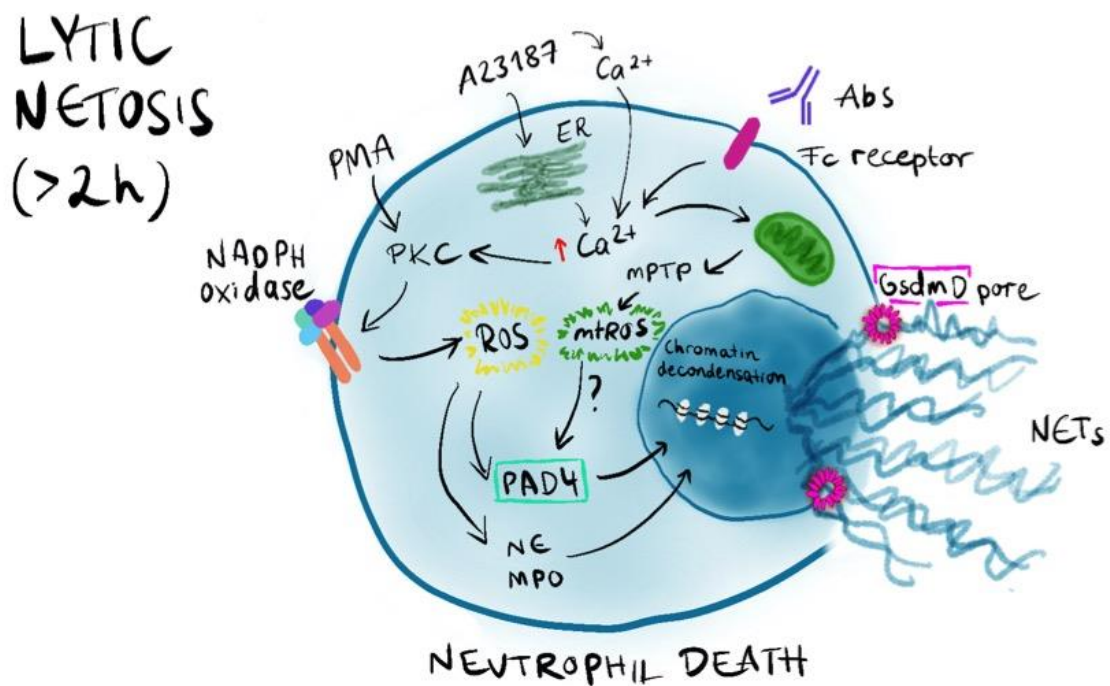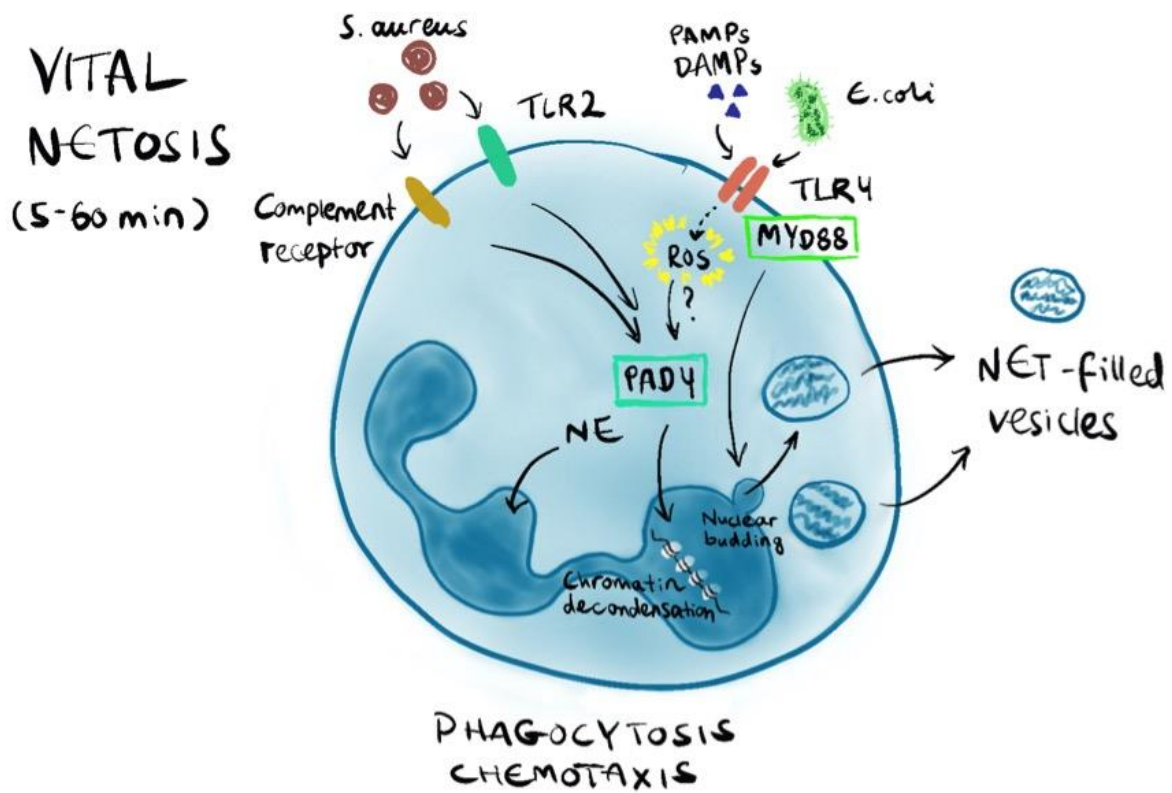
Figure 1. Proposed stimuli and pathways driving vital and lytic NET formation. NETosis is the process of NET release into the extracellular space and can be divided into vital (upper panel) and lytic (lower panel) NET formation:

Vital NETosis occurs rapidly within a 5 – 60 min timeframe without cell lysis, e.g. bacteria such as Gram-positive *S. aureus* binding activates toll-like receptor 2 (TLR2) or complement receptor signaling which in turn activates the Ca^{2+} dependent enzyme peptidyl arginine deiminase 4 (PAD4), independent of

NADPH oxidase-generated reactive oxygen species (ROS). PAD4 citrullinates histones, thereby supporting chromatin decondensation. Alternatively, Gram-negative bacteria, e.g. *E. coli*, or pathogen- or danger-associated molecular patterns (PAMPs, DAMPs) such as lipopolysaccharides (LPS), stimulate ROS generation and in turn PAD4 activation. However, vital NET formation can also proceed in the absence of oxidants. Binding of bacteria or PAMPs to TLRs activates myeloid differentiation factor 88 (MYD88) and downstream inflammatory responses. Like lytic NETosis, PAD4 triggers chromatin decondensation and neutrophil elastase (NE) translocates to the nucleus to cleave histones. NETs are enclosed in nuclear vesicles (nuclear budding) and released from viable neutrophils via exocytosis while cell membrane integrity is maintained.

Lytic NETosis is initiated by various stimuli including phorbol 12-myristate 13-acetate (PMA), calcium ionophore A23187, or (auto-)antibodies (Abs) within 2 – 4 h of stimulation, and eventually leads to death of the neutrophil. Calcium ionophore liberates Ca^{2+} from the endoplasmic reticulum (ER) that increases intracellular $[Ca^{2+}]$ that in turn opens calcium channels in the plasma membrane allowing for Ca^{2+} influx into the cytoplasm. A23187 also forms pores in the plasma membrane that mediate Ca^{2+} influx from the extra- into the intracellular space. Accumulation of Ca^{2+} in the mitochondrial matrix activates non-selective mitochondrial permeability transition pores (mPTP) and the release of mitochondrial ROS (mtROS). Increase of $[Ca^{2+}]_i$ and PMA activate protein kinase C (PKC), which activates NADPH oxidase and ROS production. ROS in turn activate PAD4, MPO and NE to translocate to the nucleus where they promote chromatin unfolding and nuclear membrane disruption. Upon nuclear membrane rupture, liberated chromatin mixes with cytosolic components such as granular proteins. GSDMD then promotes granular, nuclear, and plasma membrane rupture. Finally, the plasma membrane ruptures, and the mature NET gets extruded resulting in death of the neutrophil.

1.3.3 NETs in thrombo-inflammation

The intricate interplay between the innate immune system and coagulation is defined as immunothrombosis. Immunothrombosis entails interconnected processes that are important to limit the systemic dissemination of pathogens (64). Aberrant and excessive immunothrombosis leads to thrombo-inflammation involving the formation of micro- and macrovascular thrombi, resulting in tissue ischemia and potentially irreversible organ damage. An important event in thrombo-inflammation is the reciprocal activation of platelets and neutrophils, which augments clotting and vessel occlusion. Platelet-neutrophil interactions contribute not only to the formation but also the propagation of the clot e.g. by activating NETosis (65). NETs serve as a platform for platelet adhesion and thereby boost their prothrombotic properties (66). Platelets adhere and aggregate on von Willebrand factor (vWF) bound to the DNA backbone of NETs and get activated by histones, leading to increased clot formation (65, 67, 68). The granular enzyme NE degrades the main inhibitor of the extrinsic coagulation

pathway, tissue factor pathway inhibitor (TFPI), yielding increased tissue factor activity and thrombin formation (69). Furthermore, the negatively charged DNA of NETs serves as a surface for the binding and activation of zymogen factor XII (FXII) into FXIIa (contact activation mechanism), thereby initiating the intrinsic or contact pathway of coagulation (65, 70). Research showed that the DNA backbone of NETs was decorated with zymogens FXII and FXI and that NETs were indispensable for thrombus propagation in a mouse model of deep vein thrombosis (DVT), by binding and activating FXII (65, 70). However, the exact mechanisms on how NETs perform their prothrombotic activity *in vivo* are still under debate (71). Overall, NETs serve as a key element between thrombosis and inflammation by acting as a matrix for platelet adhesion, an activator of the coagulation system, and promoter of pro-inflammatory reactions (64).

Thrombo-inflammation received special attention during the global COVID-19 pandemic. COVID-19 is caused by severe acute respiratory syndrome coronavirus 2 (SARS-CoV-2), which has infected over 760 million people worldwide and caused more than 6.9 million confirmed deaths as of August 15, 2023 (72). Pulmonary inflammation and thrombotic occlusions of lung veins and capillaries are hallmarks of severe COVID-19 infection, causing tissue ischemia and respiratory failure. Several prothrombotic markers, including high fibrinogen and D-dimer levels, prolonged prothrombin time (PT), and activated partial thromboplastin time (aPTT), have been found in plasma from COVID-19 patients suggesting consumption of coagulation factors and/or disseminated intravascular coagulation (DIC) (73-75). SARS-CoV-2 enters host alveolar epithelial and vascular endothelial cells via its cell-entry receptor angiotensin-converting enzyme 2 (ACE2), which stimulates the exposure of vWF on the endothelial surface, favoring the recruitment and activation of platelets and neutrophils to the site of endothelial activation (2, 76-78). COVID-19 patients showed increased levels of platelet-derived chemokines CXCL4 and C-C motif chemokine ligand CCL5, and SARS-CoV-2 was also found to enter neutrophils via ACE2 and transmembrane serine protease 2 (TMPRSS2). SARS-CoV-2 directly induced NET release from healthy neutrophils via the activation of ACE2 and TMPRSS2 on neutrophils (79, 80). The pulmonary microcirculation in COVID-19 lungs displayed high amounts of NETs and activated platelets (81). COVID-19 severity was also positively correlated with levels of circulating extracellular DNA, citrullinated histone H3 (H3cit),

and MPO-DNA complexes, markers of NET formation (82). Taken together, COVID-19 patients display a disproportionate activation of platelets and neutrophils leading to coagulopathy, respiratory failure, and a systemic prothrombotic state with high mortality (64).

Vaccines to fight the mortality of SARS-CoV-2 infection were the most urgently needed countermeasure against the COVID-19 pandemic. From December 2020 through March 2021, the European Medicines Agency (EMA) approved four vaccines, including the adenoviral vector-based vaccine ChAdOx1 nCov-19 (AstraZeneca). As of March 10, 2021, 30 vaccine recipients developed thrombotic complications and thrombocytopenia, among approximately 5 million people that had received the ChAdOx1 nCov-19 vaccine (83). Complications arose in healthy individuals 1-3 weeks following vaccination with ChAdOx1 nCov-19. Adverse reactions included a combination of thrombocytopenia with cerebral venous sinus thrombosis (CVST), splanchnic vein thrombosis, pulmonary embolism (PE), and thrombosis in other vascular beds. The rare but severe thrombo-inflammatory adverse reaction included the activation of platelets, neutrophils, and the coagulation system leading to high mortality from thrombosis or secondary hemorrhage (84). Vaccinated patients showed various symptoms including headaches, abdominal pain, back pain, focal neurological symptoms, dyspnea, swelling and redness of a limb, or pallor and coldness of a limb (84). The novel disorder was termed vaccine-induced immune thrombotic thrombocytopenia (VITT) and is characterized by high immunoglobulin G (IgG) antibody titers directed against platelet factor 4 (PF4, CXCL4) similarly to heparin induced thrombocytopenia (HIT) (85).

1.3.4 NET clearance

NETs need to be cleared in a timely manner to protect the host from excessive inflammation, the presentation of auto-antigens, and detrimental tissue damage (86). Knowledge on the degradation of NETs in tissues is still scarce. Haider *et al.* suggests that serum deoxyribonucleases (DNases) cleave extracellular DNA followed by degradation by macrophages (87). DNases belong to the family of endonucleases that specifically degrade DNA. DNases degrade DNA derived from endogenous and exogenous sources by the hydrolysis of phosphodiester bonds (88-90). Endogenous

nuclear and mitochondrial DNA arising from various programmed cell death processes is the major target for DNases to avoid aberrant activation of the immune system (88-91). DNA clearance by DNases restricts inflammatory responses, and maintains tissue homeostasis in humans, mice, and other organisms. DNases emerged as key enzymes in the clearance of NETs *in vivo* (18). Human and murine serum contains DNase1 and DNase1-like 3 (DNase1L3) that clear intravascular NETs during septicemia or sterile neutrophilia (92). Deficient DNase1L3 expression augmented NET-driven tumor cell invasion in an *in vitro* and allograft model of diabetic hepatocellular carcinoma (93). In addition to DNases, 3'-exonucleases (TREX family) cleave DNA remnants from cell death processes, DNA replication, repair, and recombination pathways (94). Macrophages eliminate damaged, dead cells and cell debris and are capable of engulfing NETs in an active, endocytic process *in vitro* (95). Preprocessing NETs with DNase1 and/or opsonization with recombinant or endogenous complement factor 1q (C1q) facilitated NET clearance by macrophages. Defective dismantling of NETs may cause disorders such as anemia, parakeratosis, cataracts, and SLE (96-99). DNases may also be functionally impaired due to the presence of DNase inhibitors or the generation of anti-DNase antibodies (18). Furthermore, DNase activity is necessary to prevent the formation of intravascular thrombi containing NETs (100). DNase1- and DNase1L3 double deficient mice rapidly died from multiorgan failure due to NET-containing intravascular clots (92).

1.4 Therapeutic applications of DNases

1.4.1 DNase protein family

The DNase family comprises two distinct groups, DNase1 members - DNase1, DNase1-like 1 (DNase1L1), DNase1-like 2 (DNase1L2), DNase1L3 - and DNase2 members - DNase2a, DNase2b, L-DNaseII - which mainly differ in structure, tissue expression, substrate affinity, and catalytic properties (101). DNase1 requires divalent cations, its enzymatic activity peaks at neutral pH, and it produces DNA cleavage products with 5'-P and 3'-OH ends. In contrast DNase2 is not dependent on cofactors, has optimal enzymatic activity at an acidic pH, and generates 5'-OH and 3'-P ends (102-106). Expression pattern of DNase1 and DNase2 families is cell type specific: DNase1 is predominantly expressed by exocrine cells in the gastrointestinal tract, salivary glands, kidneys, and thymus and is secreted into the plasma (107, 108).

DNase1L3 is primarily expressed by liver- and spleen-resident macrophages and dendritic cells and also gets secreted into the plasma just like DNase1 (102, 109-112). Our laboratory has originally shown that DNase1 and DNase1L3 are essential to degrade NETs in circulation in experimental mouse models of sterile neutrophilia and septicemia (92). Thus, DNase1 and DNase1L3 protect against the deleterious effects of intravascular NETs and prevent the host from hyperinflammation, immunothrombosis, and auto-immune reactions (18, 92).

Deficiency in DNase1 family members prolongs the half-life of cell-free DNA and NETs, contributing to the formation of anti-dsDNA antibodies and the development of autoimmune diseases, including SLE, lupus nephritis and vasculitis (18, 107, 113). Congenital DNase1L3 deficiency in humans underlies pediatric-onset SLE (114), whereas reduced DNase1L3 activity and polymorphisms in DNase1L3 and DNase1 genes are associated with adult-onset SLE (111, 113, 115-117). Supporting a role of DNases for autoimmunity, DNase1 or DNase1L3 deficient mice show lupus-like symptoms with anti-nuclear antibody-positive glomerulonephritis, and kidney deposition of immune complexes and complement factor C3 (107).

In 1994, Genentech/ Roche marketed U.S. Food and Drug Administration (FDA)-approved recombinant human DNase1 under the name Dornase alfa/ Pulmozyme as a first-line treatment against the respiratory disease cystic fibrosis (CF). Pulmozyme is provided as mucolytic inhalation therapy where it digests DNA in the alveolar space, thereby reducing mucus viscosity and improving gas exchange and oxygenation in CF patients (118-120). It is also used off-label in patients suffering from asthma, atelectasis, chronic lung diseases, and COVID-19 infection (94, 121, 122).

1.4.2 Structure of DNase1 and DNase1L3

The human DNase domain houses the enzyme's active site, which entails two histidine residues, His134 and His252, crucial for the catalytic activity of all members of the DNase1 and DNase2 families (123). The catalytic activity of DNase1 is mainly directed toward non-complexed DNA, such as plasmid and bacterial DNA; as compared to DNase1L3, which preferentially digests nuclear DNA or chromatin, the complex of DNA and histones found in eukaryotic cells (111, 112, 124). Human, but not murine, DNase1L3 has two nuclear localization sites (NLS1, NLS2), that target the enzyme to

the nucleus during programmed cell death, to enable the degradation of nuclear DNA (125). DNase1 is potently inhibited by monomeric actin, while DNase1L3 does not comprise actin-binding sites causing a resistance towards actin (124). All DNase1 family members contain a 18-22 amino acid long signal sequence upstream of the catalytic domain that mediates secretion of the proteins (106, 126). Upon cleavage of the signal sequence, DNase1 and DNase1L3 are primarily secreted into the extracellular space or the lumen of organelles (111, 127, 128).

The C-terminus is the most variable region of the DNase1 family members, with DNase1 lacking this sequence entirely, and DNase1L3 carrying a helical stretch. NLS2 is part of DNase1L3's unique C-terminal tail, which was shown to be required to degrade apoptotic microparticles, lipid vesicles filled with chromatin, and other remnants of dying cells *in vivo* (111, 112, 125). The C-terminal tail allows for penetration of lipid membranes to degrade the chromatin load within the apoptotic bodies. McCord and colleagues performed molecular dynamics simulations to determine the potential binding site of the C-terminal domain of DNase1L3 to its substrate DNA (123). DNase1L3 has a 4-fold higher activity for degrading lipid-complexed or antibody-bound DNA compared to DNase1, or C-terminal-deficient DNase1L3 (123). Thus, the highly basic C-terminal domain of DNase1L3 directly binds to dsDNA with micromolar affinity at physiological salt concentrations, but not to lipids (123) and thus mediates substrate specificity for complexed DNA. The C-terminus of DNase1L3 is also involved in the degradation of lipid-free, extracellular chromatin (111). Furthermore, NLS2 may play a role by permitting DNase1L3 to enter the nucleus before the nuclear membrane of the dying cell disintegrates. In contrast to DNase1L3, DNase1 does neither carry a C-terminal helix nor an NLS, making it unable to penetrate apoptotic microparticles (111).

2. Objectives of this study

When neutrophils come in contact with pathogens they eject NETs, extracellular networks comprised of chromatin and granular proteins from neutrophils. NETs protect from infection and activate the immune system. It has become evident that NETs are associated with a growing number of immune-mediated conditions including COVID-19 infection and need to be controlled to prevent hyperinflammatory and pro-thrombotic reactions. A severe thrombo-inflammatory condition termed VITT arose after vaccination against SARS-Cov-2 with ChAdOx1 nCov19 (AstraZeneca).

This research project aims to elucidate how the formation and degradation of NETs and its interplay with the coagulation system trigger thrombo-inflammatory reactions in COVID-19 patients and vaccinated individuals that developed VITT. Secondly, we aimed to better understand the mechanism underlying NETosis and especially the roles of PAD4 and the pore-forming protein GSDMD for vascular occlusive NET formation. A third objective aimed to engineer recombinant human DNases to improve the degradation of NETs.

Overall, my research presented in this thesis addresses the following three objectives:

1. Analysis of NET formation and degradation in COVID-19 and VITT
2. Mechanism of NET formation in mice with deficiency in PAD4 and GSDMD
3. Development of DNase1 variants with improved enzymatic properties

This work will provide insights into mechanisms of NET-driven thrombo-inflammation and the resolution thereof using engineered recombinant DNases.

3. Materials and Methods

3.1 Platelet-poor plasma from patients and healthy donors

Between March 2020 and February 2021, heparinized platelet-poor plasma samples from SARS-CoV-2 positive patients (n = 43) hospitalized at the University Medical Center Hamburg (UKE), Germany were collected. The Ethics Committee of the Hamburg Medical Association approved sample collection. The inclusion criterium was a positive SARS-CoV-2 infection assessed via polymerase chain reaction (PCR) analysis. All plasma samples were stored at -80 °C for further analysis. SARS-CoV-2 positive plasma samples were sex- and age-matched with healthy blood donor plasma samples (n = 39, Institute of Transfusion Medicine at the UKE).

Citrated platelet-poor plasma was drawn from adult long COVID patients that were enrolled in the post-COVID-19 review clinic in St James's Hospital, Dublin, Ireland, between May and September 2020. Inclusion criterium was the absence of symptoms for at least 6 weeks for non-hospitalized patients, and hospital discharge for admitted patients. Long COVID patients (n = 20) were compared to a non-hospitalized asymptomatic control group (up to n = 17, depending on the assay). All plasma samples were stored at -80 °C for further analysis. Ethical approval for plasma collection for the long COVID experiments was obtained from the St James Hospital Research Ethics Committee, Dublin, Ireland, and informed written consent was provided by all participants.

3.2 Lung tissue sections

The analyzed COVID-19 lung tissue belonged to a consecutive case study at the Institute of Legal Medicine at the UKE, investigating the first 80 COVID-19 deaths at the UKE (129). The COVID-19 patients had a SARS-CoV-2-positive PCR test from throat or lung swabs, and a DVT and PE diagnosis at the time of death. The COVID-19 lung tissue was matched on postmortem interval with non-COVID-19 patients (n = 3), who died from other causes in the intensive care unit of the UKE. Postmortem lung tissue from SARS-CoV-2 infected patients and patients with different pathologies were collected in March and April 2020 at the UKE. The Ethics Committee of the Hamburg Medical Association approved access and examination of the postmortem lung tissue.

3.3 Brain tissue sections

The analyzed VITT brain sections were retrieved from the Department for Legal Medicine at the University Medical Center Rostock. The samples belonged to a COVID-19 autopsy study. Sections from the sagittal sinus and cerebellum of both patients were analyzed.

3.4 Mice

All mice were bred on a C57BL/6 genetic background. *Dnase1$^{-/-}$* mice were provided by Dr. Markus Napirei (Ruhr-Universität Bochum, Bochum, Germany) (107) and *Dnase1l3$^{-/-}$* mice were received from Dr. Ryushin Mizuta (Tokyo University of Science, Tokyo, Japan) (130). We crossed *Dnase1$^{-/-}$* and *Dnase1l3$^{-/-}$* mice to generate *Dnase1/Dnase1l3$^{-/-}$* mice (92). *Myd88$^{-/-}$* mice were acquired from Jackson Laboratory (B6.129P2(SJL)-Myd88tm1.1Defr/J; strain 009088). *Pad4$^{-/-}$* mice were provided by Dr. Kerri A. Mowen (The Scripps Research Institute, La Jolla, CA, USA) (131). We crossed *Dnase1$^{-/-}$* and *Dnase1l3$^{-/-}$* mice (107, 130) to generate double-deficient *Dnase1/Dnase1l3$^{-/-}$* mice. We then crossed *D1/D1l3$^{-/-}$* mice with *Pad4$^{-/-}$* and *Myd88$^{-/-}$* mice to generate *Pad4/D1/D1l3$^{-/-}$* and *Myd88/D1/D1l3$^{-/-}$* triple knockout mice respectively. Genotyping confirmed gene knockouts with DNA band sizes of 275 base pairs (bp). The *Dnase1/Dnase1l3/Gsdmd$^{-/-}$* mice were generated by Irm Hermans-Borgmeyer from the Transgenic Mouse Unit at the CMNH at the UKE using CRISPR-Cas9 technology, which will be described in a separate materials and methods chapter. Genotyping confirmed gene knockouts. Primers and PCR protocols are listed in **Table 1**.

3.5 Quantification of circulating free DNA

Heparinized plasma from COVID-19 patients and VITT serum samples were 20-fold diluted in phosphate-buffered saline (PBS) (14190250, Thermo Fisher Scientific) containing 0.2% bovine serum albumin (BSA, A1470, Sigma Aldrich) and 4 mM ethylenediaminetetraacetic acid (EDTA, E3889, Sigma Aldrich). The plasma samples were stained with 1 µM of the fluorescent nucleic acid dye Sytox Green (S7020, Invitrogen), and fluorescence was recorded with a microplate reader (Tecan Spark 10M). Lambda DNA (SD0011, Invitrogen) was used to calculate the standard curve.

3.6 Myeloperoxidase concentration

20-fold diluted VITT serum and heparinized COVID-19 plasma samples were tested for levels of the neutrophil marker MPO using a commercial enzyme-linked immunosorbent assay (ELISA) kit (DY3174, Duoset R&D Systems). MPO levels were determined with a biotinylated MPO detection antibody and streptavidin-horseradish peroxidase (HRP) according to the manufacturer's protocol. The optical density was measured using a microplate reader (Tecan Spark 10M) at 450 nm.

3.7 Citrullinated histone H3 concentration

20-fold diluted VITT serum samples were tested for levels of the NET marker H3cit using a commercial H3cit ELISA kit (501620, clone 11D3, Cayman chemicals). H3cit levels were determined according to the manufacturer's protocol, using an anti-H3cit antibody and a second HRP-coupled antibody recognizing the H3 core. Absorbance was measured using a microplate reader (Tecan Spark 10M) set at 450 nm.

3.8 FXIIa analysis by chromogenic substrate assay

Isolated human neutrophils from healthy volunteers were seeded in a 96-well plate at a concentration of 10^5 cells per well in serum-free Dulbecco's Modified Eagle Medium (DMEM, 41965039, Gibco) prior to activation with 10 nM PMA (P8139, Sigma Aldrich) for 4 h at 37 °C, 5% CO_2, and humidity between 85-95%. Purified human zymogen FXII (30 μg/ml, HCXII-0155, Haematologic Technologies) was added to NETs pre-treated either with recombinant human DNase1 (10 U/ml, Pulmozyme, Roche, Germany) or buffer for 1 h at 37 °C, in the absence or presence of the FXIIa inhibitor, rHA-infestin-4 (500 μg/ml, CSL Behring) or heparin (100 U/ml, Heparin-Natrium Braun "Multi" 10,000 I.E./ml, B. Braun). In another experiment, COVID-19 plasma (n = 8) was pre-incubated with 500 ng/ml dexamethasone (D1756, Sigma Aldrich) or buffer for 1 h at 37 °C, 5% CO_2, and humidity between 85-95%, before addition to purified healthy neutrophils for 2 h to generate NETs *ex vivo*. FXIIa generation was then measured photometrically using the chromogenic substrate S-2302 (S820340, 1 mM, H-D-prolyl-L-phenylalanyl-L-arginine-p-nitroaniline dihydrochloride, Diapharma) at an absorbance wavelength of 405nm using a microplate reader (Tecan Spark 10M).

3.9 Cell culture

Human embryonic kidney (HEK) 293 cells were cultured in DMEM (41965039, Gibco) supplemented with 10% fetal bovine serum (FBS, 16250078, Gibco) and 1% penicillin-streptomycin (15140122, Life Technologies) in T75 flasks at 37 °C, 5% CO_2 saturation and a humidity of 80%.

3.10 Preparation of *in vitro* expression vectors

Genscript (Germany) was commissioned to clone the DNase1 variants into pLIVE plasmids, which we were then used for further experiments. We excised the complementary DNA (cDNA) using restriction enzymes Nhe I-HF and Xho I and cloned it into a pcDNA3.1 plasmid. The cDNA was inserted into the multi-cloning site (MCS) between restriction sites Nhe I-HF and Xho I. The sequences of the generated vectors were confirmed by sequencing. All plasmids were purified from NEB 5-alpha F'I^q Competent *E. coli* (C2992H, New England Biolabs) using PureLink HiPure Plasmid Maxiprep Kit (K210007, Thermo Fisher Scientific).

3.11 Mammalian cell transfection

We seeded 2.5×10^6 HEK293 cells in a T25 flask in DMEM (41965039, Gibco) supplemented with 10% FBS (16250078, Gibco) and 1% penicillin-streptomycin (15140122, Life Technologies). Upon reaching 60-80% confluency, cells were washed once with PBS and fresh DMEM (without any supplementation) was added to the cells. We then prepared 5 ml of the reaction mixture, containing the transfection agent polyethyleneimine (PEI, 23966-2, Polysciences) and plasmid DNA in a 3:1 ratio. The mixture was immediately vortexed and incubated for 10 min at room temperature before it was added dropwise to the cells. After 48 h, the supernatant was collected and centrifuged for 5 min at 500 x g.

3.12 Quantification of DNase1 activity in plasma

DNase activity was measured using the DNase Alert QC System (AM1970, Thermo Fisher Scientific). Substrate solution and 10X nuclease buffer, both provided in the kit, were dispensed into a black 96-well plate, before 20-fold diluted heparinized plasma (in nuclease-free water, 00843566, Invitrogen) was added to the respective wells.

Fluorescence was measured with a microplate reader (Tecan Spark 10M) at excitation/emission maxima of 530/580 nm at 37 °C.

3.13 DNase1 activity by single radial enzyme diffusion (SRED) assay

DNase1 activity was measured with an agarose gel containing 0.13 mg/ml dsDNA purified from salmon testes (D1626, Sigma), 10 mM $MgCl_2$, 2 mM $CaCl_2$, and 2 x SYBR Safe (S33102, Invitrogen) in 20 mM Tris-HCl pH 7.8. After adding 2 µl of the samples to the wells, gels were incubated for 3 h at 37 °C in a humidity chamber, prior to recording DNA fluorescence with a fluorescence scanner (Bio-Rad ChemiDoc™ Imager). ImageJ 1.53t was used for the quantification of the diameter of the circles reflecting DNase activity.

3.14 DNase1L3 activity by chromatin degradation assay

To assess DNase1L3 activity we isolated nuclei from HEK293 cells using the Nuclei Isolation Kit Nuclei EZ Prep (NUC101, Sigma Aldrich). 5 µl of HEK293 cell supernatants expressing DNase1 mutants, murine serum, urine, or bile (the latter 1:10 diluted) were mixed with chromatin purified from 1.5×10^6 HEK293 cells in 20 mM Tris-HCl pH 7.4, 2 mM $MgCl_2$, 2 mM $CaCl_2$, 50 mM NaCl and 1x HALT protease inhibitor (78425, Thermo Fisher Scientific). The mixtures were incubated at 37 °C for 1 h and then heated for an additional 10 min at 65 °C. The QIAmp DNA Blood Mini Kit (51106, Qiagen) was used to isolate the DNA from the samples. The eluted DNA samples were then loaded onto a 2% agarose gel and fluorescence was recorded with the Bio-Rad ChemiDoc™ Imager. ImageJ 1.53t was used to quantify fluorescence intensity of digested high molecular chromatin aggregates on a grayscale inverted LUT image. To overcome inter-animal variability of transgenic mice and low signal intensity, we scanned the entire DNA signal including high molecular weight chromatin aggregates and the DNA-fragment ladder pattern up to the last visible signal in chromatin degradation gels shown in Figure 24.

3.15 Neutrophil isolation from human blood

Human neutrophils were isolated from citrate-anticoagulated blood (02.1067.001, Sarstedt) as previously described (132). Use of healthy human blood samples for isolation of neutrophils was approved by the Ethics Committee of the Hamburg Medical

Association. In brief, 7 ml of blood was layered onto 7 ml Histopaque 1119 (11191, Sigma Aldrich) and centrifuged for 20 min at 800 x g. The granulocyte-rich layer was collected and washed with Hanks-buffered salt solution without divalent cations (HBSS-, 14170112, Life Technologies) supplemented with 5 mM EDTA (E3889, Sigma Aldrich) and 0.1% BSA (A1470, Sigma Aldrich). The cells were further separated on a discontinuous Percoll gradient (17544501, GE Healthcare), centrifuged again, and washed with 0.1% BSA in HBSS-. Neutrophil viability was determined by trypan blue exclusion.

3.16 DNase activity by *ex vivo* NET degradation

Isolated human neutrophils from healthy volunteers were seeded in a 96-well plate at a concentration of 1×10^6 cells per well in serum-free DMEM (41965039, Gibco) and 1% penicillin-streptomycin (15140122, Life Technologies) prior to activation with 100 nM PMA (P8139, Sigma Aldrich) for 4 h at 37 °C, 5% CO_2, and humidity between 85-95%. After 4 h of incubation, DMEM was aspirated, and NETs were kept overnight at 4 °C in PBS. Next, we assessed NET-degrading capacity by co-incubating formed NETs with either 10-fold HBSS-diluted plasma or HEK293 cell supernatants for 3 h at 37 °C with 5% CO_2 and humidity between 85-95%. Recombinant human DNase1 (7.8 µg/ml, Pulmozyme, Roche, Germany) was used as positive control. Plasma/supernatants were aspirated from the wells, and NETs remnants were then fixed with 2% formalin (ROTI Histofix, P087.1, Roth) in PBS for 1 h. After washing the plates with PBS, the wells were stained with 1 µM of the nuclear dye Sytox Green (S7020, Invitrogen). Fluorescent images of nuclei and NETs were obtained with an inverted fluorescence microscope (Zeiss Axiovert 200M), and a microplate fluorometer (Tecan Spark 10 M) was used to quantify fluorescence.

3.17 Immunofluorescence staining of brain and lung tissue

For visualization, we stained formalin-fixed vibratome (300 µm and 100 µm) or paraffin-embedded (4 µm) lung and brain cross-sections. Paraffin sections were deparaffinized, rehydrated, and subjected to heat-induced antigen retrieval for 25 min at 100 °C in citrate buffer (10 mM sodium citrate, 0.1% Tween, pH 6). Sections were permeabilized for 20 min at room temperature (RT) with 0.5% Triton-X100 (T8787, Sigma Aldrich) in PBS (PBS-Tx) and subsequently blocked for 2 h with 3% BSA (A1470, Sigma Aldrich) in PBS-Tx. Primary antibodies were incubated overnight at 4 °C, followed by washing

with PBS-Tx and secondary antibody incubation overnight at 4 °C. Autofluorescence was quenched with 0.1% Sudan Black B (199664, Sigma Aldrich) in 70% ethanol for 25 min. Sections were washed thrice again and mounted in DAKO fluorescence mounting medium. The inverted confocal microscope Leica SP8 with 10x HC PL APO CS, 20x HC PL APO IMM/CORR CS2 and 63x HC PL APO Oil CS2 objectives and Leica LAS-X software from the UMIF Core Facility were used to image and generate maximum intensity projections of Z-stacks.

Primary antibodies for formalin-fixed tissue: anti-NE (5 µg/ml, ab21595, Abcam), anti-chromatin (anti-histone H2A/H2B/DNA-complex, 5 µg/ml, Davids Biotechnologie GmbH (1)), anti-collagen I (5 µg/ml, ab34710, Abcam), anti-fibrin (5 µg/ml, MABS2155, Merck), AlexaFluor488-conjugated anti-FXIIa (10 µg/ml, 3F7, CSL Limited), anti-H3cit (1 µg/ml, ab5103, Abcam), and anti-CD62P (P-selectin, 5 µg/ml, ab6632, Abcam).

Primary antibodies for paraffin-embedded tissue: anti-NE (10 µg/ml, ab68672, Abcam), anti-chromatin (anti-histone H2A/H2B/DNA-complex, 5 µg/mL, Davids Biotechnologie GmbH (1)), anti-vWF (32 µg/ml, A0082, Dako), and anti-MPO (3 µg/ml, ab9535, Abcam).

Secondary antibodies conjugated to AlexaFluor-488, -594 and -647 from Jackson ImmunoResearch were used (all donkey, used at 1:200 dilution).

3.18 Immunofluorescence staining of NETs

Immunofluorescence staining of NETs from purified human neutrophils was done on 13 mm glass coverslips in 12-well plates that were pre-coated with 0.1% poly-L-lysine (P4707, Sigma Aldrich) for 10 min at RT, and blocked with PBS/0.1% BSA (A1470, Sigma Aldrich), for 30 min at RT. Isolated human neutrophils from healthy volunteers were seeded onto coverslips at a concentration of 10^6 cells per well in serum-free DMEM (41965039, Gibco) prior to activation with 10 nM PMA (P8139, Sigma Aldrich) for 4 h at 37 °C, 5% CO_2, and humidity between 85-95%. After treating NETs with heparin (100 U/ml, Heparin-Natrium Braun "Multi" 10 000 I.E./ml, B. Braun) or buffer for 1 h at 37 °C, NETs were carefully washed with PBS and incubated with the primary antibodies anti-NE (2 µg/ml, ab21595, Abcam) and anti-H3cit (2 µg/ml, ab5103, Abcam) overnight at 4 °C. After washing, NETs were incubated with the AlexaFluor-488 labeled secondary antibody (1:5000, goat anti-rabbit, A11008, Invitrogen) for 1 h at RT, and mounted in Fluoroshield with DAPI (F6057, Sigma Aldrich). The inverted microscope Nikon Eclipse Ts2R with 10x/0.25 Ph1 ADL WD 6.2, 20x/0.40 Ph1 ADL

WD 3.1, and 40x/0.55 Ph1 ADL WD 2.1 objectives and Nikon NIS-Elements software or the inverted fluorescence microscope Axiovert 200M (objective: LD Plan-Neofluar 20x/0.4, Zeiss) were used to acquire and generate fluorescence images.

3.19 Quantification of FXIIa-positive NETs in lung vibratome sections

The quantification of pulmonary FXIIa-positive NETs was performed using ImageJ 1.53t. The H3cit-associated channel was first used to determine the NET-positive areas before the relative fluorescent units per area (mean fluorescence intensity) of the FXIIa signal on NETs was measured and the average mean fluorescence intensity of the background was subtracted. We analyzed n = 107 NET-positive areas from three COVID-19 lungs, and n = 35 NET-positive areas from three control lungs with other lung pathologies in three independent experiments.

3.20 Immunoblotting

Immunoblotting was performed with heparinized plasma samples from COVID-19 patients and healthy donors, or mouse bone marrow cells flushed from femur and tibia. Plasma samples were separated by SDS-PAGE, blotted onto PVDF membranes, and blocked with 5% normal mouse serum (015-000-120, Jackson Laboratories, USA) overnight at 4 °C. The membranes were incubated with an anti-human FXII/FXIIa antibody (1:500, GAHu/FXII, Nordic-MUbio, The Netherlands) for 1 h at RT, washed and incubated with a HRP-coupled secondary antibody (1:5,000, 18-8814-33, Rockland Immunochemicals, Inc., USA) again for 1 h at RT. Membranes were developed with the Bio-Rad ChemiDoc™ Imager. Quantification of FXIIa protein levels was subsequently performed by densitometric analysis with ImageJ 1.53t. Protein levels were normalized to albumin signals from Ponceau staining and FXII deficient plasma (#1200, Lot 6204, George King Bio-Medical, USA) was used as a negative control.

The bone marrow cell lysates underwent electrophoresis on a gradient SDS-PAGE gel (Criterion XT precast gel, 4-12%, 3450123, BioRad). Proteins were transferred onto nitrocellulose membranes and after blocking with Intercept (TBS) Blocking Buffer (Li-Cor, 927-60001) for 1 h, the membranes were incubated with an anti-GSDMD antibody (1:1,000, ab219800, Abcam) overnight at 4 °C, followed by a 1 h incubation with secondary goat anti-rabbit IgG (1:10,000, ab6721, Abcam). Antibodies were diluted in

blocking buffer supplemented with 0.2% Tween-20. Membranes were developed with the Bio-Rad ChemiDoc™ Imager.

3.21 Generation of *Gsdmd/Dnase1/Dnase1l3*^{-/-} mice using CRISPR/Cas9

Single guide ribonucleic acids (sgRNAs) flanking and targeting exon 3 (2nd coding exon) of mouse *gasdermin d* gene were designed and templates for transcription were derived by PCR using Q5-Polymerase (Biolabs). Transcription was performed using the HiScribeT7 kit (Biolabs, E20140S) with subsequent purification of the transcripts with the MEGAClear™ kit (Fisher Scientific, AM1908), both according to the manufacturer's instructions. Electroporation into single cell stage embryos derived from *Dnase1/Dnase1l3*^{-/-} mice using 300 ng/µl of each sgRNA and 500 ng/ml Cas9 protein (IDT) in OptiMEM medium (Gibco) was performed with a NEPA 21 electroporator (Nepagene) with settings used as previously described by Remy et al. (133). Injected embryos were implanted into F1 foster mothers (C57BL6/J x CBA). Genotyping of mice was performed using PCR.

3.22 Isolation of bone marrow cells

From each mouse, the bone marrow cells were flushed from both femurs and tibias with ice-cold PBS. The cells were resuspended with ice-cold PBS and centrifuged at 2,000 x g for 5 min at 4 °C; this step was repeated twice. The cell pellets were then lysed with RIPA lysis buffer (89901, Thermo Fisher Scientific) supplemented with Complete Protease Inhibitor Cocktail (4693132001, Roche) for 30 min at 4 °C with agitation. Cell lysates were centrifuged at 16,000 x g for 20 min, supernatants were collected, and protein concentrations were quantified by the bicinchoninic acid (BCA) protein assay kit (23225, Thermo Fisher Scientific).

3.23 Preparation of *in vivo* expression vectors

We used pLIVE plasmids (Mirus Bio, USA) to express proteins in a murine model. The vector enables long-lasting and hepatocyte-specific expression of proteins. We generated pLIVE plasmids containing human WT DNase1 and engineered DNase1 variants. For human *DNASE1*, a PCR of the cDNA (GenBank Accession Number NM010061) was performed using the primer pair *DNase1*-F 5´-

GTCGACATGCGGTACACAGG-3´ and *DNASE1*-R 5´-CTCGAGTCAGATTTTTCTGAGTGTCA-3´ containing Sal I and Xho I restriction sites. The cDNA of DNase1 was cloned using the T4 ligase (M0202S, New England Biolabs, Germany) into the multiple cloning site (MCS) of the pLIVE vector, which was digested with the matching enzymes. The cDNA of the DNase1 variants was available as part of the pcDNA3.1 plasmid (Genscript, Germany) which we excised using Nhe I-HF and Xho I and cloned into a pLIVE plasmid. The cDNA of colony stimulating factor 3 (*Csf3*, GenBank Accession Number BC120761) was inserted in the MCS between restriction sites Sal I and Xho I. The sequences of the generated vectors were confirmed by sequencing. All plasmids were purified using the PureLink HiPure Plasmid Maxiprep Kit (K210007, Thermo Fisher Scientific) and potential contaminations of endotoxin were removed using High-Capacity Endotoxin Removal Spin Columns (88274, Thermo Fisher Scientific).

3.24 Production of *Csf3* or *Dnase1* transgenic mice

The pLIVE plasmids containing constructs for G-CSF (*Csf3*) or different DNase variants were administered to 8–12-week-old mice via the hydrodynamic tail vein injection (134). In brief, 50 µg of the pLIVE plasmid were diluted in 0.9% saline in a volume equivalent to 10% of the body mass of the mouse. Mice were anesthetized with isoflurane and the plasmid solution was then injected intravenously over 5-8 seconds via the tail vein.

3.25 Reverse transcription PCR

RNA from tail biopsies was isolated according to the manufacturer's protocol (74104, Qiagen RNeasy Mini Kit). Reverse transcription of RNA into cDNA was performed using the SuperScript IV VILO Master Mix (11756050, Thermo Fisher Scientific). The cDNA was then quantified with the GSDMD gene probe for mice (Taqman Gsdmd Mm00509958_m1, 4331182, Thermo Fisher Scientific) and run on the StepOnePlus Real-Time PCR System (Applied Biosystems).

3.26 Genotyping PCRs

DNA from tail biopsies was isolated using the blackPREP Rodent Tail DNA Kit (845-BP-0010250, IST Innuscreen) according to the manufacturer's protocol. DNA templates were amplified on the PTC-200 thermal cycler (MJ Research) using the

KAPA2G Fast HotStart Genotyping Mix (KK5621, Roche) and the respective PCR primers (Eurofins, Germany) for all mouse lines except for *Gsdmd/D1/D1l3$^{-/-}$*. DNA from *Gsdmd/D1/D1l3$^{-/-}$* mouse tails was amplified using a genotyping mix containing dNTP mix (10 mM, 201901, Qiagen), Taq DNA polymerase (250 U, 201203,Qiagen), and the respective primers. PCR protocols and primers are given in **Table 1**. Amplified DNA fragments were visualized by agarose gel electrophoresis.

Table 1: PCR cycling conditions. PCR cycling profiles for the different knockout (KO) mouse lines used in this study are shown.

Mouse line	Temperature	Time	Number of cycles
Dnase1 KO	95 °C	4 min	1
	95 °C	15 sec	29
	61 °C	15 sec	
	72 °C	20 sec	
	72 °C	10 min	1
Dnase1-like 3 KO	95 °C	4 min	1
	95 °C	15 sec	32
	64 °C	15 sec	
	72 °C	20 sec	
	72 °C	10 min	1
Myd88 KO	94 °C	3 min	1
	94 °C	20 sec	9
	66 °C	15 sec (-0.5 °C per cycle)	
	72 °C	10 sec	
	94 °C	15 sec	28
	61 °C	15 sec	
	72 °C	10 sec	
	72 °C	10 min	1
Pad4 KO	95 °C	5 min	1
	95 °C	30 sec	34
	66 °C	30 sec	
	72 °C	40 sec	
	72 °C	10 min	1
Gsdmd KO	94 °C	2 min	1
	94 °C	15 sec	34
	60 °C	30 sec	
	72 °C	40 sec	
	72 °C	5 min	1

The following PCR primers were used to amplify the genes of interest:

Dnase1 KO CRLSV40pA_F primer: 5' CAC TGC ATT CTA GTT GTG GTT TGT C 3'

Dnase1 KO tm1_mR1 primer: 5' GAG GCA GGA CTT AAT ACA CAA ACA G 3'

Dnase1-like 3 KO G3 primer: 5' GGG CCA GCT CAT TCC TCC ACT C 3'

Dnase1-like 3 KO R7 primer: 5' CAC TCC TGG GCT TCT TGA TGG TCA G 3'

Myd88 oIMR9481 primer: 5' GTT GTG TGT GTC CGA CCG T 3'

Myd88 oIMR9482 primer: 5' GTC AGA AAC AAC CAC CAC CAT GC 3'

Myd88 9335 primer: 5' CCA CCC TTG ATG ACC CCC TA 3'

Pad4 3loxF primer: 5' AGT CCA GCT GAC CCT GAA C 3'

Pad4 3loxR primer: 5' CTA AGA GTG TTC TTG CCA CAA G 3'

Pad4 5loxF primer: 5' CAG GAG GTG TAC GTG TGC A 3'

Gsdmd F primer: 5'GTT CCC TCC AGC CCT ACT TGC TC 3'

Gsdmd Rev primer: 5'GAG AAG TGG ACA CTC GTG CCT GTG 3'

3.27 Sterile neutrophilia

Mice at 8-12 weeks of age were hydrodynamically injected into the tail vein with 50 µg of the pLIVE-plasmid containing *Csf3* to induce G-CSF expression and neutrophilia, as described before (92). Mice were euthanized and considered "non-survivors" when showing defined signs of distress combined with hematuria, and rapid and severe hypothermia, defined as decrease in body temperature of ≥ 4 °C compared to the body temperature before the plasmid injection. Body temperature of the mice was measured in the perianal area using a contactless infrared thermometer and body weight was determined with a scale. Mouse experiments were performed according to national guidelines for animal care and were covered by the animal proposal 69/16 and 143/15, approved by the Ministry for Health and Consumer Protection in Hamburg, Germany.

3.28 Septicemia

In the septicemia model, mice at 6-12 weeks of age received daily intraperitoneal (i.p.) injections of 1 µg/g of LPS from *Salmonella enterica* serotype *thyphimurium* (product number L6511, lot number 025M4042V, Sigma) in 0.9% saline, along with an intravenous (i.v.) injection of 1.5×10^7 heat-killed *E. coli*/g body weight on the third day of LPS treatment, as described before in (92). Mice were euthanized and considered "non-survivors" when showing defined signs of distress combined with hematuria, and severe hypothermia as described before (3.27 Sterile neutrophilia). When setting up

the septicemia model, we tested daily i.p. injections of 1 µg/g of LPS, however by day 3 only around 20% of the vasculature was occluded in *D1/D1l3$^{-/-}$*, which was not sufficient for a definite lethal result. To improve the model, the mice were treated with one i.v. injection of heat-killed *E. coli* along with the third LPS injection. Mouse experiments were performed according to national guidelines for animal care and were covered by the animal proposal 22/17, approved by the Ministry for Health and Consumer Protection in Hamburg, Germany.

3.29 Murine blood, plasma, and tissue collection

Blood was collected with glass capillaries from the retro-orbital sinus into 200 µl EDTA tubes (GK 150, KABE Labortechnik). Plasma was obtained after centrifugation at 3,000 x g for 15 min and stored in aliquots at −20 °C until further use. For organ analysis, mice were perfused by intracardiac infusion of PBS. Organs were collected and fixed for 24 h in 4% formalin (ROTI Histofix, P087.1, Roth) at 4 °C and embedded in paraffin for sectioning.

3.30 Neutrophil isolation from mouse blood

EDTA anticoagulated (GK 150, KABE Labortechnik) whole mouse blood was 5-fold diluted in PBS containing 1% BSA (A1470, Sigma Aldrich) and 15 mM EDTA (E3889, Sigma Aldrich) and fractionated on a discontinuous sucrose gradient. 3 ml of 1.119 g/ml sterile-filtered sucrose was added to the bottom of a 15 ml conical polypropylene centrifuge tube. 3 ml of 1.077 g/ml sterile-filtered sucrose was layered on top of the 1.119 g/ml layer. Thereafter, 6 ml of diluted blood was layered on top of the 1.077 g/ml layer and centrifuged at 700 x g for 30 min at RT without brake. Neutrophil isolation was continued using the negative selection method according to the manufacturer's protocol of the neutrophil isolation kit (130-097-658, MACS Miltenyi).

3.31 Generation of *ex vivo* NETs

Mouse neutrophils were seeded at 10^7 cells/ml in DMEM supplemented with 2% BSA. Neutrophils were stimulated with 25 µM calcium ionophore A23187 (Sigma, C5149) or 10 nM PMA (Sigma, P8139) for 4 h in the presence or absence of the necroptosis/pyroptosis inhibitor necrosulfonamide (NSA, 10 µM, Selleck, S8251) or the PAD4 inhibitor GSK484 (5 µM, Sigma, SML1658) for 30 min at 37 °C, 5% CO_2 with

humidity and gentle shaking. NET degradation was controlled by treating NETs with 10 U/ml recombinant human DNase1 (Pulmozyme, Roche) for 1 h at 37 °C, which resulted in a complete degradation of the formed NETs. NET clots were fixed with 2% PFA overnight at 4 °C. Fixed NET clots were embedded in paraffin and sections were analyzed for NET markers. The area of NETs (in kPx) was quantified using the polygon setting in ImageJ 1.53t.

3.32 Statistics

Prism version 8.2.0 (GraphPad, USA) was used for graphic representation and statistical analysis of data. A two-tailed unpaired Student's t-test was used to compare between two means, and Mann-Whitney test was used if data were not normally distributed. One-sample t-test was used for comparison with a hypothetical mean. More than two groups were either analyzed by ordinary one-way ANOVA with Dunnett's multiple comparisons test, or Kruskal-Wallis test with Dunn's multiple comparisons depending on data distribution. Pearson's correlation was used to correlate clinical parameters. Kaplan-Meier curves were generated for survival analyses. Data with two different categorical variables were compared by two-way ANOVA. Differences were considered statistically significant when $p < 0.05$.

4. Results

4.1 Thrombo-inflammation and NET formation in COVID-19 and VITT

4.1.1 FXII is increased and activated in COVID-19 lung tissue

NETs interfere with dissemination of harmful pathogens; however, an excessive accumulation of NETs predisposes to thrombo-inflammation, autoimmunity, and eventually tissue damage. We aimed to identify pathways involved in the progression of thrombo-inflammatory processes in the lungs of diseased COVID-19 patients. The postmortem lung tissues were obtained from deceased individuals between 58 and 87 years of age, with two male and one female COVID-19 patient, and all three control lungs were from females (**Fig. 2a**). The postmortem interval (PMI) ranged from 0 to 2 days, the body mass index (BMI) and the weight of the autopsied lungs varied between COVID-19 and control patients. Control and COVID-19 patients suffered from comorbidities, with cardiac insufficiency being the most common one. All three COVID-19 patients suffered from DVT and eventually died from PE and/or pneumonia, whereas the three control patients either died from cardiac insufficiency, hypovolemic shock, or acute respiratory distress syndrome (ARDS). Histological analysis of the COVID-19 lung tissue showed the accumulation of pathologic hyaline membranes lining the alveoli (**Fig. 2b**, black arrows). Hyaline membranes consist of fibrin, mucopolysaccharides, glycoproteins, and cell debris, impairing gas exchange, and aggravating pulmonary failure.

a

Patient	Sex	Age (years)	PMI (days)	Cause of death	Comorbidities	DVT	BMI	Lung weight (grams)
COVID19-1	male	71	2	PE, pneumonia	CI, DM, lung granuloma	yes	36.8	2725
COVID19-2	male	63	1	PE, pneumonia	CI	yes	37.3	2470
COVID19-3	female	75	2	PE	hypertension, IHD	yes	24.8	900
CTRL 1	female	82	1	Right ventricular insufficiency	COPD, RI	no	18.0	770
CTRL 2	female	87	0	Hypovolaemic shock	CI, RI, Status post brain injury	no	27.4	740
CTRL 3	female	58	1	ARDS	Wegener's granulomatosis	no	48.4	1860

b
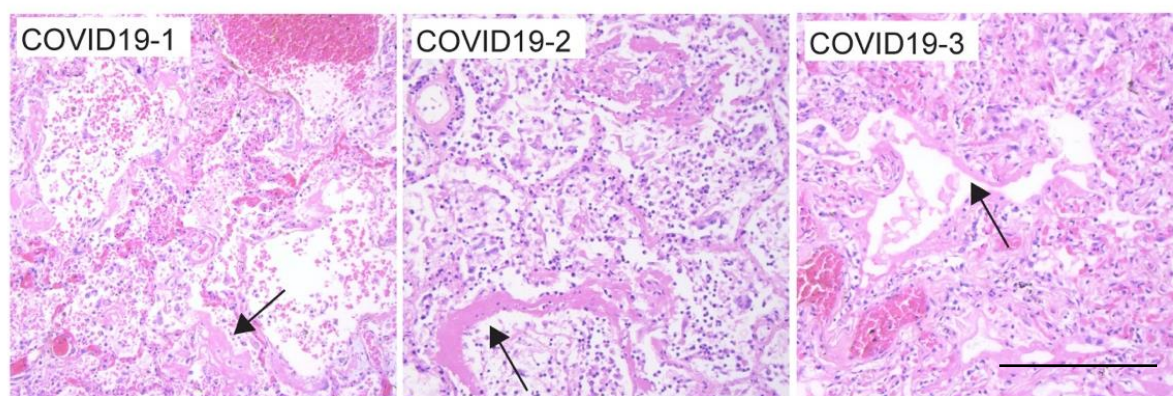
Figure 2. COVID-19 patients had cardiac comorbidities and lung tissue showed accumulation of pathologic hyaline membranes. (a) Demographics of patients that were included for autopsied lung tissue analysis. Lung tissue was analyzed from deceased COVID-19 patients (n = 3) and age- and postmortem interval (PMI)- matched control patients (n = 3) with other lung pathologies. (b) Histology of COVID-19 lung paraffin sections stained with Hematoxylin and Eosin (H&E) (n = 3). Hyaline membranes are indicated with black arrows. Scale bar: 100 μm. Deep vein thrombosis (DVT), body mass index (BMI), pulmonary embolism (PE), acute respiratory distress syndrome (ARDS), cardiac insufficiency (CI), diabetes mellitus (DM), ischemic heart disease (IHD), chronic obstructive pulmonary disease (COPD), renal insufficiency (RI). Figure adapted from (1), in the original paper Supplementary Table 1a and Supplementary Fig. 1a.

Postmortem lung tissue from deceased COVID-19 and patients with different pulmonary pathologies were analyzed using differential proteomics (**Fig. 3a**). Differential proteomics can identify proteome changes between physiological or pathological states. To specifically probe for *in situ* proteomic changes in thrombo-inflammatory pathways in COVID-19 lungs, the lung tissue was dissected with a stereomicroscope prior to analysis. During the dissection, we removed any noticeable clots that could be a consequence of DVT with PE and thus interfere with the analysis. We performed a gene ontology (GO) analysis to screen for enriched cellular pathways

in COVID-19 lungs. Pathways related to classical complement activation (green), angiogenesis (red), platelet degranulation (magenta) as well as neutrophil activation and degranulation (blue) were upregulated in lung tissue from COVID-19 patients (**Fig. 3b**). Besides these highlighted pathways, a range of proinflammatory cytokines was upregulated i.e., IL-1, IL-6, and IL-21, interferon, NF-κB, and also major histocompatibility complex (MHC) I mediated signaling pathways (black). Furthermore, upregulated cellular responses to hypoxia reflected the excessive local cell death rate in the lungs of diseased COVID-19 patients (**Fig. 3b**).

Enriched GO term	Fold increase
antigen processing and presentation of exogenous peptide antigen via MHC class I, TAP-independent (GO:0002480)	77.23
interleukin-21-mediated signaling pathway (GO:0038114)	57.92
antigen processing and presentation via MHC class Ib (GO:0002475)	44.13
type I interferon signaling pathway (GO:0060337)	41.49
antigen processing and presentation of exogenous peptide antigen via MHC class I, TAP-dependent (GO:0002479)	36.58
acute-phase response (GO:0006953)	28.25
interferon-gamma-mediated signaling pathway (GO:0060333)	22.52
NIK/NF-kappaB signaling (GO:0038061)	20.02
acute inflammatory response (GO:0002526)	19.31
negative regulation of viral genome replication (GO:0045071)	18.68
response to interleukin-6 (GO:0070741)	17.82
interleukin-1-mediated signaling pathway (GO:0070498)	16.89
negative regulation of viral life cycle (GO:1903901)	16.35
defense response to virus (GO:0051607)	12.55
complement activation, classical pathway (GO:0006958)	11.51
platelet degranulation (GO:0002576)	9.05
immune response-regulating cell surface receptor signaling pathway involved in phagocytosis (GO:0002433)	8.583
Fc-gamma receptor signaling pathway (GO:0038094)	8.33
lymphocyte mediated immunity (GO:0002449)	7.09
cellular response to hypoxia (GO:0071456)	7.24
response to decreased oxygen levels (GO:0036293)	6.47
neutrophil degranulation (GO:0043312)	6.25
neutrophil activation involved in immune response (GO:0002283)	6.20
regulation of angiogenesis (GO:0045765)	6.10
neutrophil activation (GO:0042119)	6.08
regulation of vasculature development (GO:1901342)	5.53
positive regulation of cytokine production (GO:0001819)	5.51

Figure 3. Proteomic analysis of COVID-19 lung tissue unveils enrichment of FXII, and pathways related to angiogenesis, complement, platelet, and neutrophil activation. (a) Heatmap depicts the differentially regulated protein expression in the lung tissue of patients with COVID-19 and COVID-19-independent lung pathologies (CTRL) (n = 3, each). (b) Selected Gene Ontology (GO) terms of increased proteins in COVID-19 lungs were correlated with biological pathways and showed an upregulation of complement (green), platelet degranulation (magenta), neutrophil activation (blue), and angiogenesis (red). (c) Protein association network analysis (https://string-db.org) of upregulated proteins in COVID-19 lungs. (d) Representative immunofluorescence images of COVID-19 lung sections using antibodies against collagen I (green) and fibrin (magenta). Fibrin depositions line the alveolar space of FXII-increased COVID-19 lungs (white arrows). Scale bar: 100 mm. Figure from (1), in the original paper Fig. 1.

Next, key proteins contributing to thrombo-inflammation in COVID-19 were identified by performing a protein association network analysis (https://string-db.org) from the previously obtained differential proteomics data (**Fig. 3c**). The network association analysis found enriched peptides including caspases, proteasome subunits, human leukocyte antigens, and coagulation factor XII (**Fig. 3c**, red rectangle) in the lungs of patients COVID-19-**1** and COVID-19-**3**. Consistent with previous studies (135) and the pronounced procoagulant state in COVID-19, our proteomic data also revealed accumulation of fibrin(ogen) protein complexes (fibrinogen alpha (log2fold change 1.73), beta (1.50), gamma chains (1.64)) in COVID-19 lung tissue. This finding was confirmed by immunofluorescence staining of COVID-19 lung vibratome sections using fibrin and collagen I antibodies, revealing extensive depositions of fibrin sheets on the alveolar walls (**Fig. 3d**, white arrows indicate fibrin depositions).

Platelet hyperactivity has been previously shown to occur in COVID-19 (136, 137). Concordantly, immunofluorescence staining of COVID-19 lung vibratome sections using an antibody against P-selectin (CD62P), a cell adhesion molecule and platelet activation marker, demonstrated an increase in degranulated platelets on the vessel walls (**Fig. 4**).
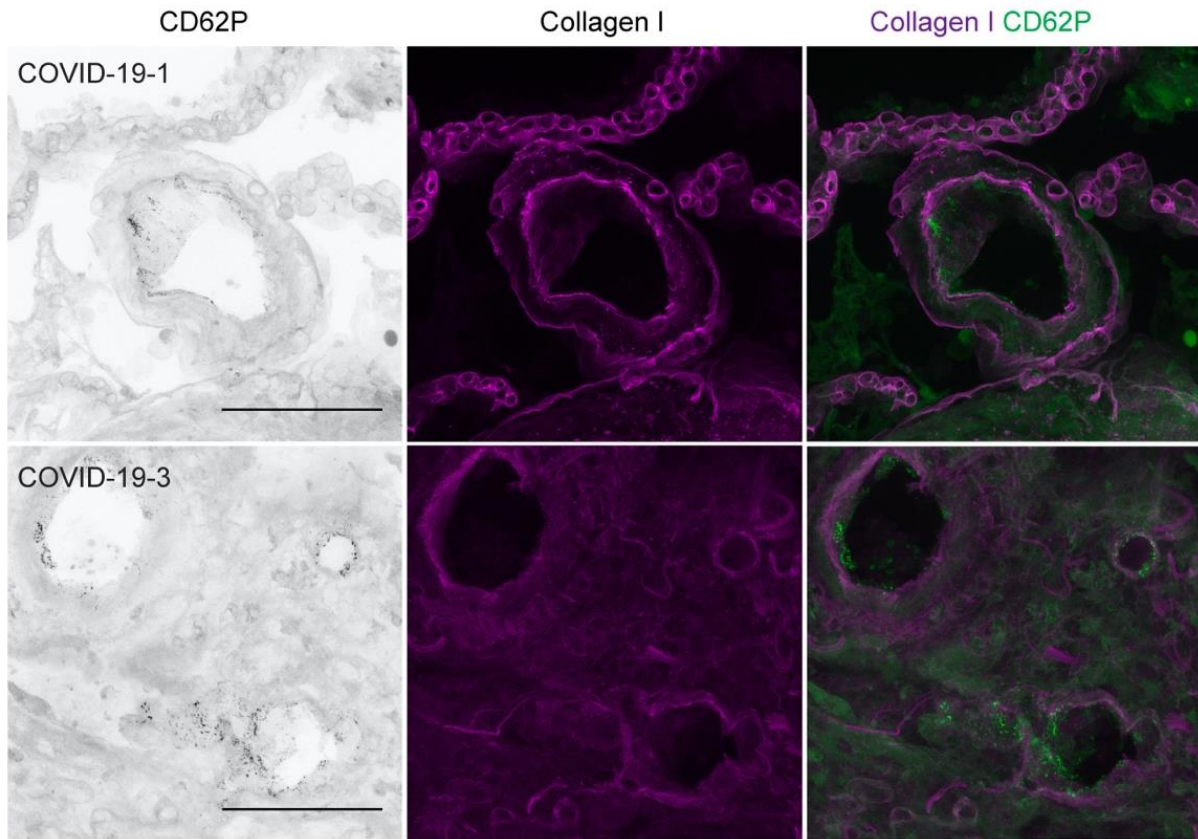
Figure 4: Platelets adhere to vessel walls of COVID-19 lungs. Platelets accumulate at microvascular vessel walls in COVID-19 lungs. Immunofluorescence of COVID-19 lung vibratome sections using antibodies against collagen I (magenta) and platelet marker CD62P (P-selectin, green, 1:100, ab6632, Abcam). Scale bar: 100 µm. Figure from (1), in the original paper Supplementary Fig. 1b.

To distinguish zymogen FXII from the active enzyme, FXIIa, we performed immunofluorescence staining of COVID-19 and control lung sections using the FXIIa specific antibody 3F7 (138) and collagen I antibodies (**Fig. 5a**). 3F7 specifically detects FXIIa and does not cross-react with zymogen FXII (139). The previous proteomics analysis enabled the detection of FXII-specific peptides, however, it does not have the capacity to discriminate between (inactive) zymogens and active proteases. Immunofluorescence staining revealed that FXIIa was enriched in the lung parenchyma, within the pulmonary vessels, and in fibrin-rich alveolar spaces of COVID-19 lung tissue (**Fig. 5a**). In the ARDS control tissue, no distinct FXIIa signal could be detected in the lung parenchyma.
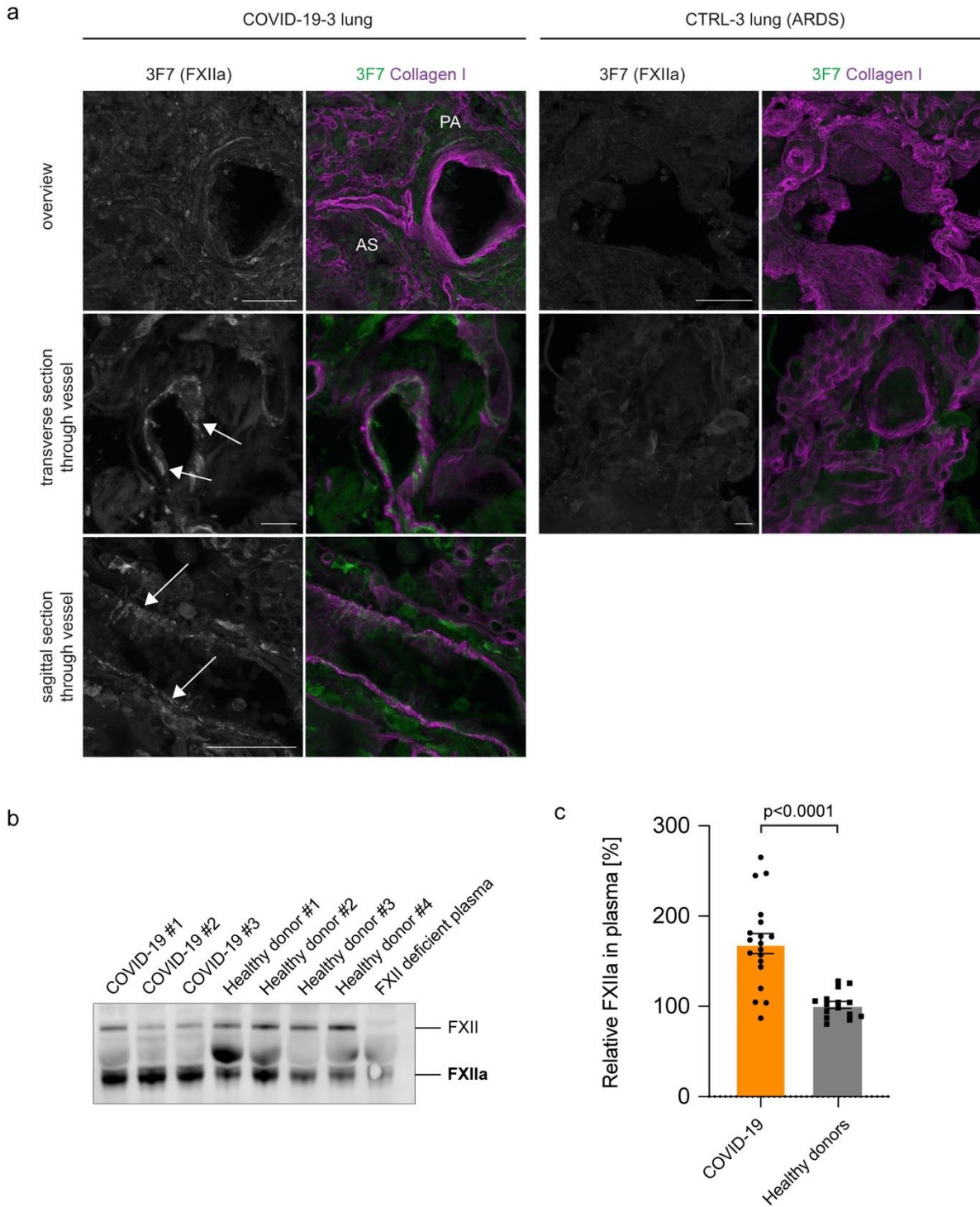
Figure 5. FXII is activated in COVID-19 lungs and plasma. (a) Representative immunofluorescence of vibratome sections from COVID-19 and acute respiratory distress syndrome (ARDS) control lungs using antibodies against FXIIa (3F7, green or grey in single channel images) and collagen I (magenta). White arrows indicate the FXIIa signal within the pulmonary microvasculature. Alveolar space (AS), parenchyma (PA). (b) Representative immunoblot of COVID-19 and healthy donor plasma samples blotted for FXII. The antibody detects zymogen FXII and cleaved, activated FXII (FXIIa). As a negative control, FXII-deficient plasma was used. (c) Quantification of FXIIa in COVID-19 plasma (n = 19) and age- and sex-matched healthy donor plasma (n = 15). FXIIa was normalized to plasma albumin levels.

Data represent mean ± s.e.m., p-value, and two-tailed unpaired Student's t-test. Scale bar: 100 mm top / 10 mm middle / 50 mm bottom panel (a). Figure from (1), in the original paper Fig. 2.

Subsequently, we examined if FXIIa can also be found in COVID-19 plasma samples. Samples of COVID-19 patients and sex- and age-matched healthy donors were compared by immunoblot analyses using an antibody (GAHu/FXII, Nordic MUbio) that detects both, the zymogen and active form of FXII (**Fig. 5, b, and c**). COVID-19 patients included for the plasma analyses in this study were on average 60 years of age, with a ratio of 2:1 male to female, and around 25% of the patients depended on extracorporeal membrane oxygenation (ECMO). The most prevalent comorbidities of that cohort were hypertension, obesity, diabetes, and kidney insufficiency (**Table 2**).

FXII-deficient plasma was used as specificity control. The representative immunoblot shows an accumulation of FXIIa in COVID-19 plasma samples while the signal was totally absent in the FXII-deficient sample (**Fig. 5b**). The increase in FXIIa was further substantiated by a corresponding decrease in zymogen FXII signal (upper band of immunoblot). In healthy donor plasma, a stronger signal for zymogen FXII compared to activated FXII was detected. These findings were quantified in **Fig. 5c**, showing a 67% increase of FXIIa in COVID-19 compared to healthy donor plasma (normalized to plasma albumin levels). Taken together, these findings show an accumulation of FXIIa in COVID-19 lung tissue and plasma compared to controls, implicating a contribution of FXIIa to pulmonary thrombo-inflammation in COVID-19.

Table 2: Clinical data and comorbidities of deceased COVID-19 patients from whom plasma samples were retrieved. Clinical data from enrolled COVID-19 patients (n = 43). Extracorporeal membrane oxygenation (ECMO) status, mean clinical chemistry parameters, and comorbidities are shown. Reference values (Ref) for clinical chemistry parameters of healthy donors are included for comparison. C-reactive protein (CRP), lactate dehydrogenase (LDH), acute myeloid leukemia (AML), acute lymphoblastic leukemia (ALL), immune thrombocytopenic purpura (ITP), and chronic obstructive pulmonary disease (COPD). Figure from (1), in the original paper Supplementary Fig. 1b.

	Mean	Range	Ref	Percentage
Age (years)	60.83	27-93		
Male	28			65.1
Female	15			34.9
ECMO	10			23.3
without ECMO	33			76.7
CRP (mg/ml)	66.24	4-245.44	<5	
IL-6 (ng/l)	80.46	2.7-699	≤7	
LDH (U/l)	385.92	113-652	84-246	
Leukocytes (Mrd/l)	8.12	0.2-19.05	3,8-11	
Platelets (Mrd/l)	238.59	13-567	150-400	
D-Dimer (mg/ml)	7.52	0.78-35.2	≤0.5	
Neutrophils (Mrd/l)	8.20	4.18-18.11	1,8-7,7	
Absolute Neutrophil Count (%)	73.08	30.3-93.3	39-75	

Comorbidities	
Hypertension	19
Obesity	12
Diabetes	12
Kidney insufficiency	11
Atrial fibrillation	5
Asthma	5
Coronary heart disease	5
AML	4
Benign prostatic hyperplasia	4
ALL	3
Multi-resistant bacteria	3
Hyperthyroidism	3
Thrombosis	3
Myocardial infarction	2
Fatty liver	2
Epilepsy	1
Cholecystolithiasis	1
Breast cancer	1
ITP	1
Aortic valve insufficiency	1
Skin cancer	1
COPD	1
Mitral valve insufficiency	1
Anemia of chronic kidney disease	1
Prostate cancer	1
Stroke	1

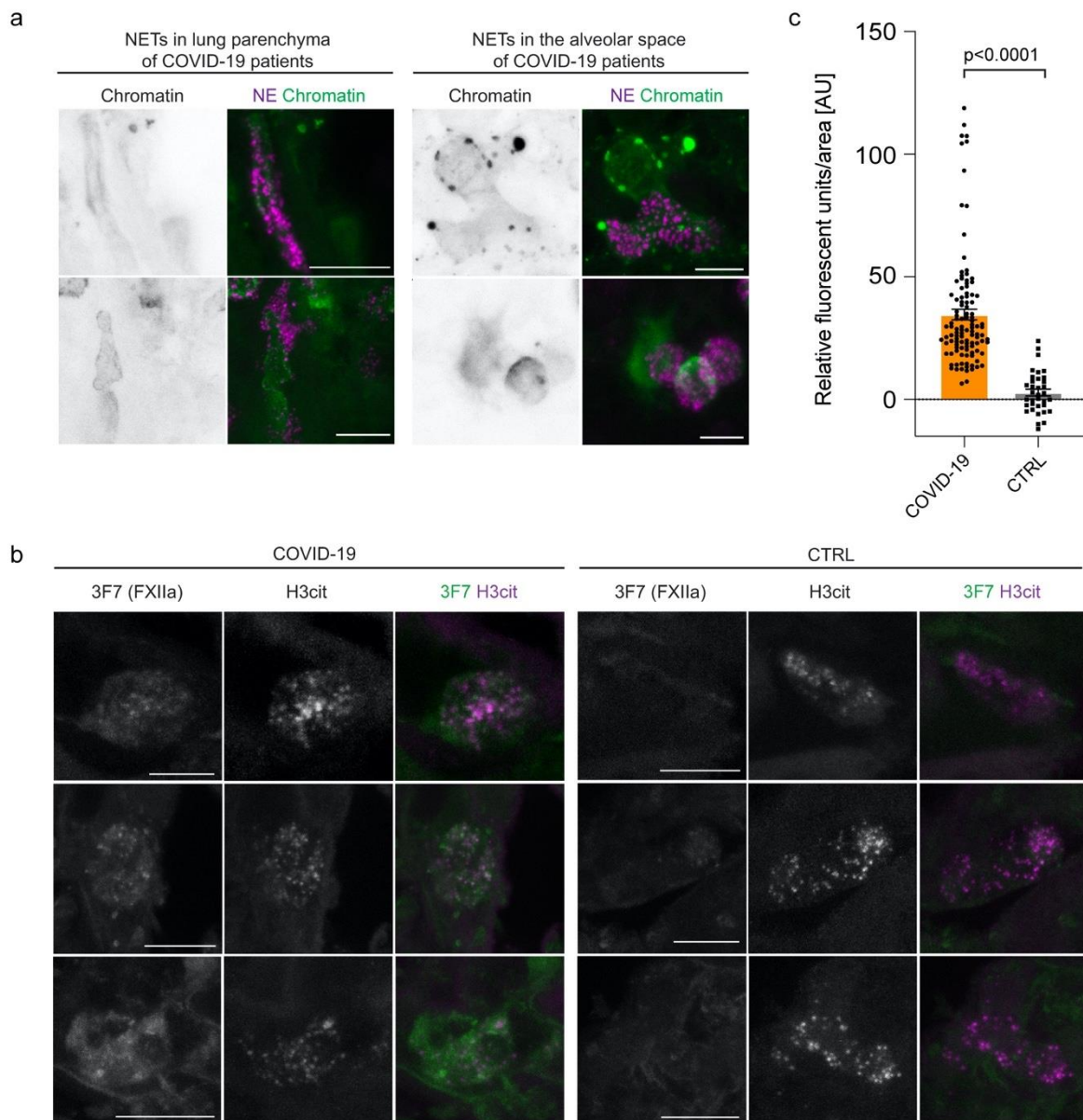## 4.1.2 NETs and FXII colocalize in COVID-19 lungs

Our next aim was to determine the mechanisms underlying FXII activation in COVID-19. A previous study showed that NETs can serve as FXII contact activating surface *ex vivo* (65). It is also known that NET formation is exacerbated in the plasma and lung tissue of COVID-19 patients (80, 82). Sections of COVID-19 lung tissue showed NET-specific markers NE and chromatin (**Fig. 7a**) indicating local accumulation of degranulated neutrophils and NET filaments in the parenchyma and alveolar space. To corroborate excessive NET formation within COVID-19 patients (n = 43) versus healthy donors (n = 39), NET markers in plasma samples, i.e., circulating extracellular DNA (ceDNA) and MPO were tested (**Fig. 6, a, and b**). Both, ceDNA and MPO were significantly increased in COVID-19 patient plasma compared to healthy controls ($p <$ 0.0001 and $p =$ 0.0016, respectively). ceDNA and disease-relevant biomarkers (82), including total peripheral leukocyte count and lactate dehydrogenase (LDH, cell destruction marker), as well as a tendency for C-reactive protein (CRP, inflammation marker) were positively correlated with each other (**Fig. 6, c – e**).
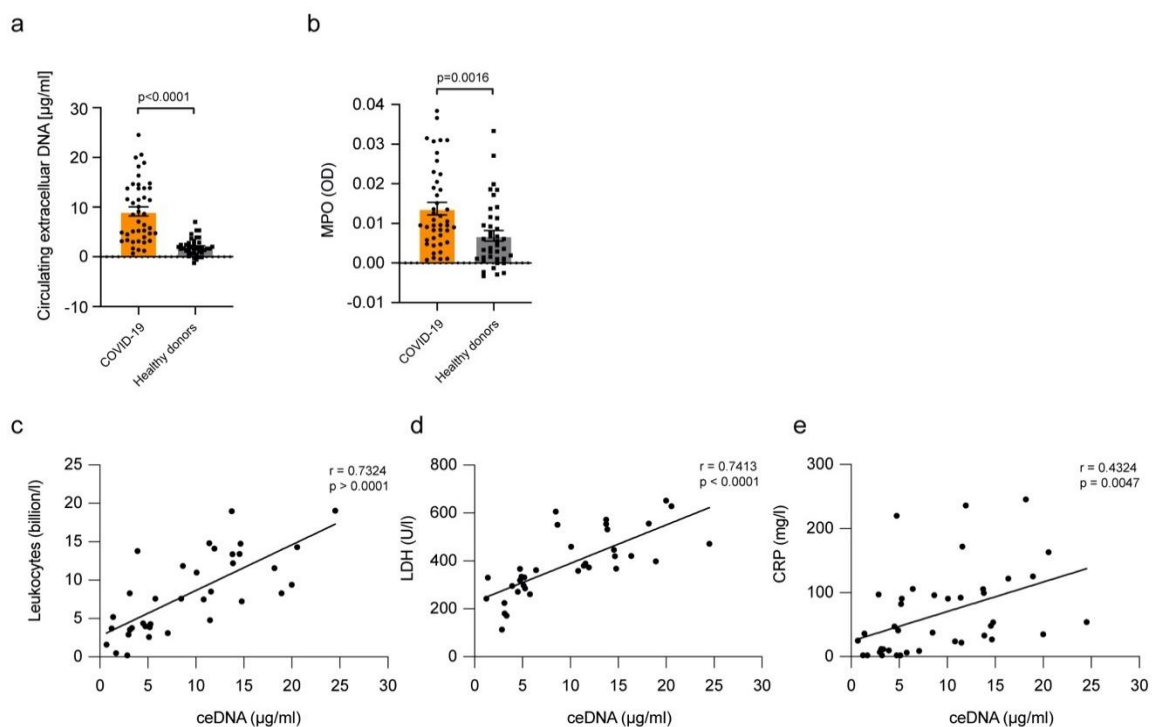
Figure 6. Elevated NET markers correlate with disease markers in plasma from COVID-19 patients. (a-b) Circulating extracellular DNA (ceDNA, a) and myeloperoxidase (MPO, b) levels were measured in plasma samples from COVID-19 patients (n = 43) and healthy donors (n = 39). Data represent mean ± s.e.m. p-value, unpaired Student's t-test. (c-e) ceDNA levels in COVID-19 plasma

samples were correlated with the laboratory markers absolute leukocyte count (n = 36) (c), lactate dehydrogenase (LDH) (n = 36) (d), and C-reactive protein (CRP) (n = 41) (e). Correlations with laboratory parameters were performed, when available. Linear regression, Pearson's correlation coefficients (depicted as r), and p-values are shown in each panel. Figure from (1), in the original paper Supplementary Fig. 2.

To confirm that NETs can act as contact activating surface for FXII in COVID-19 lungs, high-resolution immunostainings of lung sections using anti-FXIIa (3F7) and anti-H3cit antibodies were performed (**Fig. 7b**). Overlay of the immunofluorescent signals revealed co-localization of FXIIa and H3cit in COVID-19 lungs, whereas no FXIIa signal could be detected in control lungs. FXIIa signal was 12-fold increased in H3cit positive areas (indicating NETs) in COVID-19 lung tissue compared to control lungs (**Fig. 7c**). These findings show colocalization of NETs and FXII in the lungs of COVID-19 patients, which implicates activation of FXII and the intrinsic coagulation system.

Figure 7. FXIIa and NETs colocalize in COVID-19 lungs. (a) Representative immunofluorescence images of NETs in the lung parenchyma and the alveolar spaces using antibodies against NE (magenta) and chromatin (green or grey in single channel images). (b) Representative immunofluorescence of vibratome sections of COVID-19 and control (CTRL) lungs using antibodies against FXIIa (3F7, green or grey in single channel images) and citrullinated histone 3 (H3cit) (magenta or grey in single channel images). (c) Quantification of FXIIa pixel intensity in n = 107 H3cit-positive areas from three COVID-19 lungs and n = 35 H3cit-positive areas from three CTRL lungs. Negative values occur due to background subtraction. Data represent mean ± s.e.m., p-value, and two-tailed unpaired Student's t-test. Scale bar: 10 mm (a, b). Figure from (1), in the original paper Fig. 3.

4.1.3 Defective NET degradation contributes to excessive FXII activation in COVID-19 lungs

To identify the mechanism underlying NET accumulation in plasma, lung parenchyma, and alveolar spaces in COVID-19 patients, plasma samples were analyzed for DNase activity. To measure DNase activity, three different experimental approaches were used. First, DNase activity in plasma samples from COVID-19 patients and healthy donors was measured using the zymography-based SRED assay (**Fig. 8b**). DNase activity in COVID-19 was reduced by 23% compared to healthy donors. The reduced DNase activity in COVID-19 vs. healthy donor plasma samples was confirmed in an independent experiment using the fluorometric-based DNase Alert assay (**Fig. 8a**). The DNase Alert assay system is based on a DNA substrate tagged with a fluorescent reporter and a dark quencher. When DNases are present, the linkage between the fluor and quencher is cleaved, resulting in the emission of a bright fluorescence signal. Additionally, we tested the ability of plasma from COVID-19 patients versus healthy donors to degrade *ex vivo* generated NETs (**Fig. 8c**). COVID-19 plasma was unable to degrade NETs *ex vivo*, whereas healthy donor plasma degraded NETs within 3 h. This finding implies that defective NET degradation contributes to the pathologic NETs accumulation in COVID-19. To show that *ex vivo* generated NETs can be degraded by commercially available recombinant human DNase1, we treated them for 3 h with 10 U/ml Pulmozyme. Pulmozyme completely degraded NETs within 3 h (not shown).

Next, we assessed whether DNase-mediated NET degradation reduces activation of FXII *in vitro*. Neutrophils were activated with PMA to form NETs and FXII activation was measured by a chromogenic assay using a plasma kallikrein/FXIIa substrate (**Fig. 8d**). FXII activation decreased by 51% upon treating NETs with 10 U/ml Pulmozyme. When adding the FXII inhibitor rHA-infestin-4 (500 µg/ml) to the experimental setup, the FXIIa signal was completely inhibited. Incomplete NET degradation may contribute to prolonged FXII activation in COVID-19-associated pulmonary thrombo-inflammation. These findings indicate that targeting of FXIIa, as well as dissolution of NETs, might be beneficial in COVID-19.
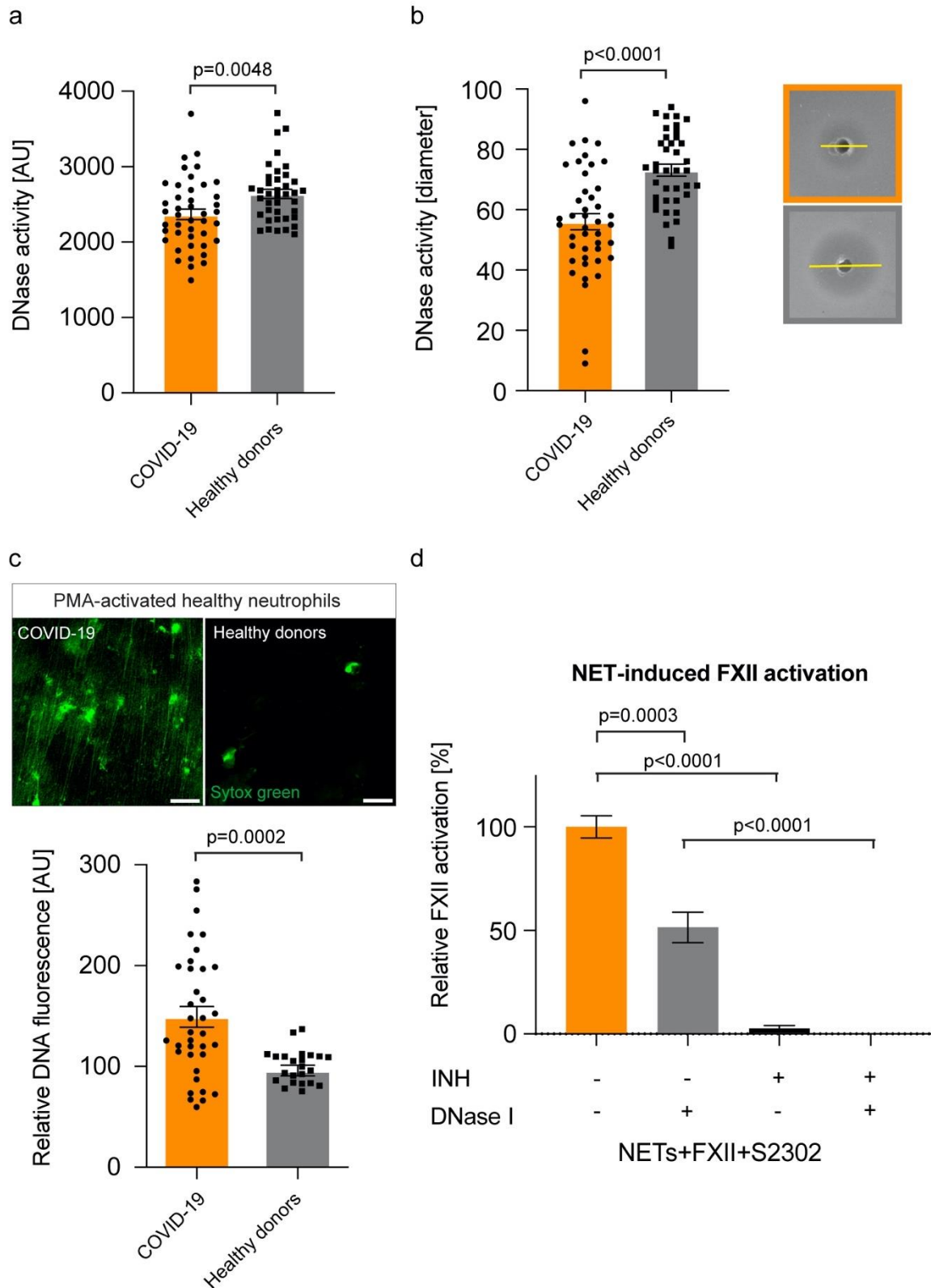
Figure 8. Defective DNase activity results in delayed NET clearance in COVID-19. (a) DNase activity in plasma samples from COVID-19 patients (n = 43) or healthy donors (n = 39) using the DNase Alert QC System based on quenching of a fluorescent DNA substrate. Data represent mean ± s.e.m.,

p-value, and two-tailed unpaired Student's t-test. (b) DNase activity in plasma samples from COVID-19 patients (n = 43) or healthy donors (n = 39) using the SRED assay. Representative zymography signals are shown for COVID-19 patient samples (orange box) and healthy donors (grey box). Data represent mean ± s.e.m., p-value, and two-tailed unpaired Student's t-test. (c) Representative immunofluorescence images of *ex vivo* generated NETs from healthy human neutrophils incubated with healthy donor or COVID-19 plasma and NET degradation capacity of COVID-19 plasma for 3 h. DNA fluorescence was quantified from COVID-19 plasma (n = 36) and healthy donor plasma (n = 24). Data represent mean ± s.e.m., p-value, and two-tailed unpaired Student's t-test. (d) Recombinant FXII activation by NETs was measured by conversion of the chromogenic substrate H-D-Pro-Phe-Arg-p-nitroaniline (S-2302) at the absorption of λ = 405 nm. S-2302 was added either in the presence or absence of DNase1 (Pulmozyme) or the FXIIa inhibitor rHA-infestin-4 (INH). Data represent mean ± s.e.m., p-value, two-tailed unpaired Student's t-test (n = 6 replicates per time point from two independent experiments). Arbitrary units (AU), Scale bar: 25 mm (c). Figure from (1), in the original paper Fig. 4.

4.1.4 NET-induced FXII activation was not reduced by heparin and dexamethasone

Following the *ex vivo* finding that NETs may enhance FXII activation, we tested if heparin or dexamethasone could reduce FXII activation by NETs. Firstly, heparin was added to NETs, since heparin has been shown to dismantle NETs *ex vivo* (67). Unexpectedly, FXII activation was increased in heparin-treated NETs, compared to NETs treated with buffer (**Fig. 9a**). Representative immunofluorescence staining of buffer (CTRL) and heparin-treated NETs showed positive DNA and NE signals, however, H3cit was only detected in buffer, but not heparin-treated NETs (**Fig. 9b**).

Dexamethasone is a glucocorticoid with immunosuppressant and anti-inflammatory effects used in various allergic and inflammatory conditions including COVID-19 (140). To investigate if dexamethasone reduces excessive NET-mediated FXII activation, plasma from COVID-19 patients was pre-treated with dexamethasone (500 ng/mL) before adding it to isolated neutrophils from healthy donors (**Fig. 9c**). Both untreated and dexamethasone pre-treated plasma did not reduce NET-mediated FXII activation. Taken together, heparin and dexamethasone did not diminish thrombo-inflammation *ex vivo*.
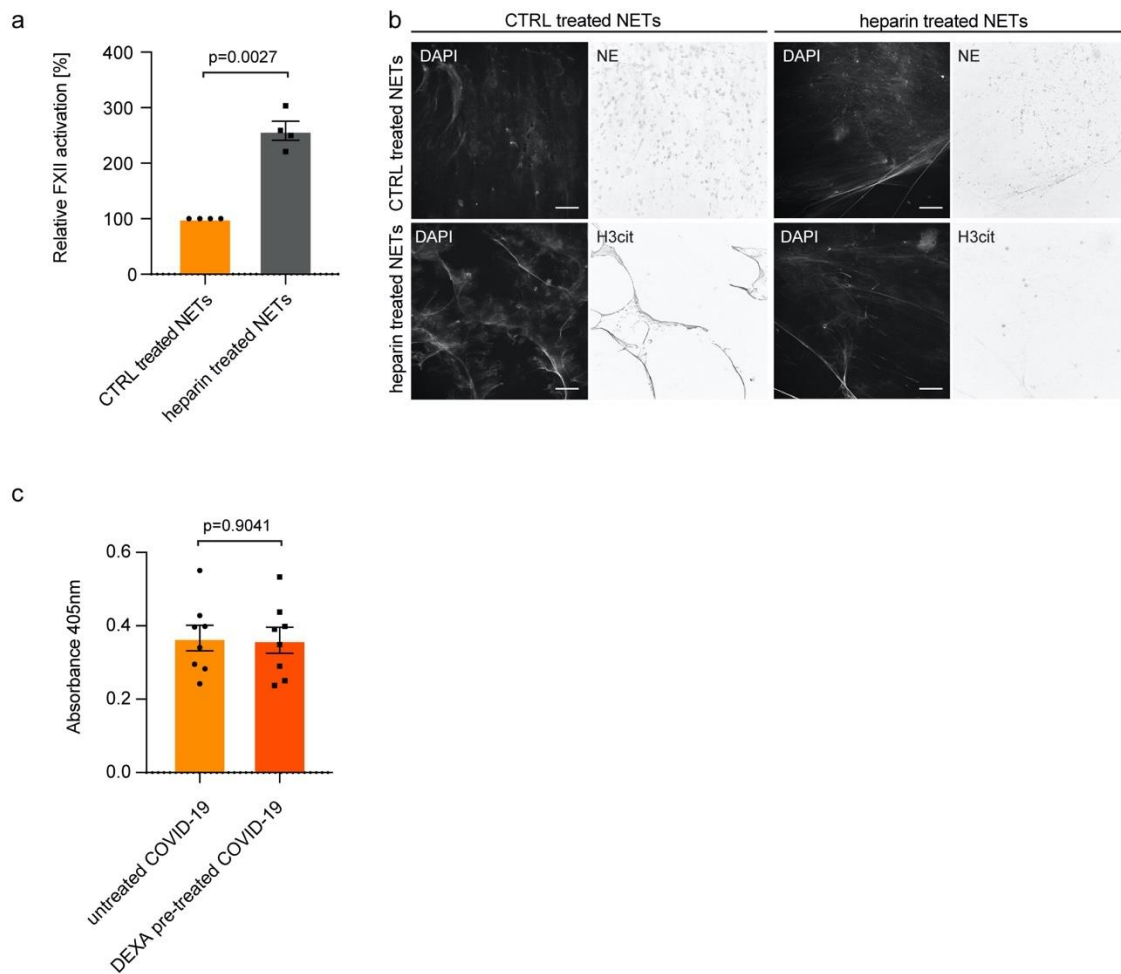
Figure 9. COVID-19 plasma stimulated NET formation and NET-induced FXII activation was not decreased by the addition of heparin or dexamethasone. (a) NETs treated with heparin showed an increased FXIIa generation. NETs were stimulated with PMA and pre-treated with buffer (CTRL) or heparin (100 U/ml) before FXIIa measurement. Data represent mean ± s.e.m., p-value, and one-sample t-test (n = 4 replicates from two independent experiments). (b) Representative immunofluorescence images of NETs activated with PMA and pre-treated with buffer (CTRL) or heparin (100 U/ml). NETs stained with DAPI and NET markers: neutrophil elastase (NE) or citrullinated histone 3 (H3cit) (grey single-channel images), respectively. Scale bar 100 μm. (c) COVID-19 plasma pre-treated with dexamethasone (DEXA, 500 ng/ml, n = 8) or buffer (n = 8) was incubated with healthy neutrophils to perform a kinetic measurement (chromogenic substrate S-2302, 1 mM, absorption λ = 405 nm at 37 °C for 2 h). Data represent mean ± s.e.m., p-value, and two-tailed unpaired Student's t-test. Figure from (1), in the original paper Supplementary Fig. 3.

4.1.5 NETs and FXIIa do not contribute to long COVID pathogenesis

NETosis has been implicated in acute COVID-19 thrombo-inflammation and persistent endotheliopathy (77, 141, 142). We were interested to determine, whether certain thrombo-inflammatory reactions may be sustained in convalescent COVID-19 patients and contribute to long COVID pathogenesis. In this study the long COVID cohort was defined as 1) not hospitalized and symptom-free for at least 6 weeks, or 2) already discharged from the hospital for those requiring admission.

Firstly, we determined levels of the NET and cell death marker ceDNA in plasma from healthy donors and convalescent COVID-19 patients using a fluorescent Sytox Green probe (**Fig. 10a**). ceDNA levels were not significantly different in the cohorts (median ceDNA convalescent COVID-19 0.37 µg/ml, vs. controls 0.37 µg/ml; $p = 0.73$, 95% CI −0.04 to 0.05). Next, we tested DNase activity in healthy and convalescent COVID-19 plasma in an *ex vivo* NET degradation assay. As expected from similar ceDNA concentrations between healthy and convalescent COVID-19 plasma in **Fig. 10a**, no difference in DNase activity was observed (median DNase activity convalescent COVID-19 22,792 arbitrary units (AU) vs. controls 18,835 AU; $p = 0.53$, 95% CI −4,554 to 9,410) (**Fig. 10c**). Finally, we stimulated convalescent COVID-19 patients and healthy donor plasma with kaolin (10 µg/ml), an established anionic substance that is well-known to activate blood clotting in a FXII-dependnet manner *in vitro*. Upon stimulation with kaolin, we measured FXII activation in convalescent COVID-19 and healthy donor plasma. We did not detect differences in stimulated FXIIa levels in convalescent COVID-19 and healthy donor plasma ($p = 0.16$, 95% CI −0.15 to 0.03) (**Fig. 10b**).

We neither found elevated ceDNA levels nor a deficiency in NET degradation in the convalescent COVID-19 plasma. In contrast to acute COVID-19, cell death and NET degradation are in the physiological range in long COVID. Furthermore, we did not detect increased FXIIa levels in convalescent COVID-19 plasma, suggesting unaltered intrinsic coagulation in long COVID. Overall, we found deficient NET degradation and elevated levels of the NETs/FXIIa axis in acute COVID-19, but not in long COVID.
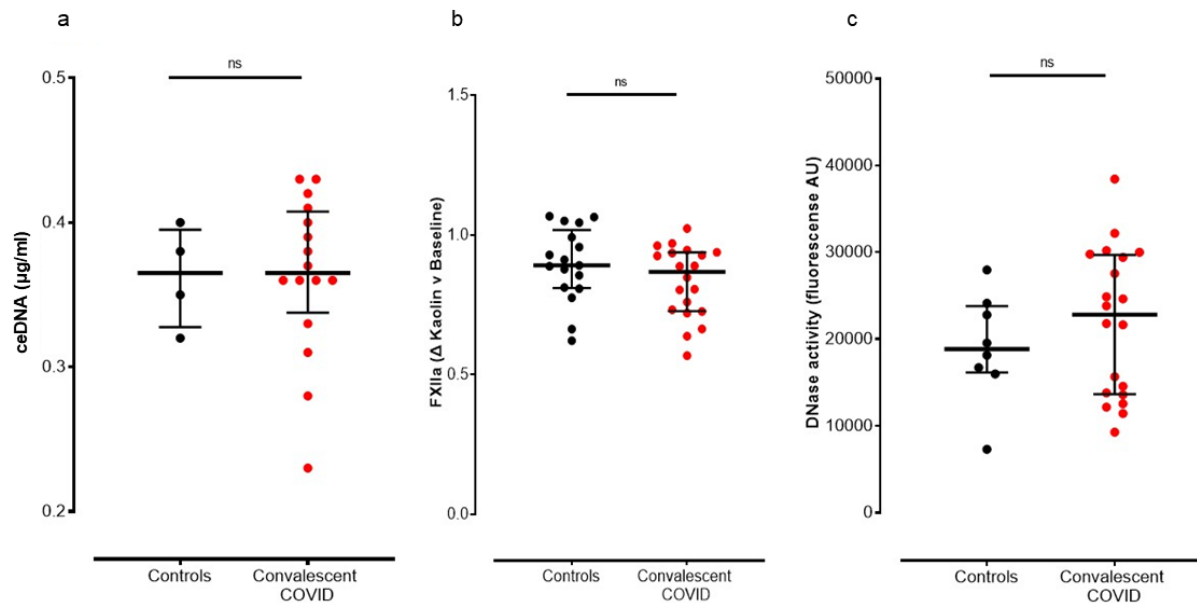
Figure 10. Cell death, FXII activation, and DNase activity were not elevated in long COVID. (a) Circulating extracellular DNA levels in plasma samples from long COVID patients (n = 16) and healthy controls (n = 4). (b) Activation of FXII (via conversion of the chromogenic substrate H-D-Pro-Phe-Arg-p-nitroaniline S-2302) in kaolin-stimulated (10 μg/ml, 2 h) plasma from convalescent COVID-19 patients (n = 20) and healthy controls (n =17). (c) *Ex vivo* NET degradation capacity of plasma from long COVID patients. Quantified DNA fluorescence from long COVID plasma (n = 20) and healthy donor plasma (n = 8) using the dye Sytox Green. Data represent mean ± s.e.m., unpaired Student's t-test. Arbitrary units (AU). Figure from (2), in the original paper Supplementary Fig. 1g, c, and f.

4.1.6 NETs in vaccine-induced immune thrombotic thrombocytopenia-associated cerebral sinus vein thrombosis

Upon the emergence of COVID-19, various vaccination programs were started to fight the ongoing pandemic. AstraZeneca developed a vaccine based on a recombinant chimpanzee adenoviral vector (ChAdOx1-S) encoding the spike glycoprotein of SARS-CoV-2 (ChAdOx1 nCoV-19; Vaxzevria). When the EMA approved vaccine was rolled out, CVST, splanchnic vein thrombosis, and other severe thrombotic events together in conjunction with thrombocytopenia were reported in healthy individuals 5-20 days after the vaccination. These novel vaccine-induced thrombotic complications were categorized under the term VITT. VITT is characterized by high titers of anti-PF4 antibodies, arising against the cationic platelet chemokine PF4 (85). PF4-directed antibodies were rarely found in non-VITT CVST patients, hence they seem to drive post-vaccination VITT and related thrombotic complications (143). In this study, vaccine components forming complexes with PF4, anti-PF4 antibody-driven platelet and granulocyte activation, and NETosis were investigated in VITT patients. The following section will focus on NET formation in serum and brain tissue.
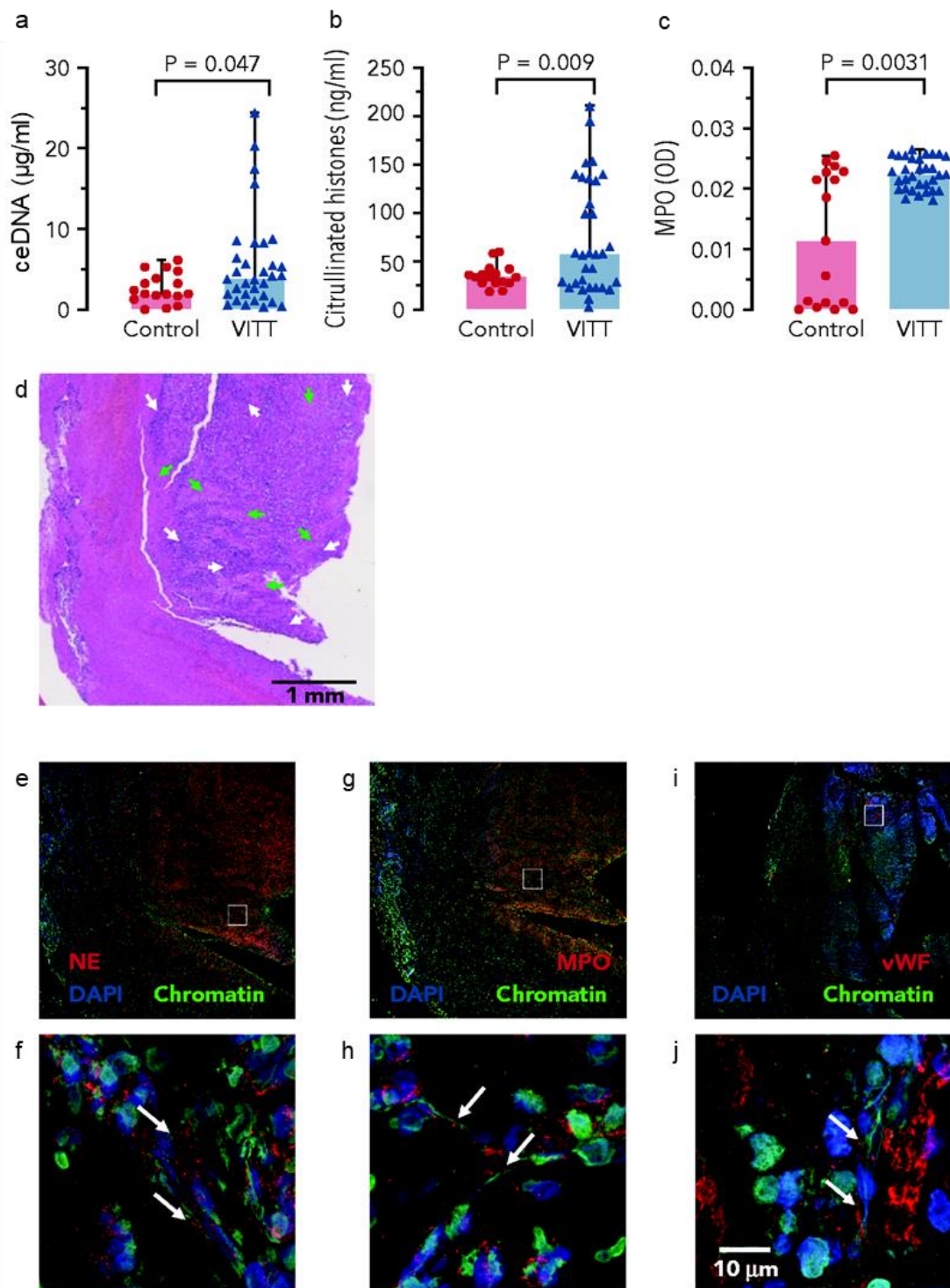
Figure 11. Elevated NET markers in VITT patient serum and cerebral sinus vein thrombi. (a) Circulating extracellular DNA (ceDNA) serum levels of VITT patients and healthy donors using fluorescent DNA-intercalating dye Sytox Green. (b) Citrullinated histone H3 (H3cit) serum levels in VITT patients and healthy donors measured by ELISA. (c) Myeloperoxidase (MPO) serum levels in VITT patients and healthy donors measured by ELISA. (d) H&E staining of a cerebral venous sinus thrombus paraffin section of a VITT patient. Green arrows highlight areas of amorphous fibrin accumulation and white arrows indicate granulocyte-rich areas in the thrombus core. (e-j) Representative

immunohistochemistry of a VITT patient's cerebral sinus vein thrombus stained for NETs using DAPI and antibodies against chromatin (green), and either NE (red, E, and F), MPO (red, G, and H), or vWF (red, I, and J). The detailed view of the sections in panels F, H, and J are depicted as small, white rectangles in panels E, G, and I, respectively. Data represent mean ± s.e.m., p-value, unpaired Student's t-test (a, b) Mann-Whitney test (c). Figure from (3), in the original paper Fig. 6.

To investigate if NET formation is increased in sera and cerebral sinus vein thrombi from VITT patients compared to vaccinated healthy controls, three NET biomarkers were analyzed: ceDNA, H3cit, and MPO (**Fig. 11, a-c**). All three markers were elevated in VITT serum compared to healthy controls. Next, the histology of cerebral sinus vein thrombi, a complication of VITT patients was assessed. A thrombus from one VITT patient was excised by thrombectomy and another thrombus was retrieved during autopsy. The thrombus obtained by thrombectomy displayed fibrin depositions (green arrows) surrounded by nucleated cells (white arrows) (**Fig. 11d**). Immunofluorescence staining of these cell-dense areas revealed an accumulation of activated neutrophils and NETs. Co-staining of the NET markers chromatin and NE (**Fig. 11, e**, and **f**) or chromatin and MPO (**Fig. 11, g**, and **h**) showed elongated DNA strands decorated with granular enzymes (white arrows) within the platelet-rich thrombus (**Fig. 11, i**, and **j**). The cerebral sinus vein thrombus retrieved during autopsy showed similar NET structures compared to the thrombus of the first patient. The thrombus contained large strands of DNA (chromatin staining in green), decorated with MPO, derived from the azurophilic granules in neutrophils (MPO staining in red). Upon comparing cerebral venous sinus thrombus regions of the vaccinated patient (A and A') and a non-vaccinated control patient (B and B'), fewer neutrophils were visible in the control section (**Fig. 12**). Taken together, my data show that NETs are present in thrombus tissue and plasma from patients with VITT-induced CVST, potentially exacerbating prothrombotic processes in VITT patients.
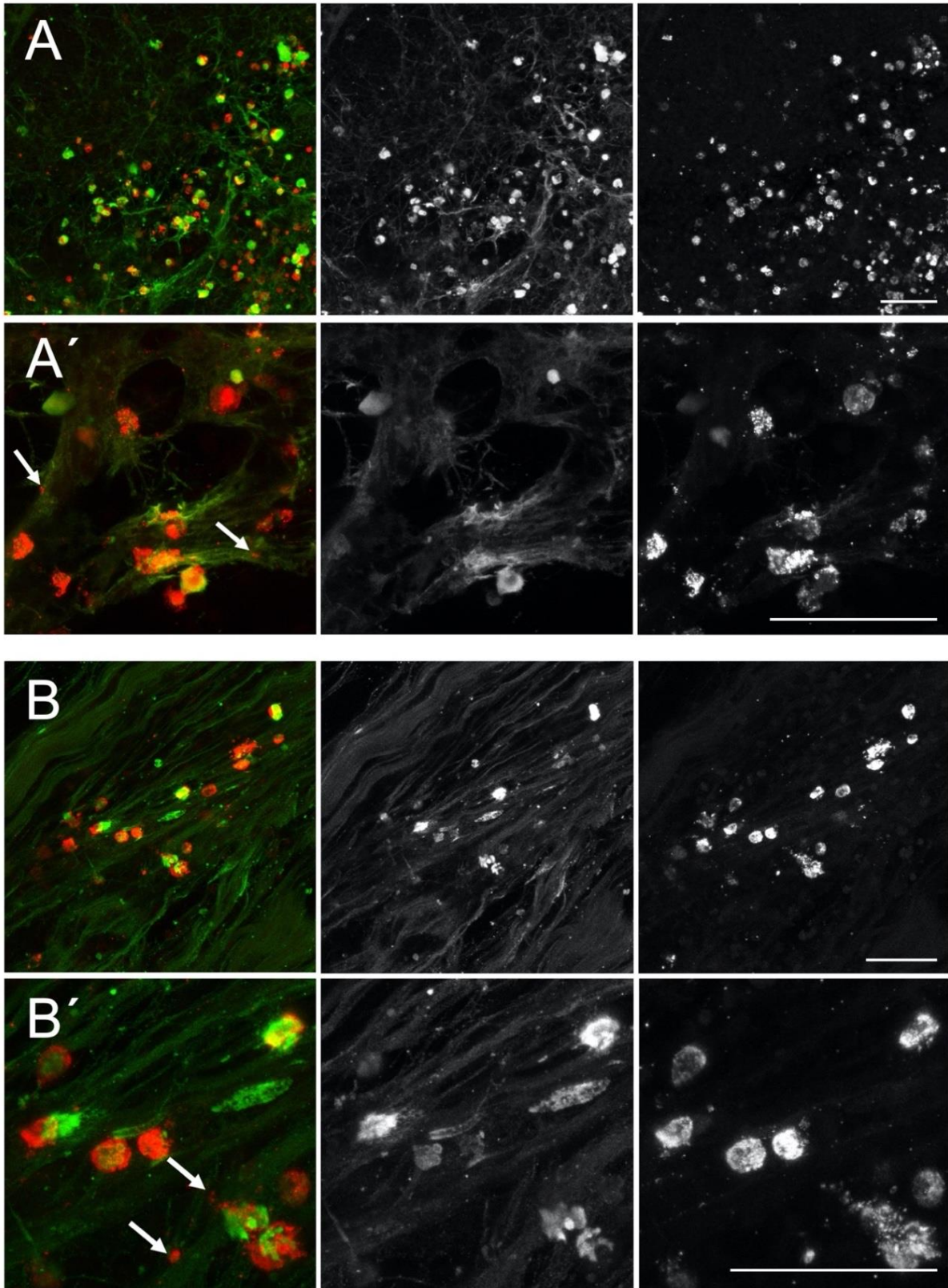
Figure 12. NETs in CVST tissue of VITT patient. Immunofluorescence staining of 100 µm transverse vibratome sections from an autopsy-derived CVST (A, A´) and a VITT-independent CVST (B, B´). Brain tissue was obtained by autopsy. Sections were stained with antibodies against chromatin (green or grey in single channel images) and myeloperoxidase (MPO) (red or grey in single channel images). White

arrows point to NET structures where MPO co-localizes with chromatin. Scale bars: 50 μm (A, B), 10 μm (A´, B´). Figure from (3), in the original paper Supplemental Fig. S5.

4.2 NET formation drives vascular occlusions independent of PAD4 and GSDMD

To investigate the molecular mechanisms of NET formation, we analyzed the role of MYD88, GSDMD, and PAD4 in two previously described NET-driven vaso-occlusive murine models (92). Firstly, the *chronic neutrophilia model* was generated to investigate experimental neutrophil-driven inflammation in mice. Mice have a lower neutrophil count compared to humans. To "humanize" mouse neutrophil counts *Csf3* which encodes for G-CSF was hydrodynamically injected into the tail vein using the long-term gene expression pLIVE vector. Mice deficient in DNase1 and DNase1L3 (*D1/D1l3*$^{-/-}$) that overexpress G-CSF died rapidly from intravascular DNA-rich clots as revealed by H&E staining (92). Secondly, the *septicemia model* was generated to serve as a more physiological model (92). Sepsis or septicemia is an acute systemic reaction to an infection that has been shown to cause intravascular NET formation (38, 144).

D1/D1l3$^{-/-}$ mice were injected with LPS and *E. coli*, resulting in mortality and intravascular NET clot formation similar to the sterile neutrophilia model (92). Based on the finding that *D1/D1l3*$^{-/-}$ mice show increased mortality due to vascular occlusions in both models (92), we tested mice with a triple deficiency to identify critical proteins of NETosis in this study. The mice had a deficiency in DNase1, DNase1L3, and additionally in the protein of interest, i.e., MYD88, GSDMD, and PAD4. *Myd88/D1/D1l3*$^{-/-}$, *Gsdmd/D1/D1l3*$^{-/-}$, and *Pad4/D1/D1l3*$^{-/-}$ mice were subjected to chronic neutrophilia and septicemia and analyzed for survival, body weight, body temperature, and histological staining of the lungs.

4.2.1 MYD88 is required for septicemia, but not sterile neutrophilia triggered NETosis

MYD88 is an adaptor protein for inflammatory signaling pathways downstream of TLR and IL-1 receptor families. MYD88 is the central node of a multitude of inflammatory pathways, causing the activation of NF-κB, MAPK, and activator protein 1 (145). We

analyzed the importance of MYD88 for NET formation using our two distinct models of NET-driven venous thrombosis with the formation of microvascular occlusions: 1) septicemia, and 2) sterile neutrophilia. We expected that LPS would not be sensed downstream of TLRs and thus result in the survival of MYD88-deficient mice during septicemia, as previously shown (146). We sacrificed the animals when they showed defined signs of distress combined with severe hypothermia and hematuria, or latest on day 14 for WT animals, and performed histology analysis.

As a proof-of-concept experiment, we investigated if $Myd88/D1/D1l3^{-/-}$ mice are protected from lethal vascular NET occlusions during septicemia. As expected, all $Myd88/D1/D1l3^{-/-}$ mice (n = 7/7) survived the LPS/ $E.\ coli$ challenge. In contrast, more than half (n = 4/7) of $D1/D1l3^{-/-}$ mice died during septicemia while WT mice with intact NET-degrading capacity were protected (n = 7/7) (**Fig. 13A**). Progressive hypothermia (median -2.51 °C, interquartile range (IQR) -3.80 (25% percentile), 0.08 (75% percentile)) and drop in body weight (median -3.09 g, IQR -3.78, -2.01) preceded the death of $D1/D1l3^{-/-}$ animals, whereas surviving mice recovered from hypothermia within five days after treatment (**Figs. 13, B and C**). In contrast, $Myd88/D1/D1l3^{-/-}$ mice did not show a significant change in peripheral body temperature (median -0.18 °C, IQR -0.75, 0.18, $p > 0.05$) as compared to $D1/D1l3^{-/-}$ mice. $Myd88/D1/D1l3^{-/-}$ mice lost significantly less body weight (median -0.23 g, IQR -0.61, -0.01, $p = 0.0096$) than $D1/D1l3^{-/-}$ mice in the septicemia challenge.

In the TLR signaling-independent sterile neutrophilia NET formation model, MYD88 deficiency did not provide protection, and mortality was similar in $Myd88/D1/D1l3^{-/-}$ and $D1/D1l3^{-/-}$ animals (n = 4/4 vs. n = 7/7, respectively, **Fig. 13D**). Mortality in both genotypes was associated with a similar magnitude of hypothermia ($Myd88/D1/D1l3^{-/-}$: median -0.71 °C, IQR -2.24, -0.35 vs. $D1/D1l3^{-/-}$: median 0.19 °C, IQR -2.60, 0.60, $p > 0.05$, **Fig. 13E**). Consistent with published data (92), none of the WT mice (n = 0/6) died and we measured only a minor drop in body temperature upon $Csf3$ treatment. The number of occluded pulmonary vessels increased > 2-fold in $Myd88/D1/D1l3^{-/-}$ over $D1/D1l3^{-/-}$ mice (median 6.00 occluded vessels/all field-of-views (FOVs), IQR 2.00, 8.00 vs. median 3.00 occluded vessels/all FOVs, IQR 2.00, 5.00, respectively, $p = 0.0075$, **Fig. 13F**). The occlusive material blocking the vessel lumen was rich in long DNA strands (arrow) and the meshwork trapped erythrocytes and

leukocytes (**Fig. 13G**). Strong immunohistochemistry signals for the NET markers H3cit, MPO, and chromatin confirmed NET formation in the pulmonary vasculature in *Myd88/D1/D1l3*^{-/-} and *D1/D1l3*^{-/-} mice (**Figs. 13, H and I**).
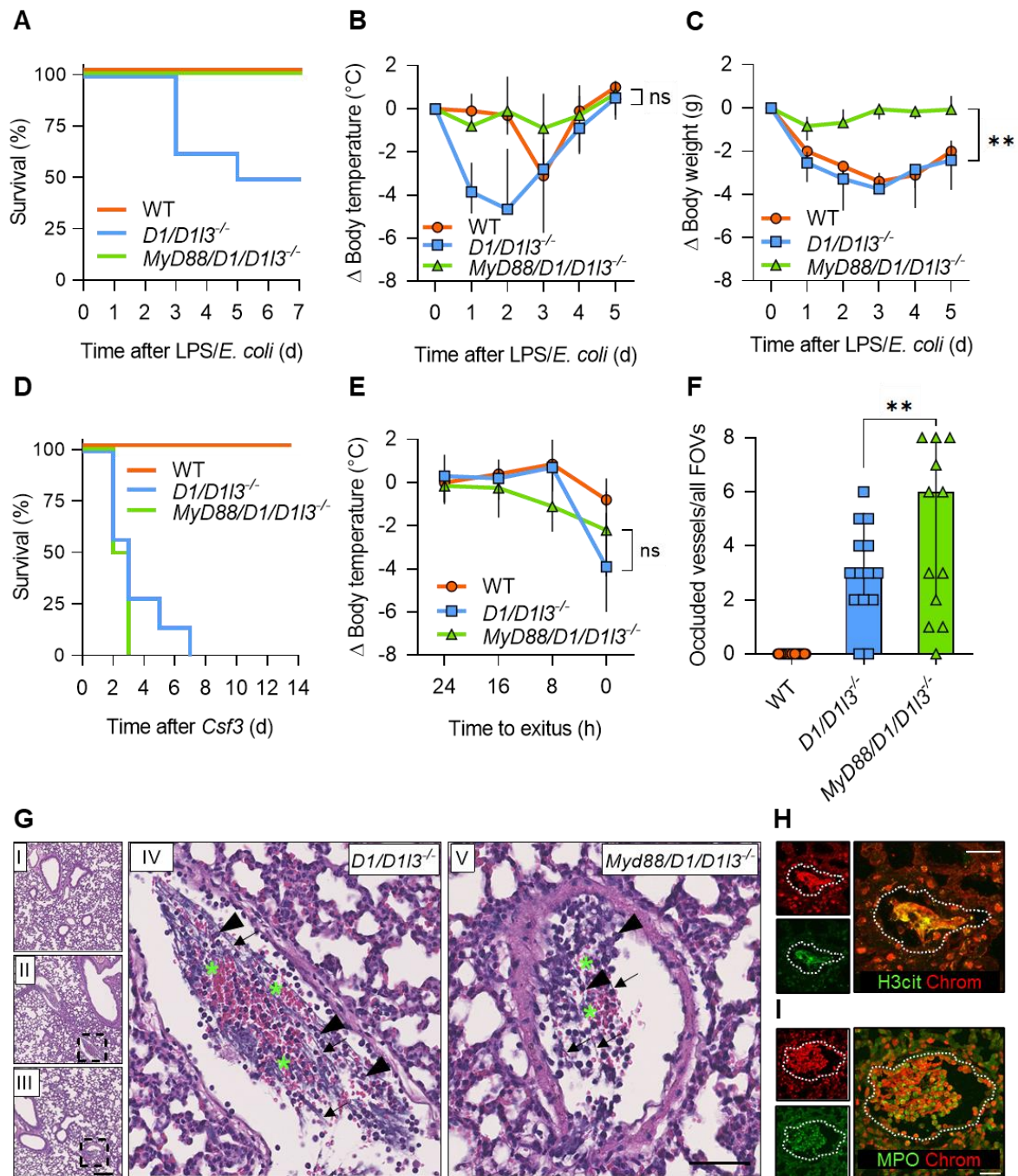
Figure 13. MYD88 is required for septicemia but not neutrophilia-driven intravascular NET formation. *Myd88/D1/D1l3*^{-/-}, *D1/D1l3*^{-/-}, and WT mice were i.p. injected with lipopolysaccharide (LPS, 3-times, 1 µg/g) and i.v. with 1.5 x 10^{7} heat-killed *E. coli* (**A-C**) or challenged by chronic neutrophilia induced by hydrodynamic tail vein injection of a G-CSF-expressing plasmid (**D-I**). Survival (**A, D**), peripheral body temperature following LPS/*E. coli* infusions or *Csf3* expression (**B, E**) and body weight (**C**) of challenged mice is given. Histological analysis of *Myd88/D1/D1l3*^{-/-} *and D1/D1l3*^{-/-} mice that ectopically expressed *Csf3* (**F-I**). H&E staining of murine lungs. A pulmonary blood vessel of *Csf3* over-

58

expressing mice show hematoxylin-rich clots, long DNA filaments (arrow) with entrapped erythrocytes (asterisk), and leukocyte nuclei (arrowhead). Scale bars, 250 µm (overview) and 50 µm (zoom-in view). Upper left overview **I** depicts an H&E-stained lung of a WT mouse. **II** is the overview of **IV** of a *D1/D1l3*$^{-/-}$ mouse lung and **III** is the overview of **V** of a *Myd88/D1/D1l3*$^{-/-}$ mouse lung (**G**). Quantification of blood vessels in lungs occluded by hematoxylin-positive clots per field-of-view (FOV) in *Myd88/D1/D1l3*$^{-/-}$, *D1/D1l3*$^{-/-}$ and WT mice, 5 FOVs/lung (**F**). Immunostaining of occluded blood vessels for chromatin (red) and the neutrophil markers H3cit and MPO (green, **H, I**). Scale bars, 25 µm. Representative images from four mice. Dotted lines indicate the vessel wall. Data is represented as median and interquartile range (IQR). (B, C, E) Two-way ANOVA after 5 days or time point 0 h, (F) one-way ANOVA. * $p < 0.05$, ** $p < 0.01$, *** $p < 0.001$.

4.2.2 Vessel occlusive NETosis proceeds in the absence of GSDMD in septicemia and sterile neutrophilia

GSDMD forms membrane pores that can promote cytolysis and the release of IL-1 family cytokines (147). GSDMD is also known to be the key mediator of pyroptotic cell death (148) and has been associated with NETosis in recent years (61). GSDMD is believed to be required for NET formation and both *Gsdmd* gene ablation and pharmacological inhibition of GSDMD have been shown to interfere with NET formation in mouse models of lethal sepsis (58). Based on these findings, we aimed to investigate the role of GSDMD in our NET-induced vascular occlusion models, septicemia and sterile neutrophilia. We targeted *Gsdmd* in *D1/D1l3*$^{-/-}$ mouse-derived embryonic stem cells using CRISPR/Cas9 technology and deleted the second coding exon (exon 3) of 193 base pairs (bp), resulting in a frameshift and a truncated protein of 73 amino acids (**Fig. 14A**). Quantitative PCR confirmed absent *Gsdmd* messenger RNA (mRNA) expression in *Gsdmd/D1/D1l3*$^{-/-}$ mice (**Fig. 14B**). Consistently, immunoblot analysis using antibodies that detect both the full-size protein at an apparent molecular weight of ~ 53 kDa and its proteolytic N- and C-terminal fragments at ~ 31 and ~ 22 kDa, respectively, confirmed complete absence of GSDMD protein in *Gsdmd/D1/D1l3*$^{-/-}$ bone marrow cells (**Fig. 14C**). Development, size, and body weight of *Gsdmd/D1/D1l3*$^{-/-}$ mice did not show obvious differences compared to age and sex-matched *D1/D1l3*$^{-/-}$ or WT mice and animals appeared phenotypically normal under standard conditions.
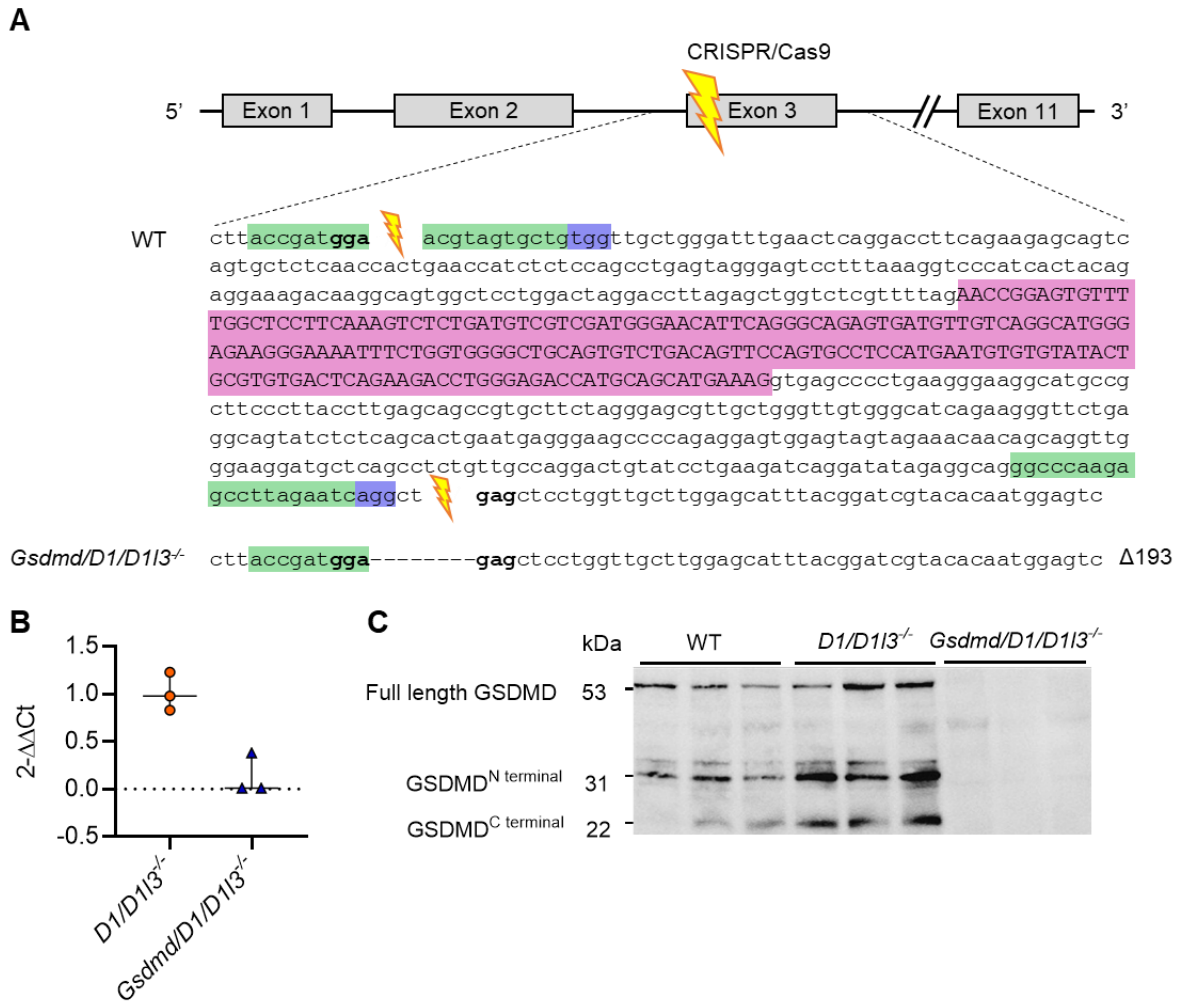
Figure 14. CRISPR/Cas9 gene disruption generates *Gsdmd*⁻/⁻ mice. (**A**) Scheme showing the CRISPR/Cas9-mediated gene targeting strategy to generate *Gsdmd*⁻/⁻ mice. Sequence of the Gsdmd allele in WT and *Gsdmd*⁻/⁻ mice with the intron-flanking single guide RNA (sgRNA) targeting exon 3 (2nd coding exon) (green), target sequence (pink), and protospacer adjacent motif (PAM, purple) are depicted. Double-strand breakage by CRISPR/Cas9 followed by non-homologous end joining resulted in the deletion of 193 base pairs (bp) long exon 3. (**B**) *Gsdmd* mRNA expression from *Gsdmd/D1/D1l3*⁻/⁻ and *D1/D1l3*⁻/⁻ tail biopsies. (**C**) Lysed bone marrow cells isolated from *Gsdmd/D1/D1l3*⁻/⁻, *D1/D1l3*⁻/⁻, and WT mice were analyzed by western blotting using a polyclonal anti-GSDMD antibody. Equal protein loading of 20 µg/lane, n = 3 animals/genotype. Data is represented as median and interquartile range (IQR).

Next, I compared *Gsdmd/D1/D1l3*⁻/⁻ and *D1/D1l3*⁻/⁻ mice in our two NET formation models and found that mortality upon i.v. LPS/ i.p. *E. coli* challenge was not different in *Gsdmd/D1/D1l3*⁻/⁻ and *D1/D1l3*⁻/⁻ mice (n = 9/11 vs. n = 10/11 failed to survive, p>0.05, **Fig. 15A**). Independent of the absence or presence of GSDMD >80% of challenged mice succumbed to septicemia within the first 48 h after LPS-injection. In contrast, all WT control mice survived experimental sepsis (n = 7/7). Next, we analyzed

the lung vasculature of challenged mice. H&E-stained tissue sections showed large vessel occlusive thrombi in the lungs of *Gsdmd/D1/D1l3*^{-/-} and *D1/D1l3*^{-/-} mice (**Fig. 15C**). The number of vascular occlusions was similar between the two mouse lines (*Gsdmd/D1/D1l3*^{-/-}: median 1.00 occluded vessels/all FOVs, IQR 0.00, 2.00 vs. *D1/D1l3*^{-/-}: median 1.00 occluded vessels/all FOVs, IQR 0.00, 2.00, respectively, *p* > 0.05, **Fig. 15B**). In contrast, there were no thrombi detectable in challenged WT mice, confirming the critical role of circulating DNases for NET clearance. Vascular occlusive thrombi, both in *Gsdmd/D1/D1l3*^{-/-} and *D1/D1l3*^{-/-} mice, were rich in neutrophils and acidic filamentous structures. The pulmonary occlusions stained strongly positive for the NET biomarkers H3cit and MPO, each colocalizing with extracellular chromatin in immunohistochemical analyses (**Figs. 15, D and E**).

I aimed to confirm the unexpected redundancy of GSDMD in the second model of NET-mediated vascular occlusions, which is driven by spontaneous NET formation in sterile neutrophilia (92). In sterile neutrophilia-induced thrombosis, the lethality of both *Gsdmd/D1/D1l3*^{-/-} and *D1/D1l3*^{-/-} mice was high with > 90% dying within 6 days after ectopic *Csf3* overexpression and mortality was not significantly different among the two mouse lines (n = 6/6 and n = 12/13, **Fig. 15F**). In contrast, all (n = 6/6) WT mice survived the sterile neutrophilia challenge. A severe and rapidly progressing hypothermia of comparable degree preceded the decease of both *Gsdmd/D1/D1l3*^{-/-} and *D1/D1l3*^{-/-} mice (*Gsdmd/D1/D1l3*^{-/-}: median -0.43 °C, IQR -3.10, -0.32 vs. *D1/D1l3*^{-/-}: median 0.35 °C, IQR -1.86, 0.78, **Fig. 15G**). In contrast, peripheral body temperature did not change significantly in challenged WT mice (median 0.16 °C, IQR -0.36, 0.60). These findings were further validated by a reduction in body weight of *Gsdmd/D1/D1l3*^{-/-} and *D1/D1l3*^{-/-} mice (*Gsdmd/D1/D1l3*^{-/-}: median -1.16 g, IQR -2.13, -0.21 vs. *D1/D1l3*^{-/-}: median -0.57 g, IQR -0.88, -0.03, **Fig. 15H**). In line with the findings from the septicemia model, vascular clot formation did not show significant differences between challenged *Gsdmd/D1/D1l3*^{-/-} and *D1/D1l3*^{-/-} mice (median 6.00 occluded vessels/all FOVs, IQR 4.00, 9.75 vs. median 6.00 occluded vessels/all FOVs, IQR 4.25, 9.75, respectively, **Fig. 15I**). Vascular occlusions were rich in NETs as revealed by immunohistochemistry signals for chromatin, H3cit and MPO (**Figs. 15, K** and **L**).
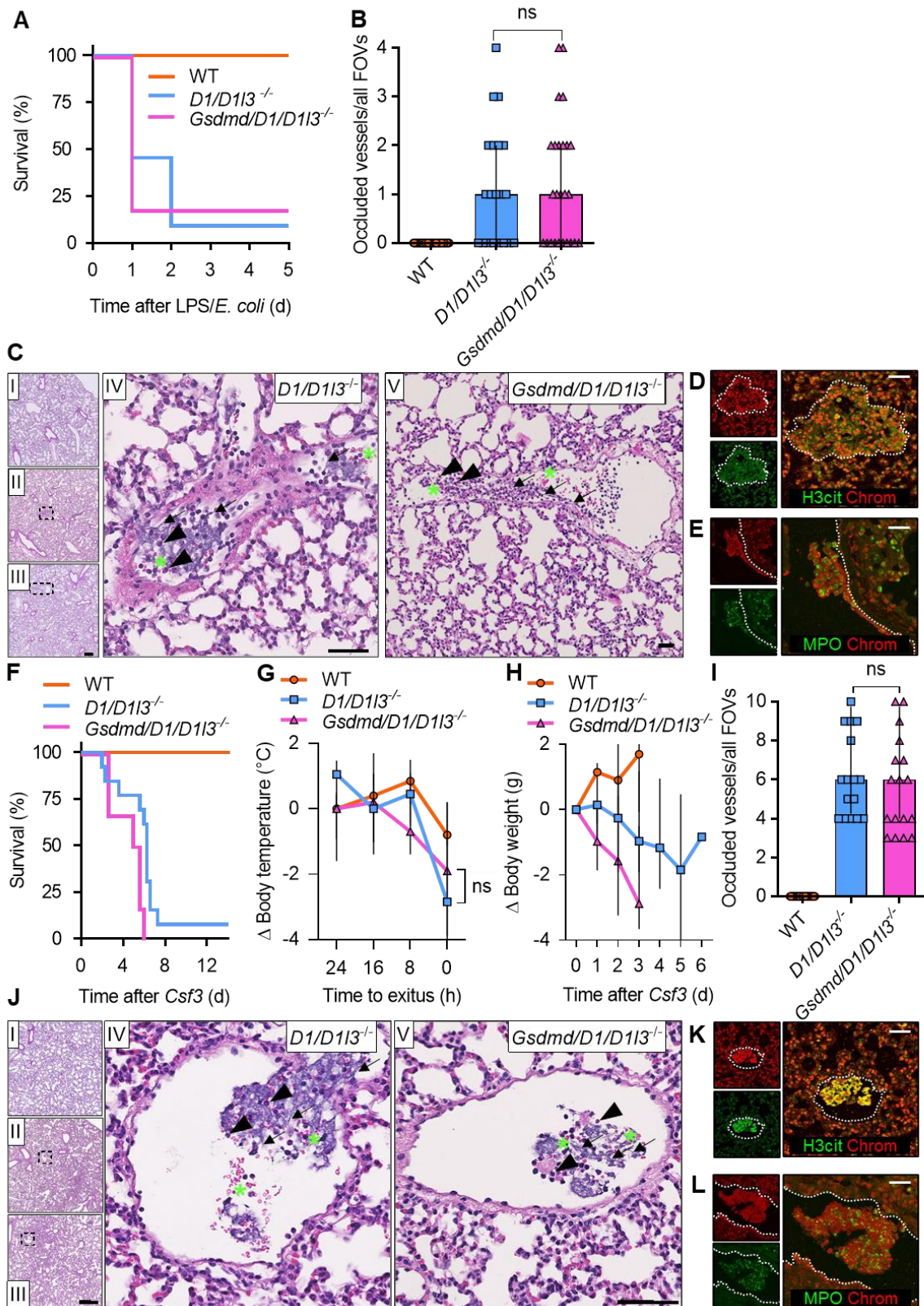
Figure 15. Vessel occlusive NET formation in septicemia and sterile neutrophilia is independent of GSDMD. *Gsdmd/D1/D1l3*$^{-/-}$, *D1/D1l3*$^{-/-}$, and WT mice were challenged with LPS/*E. coli* (**A-E**) or *Csf3* overexpression (**F-L**) as shown in Fig. 1. Survival (**A, F**), change in peripheral body temperature 24 h prior to exitus (**G**), and change in body weight (**H**) of challenged mice. Histological analysis of

Gsdmd/D1/D1l3^-/- and *D1/D1l3^-/-* mice following experimental septicemia or neutrophilia challenge (**B-E, I-L**). H&E-stained lung sections revealed occluded pulmonary vessels. Hematoxylin-rich clots occluding vessels are made up of long DNA filaments (arrow) with entrapped erythrocytes (asterisk), and leukocytes (arrowhead). Scale bars, 250 µm (overview), **IV** 50 µm, and **V** 125 µm (zoom-in view). Upper left overview **I** depicts an H&E-stained lung of a WT mouse. **II** is the overview of **IV** of a *D1/D1l3^-/-* mouse lung and **III** is the overview of **V** of a *Gsdmd/D1/D1l3^-/-* mouse lung. (**C, J**). Quantification of occluded blood vessels in lungs per field-of-view (FOV) in *Gsdmd/D1/D1l3^-/-*, *D1/D1l3^-/-* and WT mice, 5 FOVs/lung (**B, I**). Immunofluorescence images of occluded vessels stained for chromatin (red), H3cit and MPO (green, **D, K** and **E, L**). Scale bars, 25 µm. Representative images from n = 4 mice. Dotted lines indicate the vessel wall. Data is represented as median and interquartile range (IQR). (B, I) Kruskal-Wallis test, (G) two-way ANOVA at time point 0 h. * $p < 0.05$, ** $p < 0.01$, *** $p < 0.001$.

4.2.3 PAD4 is dispensable for vessel occlusive NETosis in septicemia and sterile neutrophilia

D1/D1l3^-/- mice develop intravascular occlusions composed of entrapped erythrocytes, long DNA strands and citrullinated histones from neutrophils that underwent NETosis (92). PAD4 catalyzes the conversion of arginine to citrulline residues. During NETosis, PAD4 citrullinates histones leading to chromatin unfolding, which is commonly believed to be a crucial step in NET formation. Thus, PAD4 may be a promising target for the inhibition of histone citrullination and prevention of NET formation. We generated *Pad4/D1/D1l3^-/-* mice to analyze the role of PAD4 in vessel occlusive NET formation during septicemia-triggered thrombosis. *Pad4/D1/D1l3^-/-* mice and *D1/D1l3^-/-* control animals were similarly susceptible to septicemia with 9/9 and 7/9 of the challenged mice dying within 4 days (**Fig. 16A**). In contrast, all (n = 7/7) WT mice survived septicemia. In line with survival, *Pad4/D1/D1l3^-/-* mice experienced a rapid drop in body weight, whereas surviving *D1/D1l3^-/-* and WT control mice remained a more stable body temperature and recovered after 4 days (*Pad4/D1/D1l3^-/-*: median -3.85 g, IQR -7.08, -0.80, *D1/D1l3^-/-*: median -3.16 °C, IQR -4.02, -1.83, WT: median -2.28 g, IQR -3.00, -1.38, **Fig. 16B**). Numbers of occluded pulmonary vessels were not significantly different in *Pad4/D1/D1l3^-/-* and *D1/D1l3^-/-* animals (median 2.00 occluded vessels/all FOVs, IQR 0.00, 3.00 vs. median 3.00 occluded vessels/all FOVs, IQR 1.00, 4.00, respectively), while vascular occlusions were virtually absent in WT mice (**Fig. 16C**). Occlusive thrombi in the two lines appeared morphologically similar and were rich in DNA filaments and polynucleated cells (**Fig. 16D**). *Pad4/D1/D1l3^-/-* lung tissue sections

stained positive for MPO and chromatin in immunohistochemistry (**Fig. 16F**). As expected, pulmonary thrombi in *Pad4/D1/D1l3*$^{-/-}$ animals were defective in histone citrullination as revealed by a complete loss of H3cit signal in immunohistochemistry (**Fig. 16E**).

Spontaneous NET formation in the neutrophilia model showed that PAD4 deficiency can be overcome in vascular occlusive NET formation. Independent of PAD4 expression, all *Pad4/D1/D1l3*$^{-/-}$ (n = 7/7) and *D1/D1l3*$^{-/-}$ (n = 6/6) mice died within six days after *Csf3* overexpression, while WT mice (n = 6/6) survived the challenge (**Fig. 16G**). Concomitant to survival data a significant drop in body temperature preceded mortality by 8 h which was similarly reduced both in *Pad4/D1/D1l3*$^{-/-}$ and *D1/D1l3*$^{-/-}$ mice (median -1.01 °C, IQR -2.31, 0.12 vs. median -0.33 °C, IQR -3.07, 0.27). In contrast temperature in WT mice remained stable (median 0.16 °C, IQR -0.36, 0.60, **Fig. 16H**). *Pad4/D1/D1l3*$^{-/-}$ and *D1/D1l3*$^{-/-}$ mice (median -0.11 g, IQR -0.60, 0.14, vs. median -0.10, IQR -0.85, 0.03) dropped in body weight, whereas WT animals (WT: median 0.58 g, IQR 0.10, 1.00) even increased in body weight upon neutrophilia (**Fig. 16I**). Counting vascular occlusions in H&E-stained lung sections showed that the number of thrombi in *Pad4/D1/D1l3*$^{-/-}$ was not significantly different compared to *D1/D1l3*$^{-/-}$ control mice (median 6.00 occluded vessels/all FOVs, IQR 2.50, 8.50 vs. median 5.00 occluded vessels/all FOVs, IQR 1.50, 8.50, respectively, **Figs. 16, J** and **K**). In contrast, WT mice did not develop any thrombi and lung sections were virtually free of occlusions (**Figs. 16, J** and **K**). Immunohistochemistry of lung sections indicated that pulmonary occlusions contained NETs and stained for chromatin and MPO but not H3cit in *Pad4/D1/D1l3*$^{-/-}$ mice (**Figs. 16, L** and **M**).
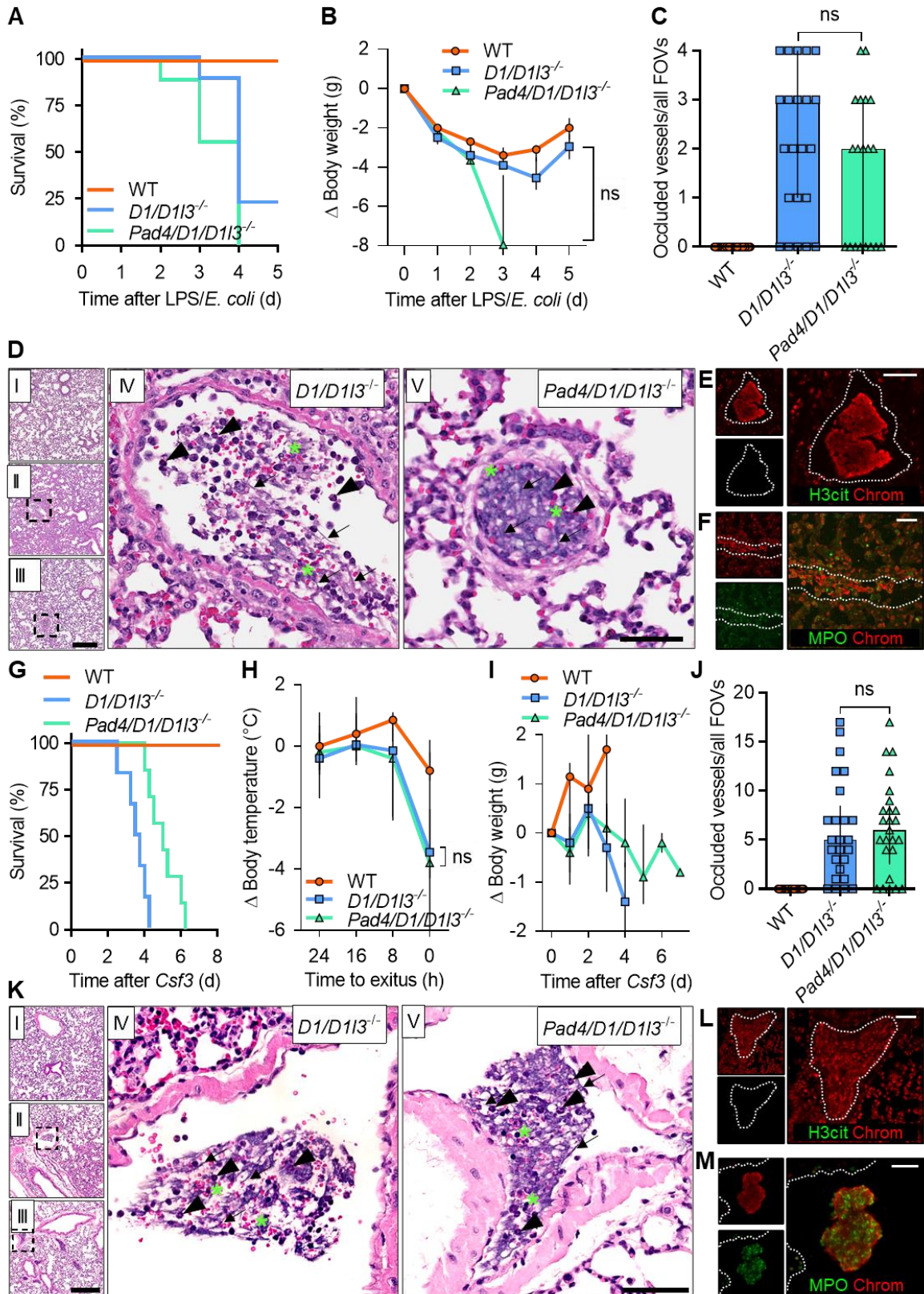
Figure 16. PAD4 deficiency allows for intravascular NET formation in septicemia and sterile neutrophilia. *Pad4/D1/D1l3*^{-/-}, *D1/D1l3*^{-/-}, and WT mice were challenged by LPS/*E. coli* infusions (**A-F**) or *Csf3* overexpression (**G-M**) as given in Figs. 1 and 3. Survival (**A, G**), change in body weight (**B, I**), and temperature 24 h prior to exitus (**H**). H&E-stained lung sections showed occluded vessels with clots

comprised of DNA filaments (arrow), erythrocytes (asterisk), and leukocytes (arrowhead). Scale bars, 250 μm (overview) and 50 μm (zoom-in view). Upper left overview **I** depicts an H&E-stained lung of a WT mouse. **II** shows the overview of **IV** of a *D1/D1l3$^{-/-}$* mouse lung and **III** is the overview of **V** of a *Pad4/D1/D1l3$^{-/-}$* mouse lung (**D, K**). Number of occluded blood vessels in lungs per field-of-view (FOV) in *Pad4/D1/D1l3$^{-/-}$ and D1/D1l3$^{-/-}$* mice, 5 FOVs/lung (**C, J**). Immunofluorescence images of vessel-occluding aggregates show positive co-staining for chromatin (red) and H3cit or MPO (green, **E, L** and **F, M**). Scale bars, 25 μm, n = 4. Dotted lines indicate the vessel wall. Data is represented as median and interquartile range (IQR). (B, C, J) Kruskal-Wallis test after 3 days (B), (H) two-way ANOVA at time point 0 h. * $p < 0.05$, ** $p < 0.01$, *** $p < 0.001$.

4.2.4 Targeting GSDMD but not PAD4 blocks PMA-induced NETosis

Next, we inhibited GSDMD and PAD4 in isolated neutrophils to block NET formation in response to the activators PMA and the Ca^{2+} ionophore A23187. A23187 causes rapid calcium influx through the plasma membrane leading to neutrophil activation with the extrusion of DNA in a process that differs from NADPH oxidase-dependent NET formation induced by PMA (149). Neutrophils isolated from *D1/D1l3$^{-/-}$*, *Pad4/D1/D1l3$^{-/-}$*, or *Gsdmd/D1/D1l3$^{-/-}$* mice similarly formed NETs upon A23187 stimulation at 4 h, as shown by immunohistochemistry staining of the NET markers DNA, MPO and H3cit, as well as brightfield microscopy (**Fig. 17, A, B,** and **D**). DNase1 treatment (10 U/ml) completely dissolved these formed aggregates (data not shown).

PMA stimulated NET formation in *Pad4/D1/D1l3$^{-/-}$* neutrophils, however no NETs formed upon PMA activation in *Gsdmd/D1/D1l3$^{-/-}$* neutrophils (*Pad4/D1/D1l3$^{-/-}$*: median clot area of 1.68 kpx², IQR 1.43, 2.21, **Figs. 17, B** and **C**; vs. *Gsdmd/D1/D1l3$^{-/-}$*: median clot area of 0.0 kpx², IQR 0.0, 0.0; $p = 0.0004$, **Figs. 17, D** and **E**). To test if combined targeting of PAD4 and GSDMD has an effect on NET formation, we pharmacologically inhibited GSDMD activity (NSA, 10 μM) in PAD4 deficient neutrophils. Targeting GSDMD abolished NET formation upon PMA-, but not A23187-treatment in PAD4 deficient neutrophils (PMA+NSA: median 0.0 kpx², IQR 0.0, 0.0; vs. A23187+NSA: median 3.24 kpx², IQR 2.76, 3.52, $p < 0.0001$, **Figs. 17, B** and **C**). In contrast, interference with PAD4 activity using GSK484 (5 μM) failed to significantly reduce A23187-activated NET formation in GSDMD deficient neutrophils (A23187: median 9.18 kpx², IQR 2.39, 11.58 vs. A23187+GSK484: median 10.18 kpx², IQR 7.73, 11.10, **Figs. 17, D** and **E**). Together the data show that GSDMD is required

for PMA-mediated NET formation *ex vivo* but not sepsis or neutrophilia-associated NET formation *in vivo*. Furthermore, the data show that findings obtained for NETosis *ex vivo* require confirmation in *in vivo* settings.
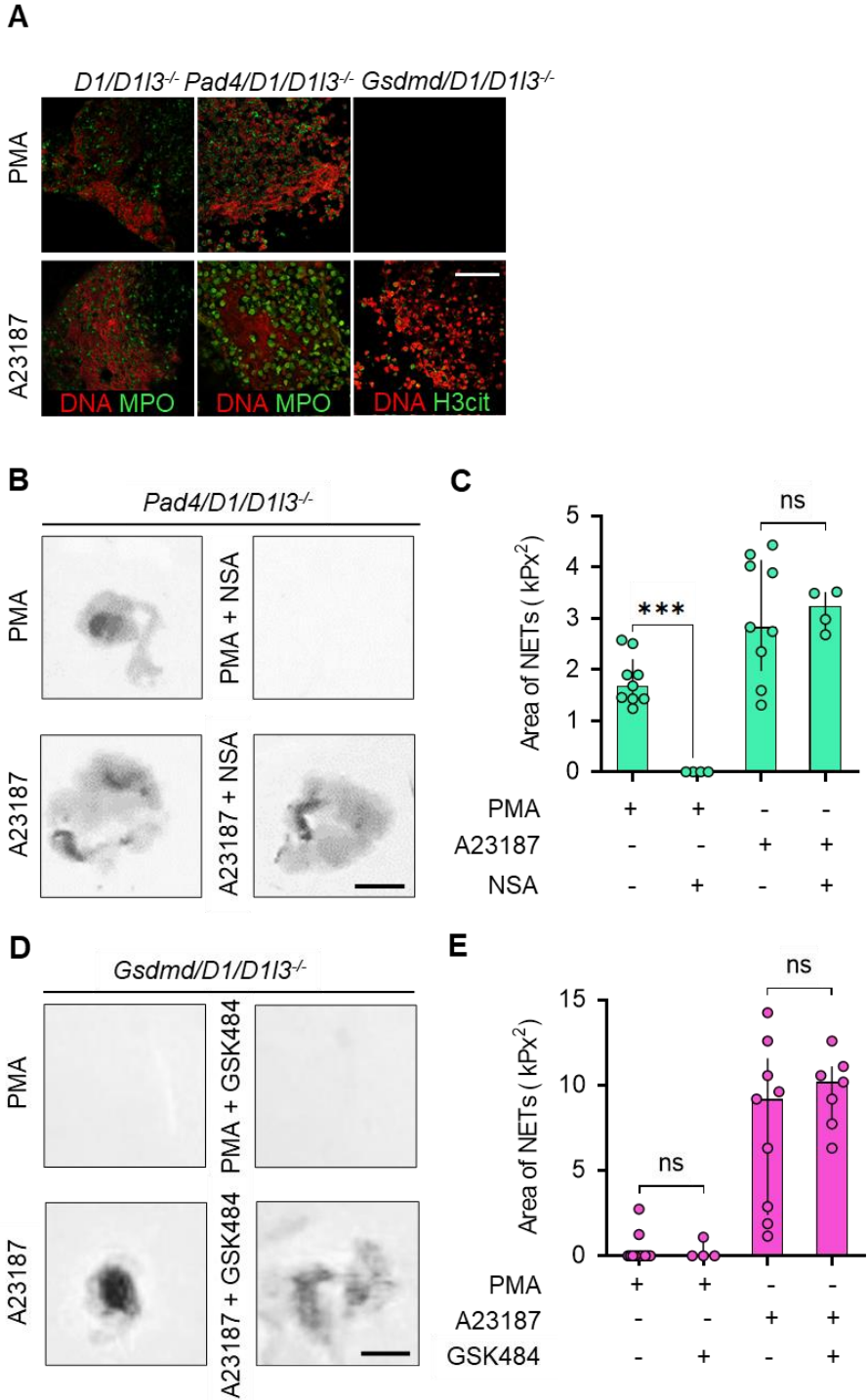
Figure 17. Targeting GSDMD, but not PAD4 interferes with PMA-stimulated NET formation *ex vivo*. Neutrophils were purified from neutrophilic *D1/D1l3⁻/⁻*, *Pad4/D1/D1l3⁻/⁻*, and *Gsdmd/D1/D1l3⁻/⁻* mouse blood, stimulated with PMA (10 nM) or A23187 (25 µM) and analyzed for NET generation at 4 h by immunohistochemistry staining of DNA (red) and MPO or H3cit (green, **A**). Representative images,

n = 5. *Pad4/D1/D1l3*^{-/-} and *Gsdmd/D1/D1l3*^{-/-} mouse-derived neutrophils were pre-treated with the GSDMD inhibitor necrosulfonamide (NSA, 10 µM) or the PAD4 inhibitor GSK484 (5 µM), respectively, parallel to activation with PMA (10 nM) or A23187 (25 µM). Representative images of formed NETs at 4 h were visualized by brightfield microscopy (**B, D**). The surface area covered with NETs was quantified from these microscopic images (**C, E**). Data is represented as median and interquartile range (IQR). (C) Student´s t-test, (E) Mann-Whitney test. * $p < 0.05$, ** $p < 0.01$, *** $p < 0.001$.

4.3 Human DNase1 variants for therapy

4.3.1 Protein engineering of recombinant human DNase1

Efficient removal of NETs from the circulation is a crucial endeavor to protect the host from hyperinflammation, coagulopathy and autoimmune reactions (101). To minimize detrimental effects of circulating NETs, their removal is regulated by two secreted DNases, DNase1 and DNase1L3, which are essential for the degradation of plasma borne nucleic acids (111, 112, 124). However, until today, there are many conditions where an overactive immune system leads to an exuberant accumulation of NETs. Thus, developing novel engineered DNase variants that potently degrade NETs is warranted to better tackle NET-driven thrombo-inflammatory pathologies.

DNase1 preferentially digests naked dsDNA, whereas DNase1L3 favors chromatin as its substrate. The different substrate specificities of DNase1 and DNase1L3 offer the potential to design DNase variants that degrade circulating nucleic acids more efficiently. To exploit the functional differences between DNase1 and DNase1L3, we aimed to generate recombinant human DNase1/DNase1L3 variants that combine key properties of both enzymes.
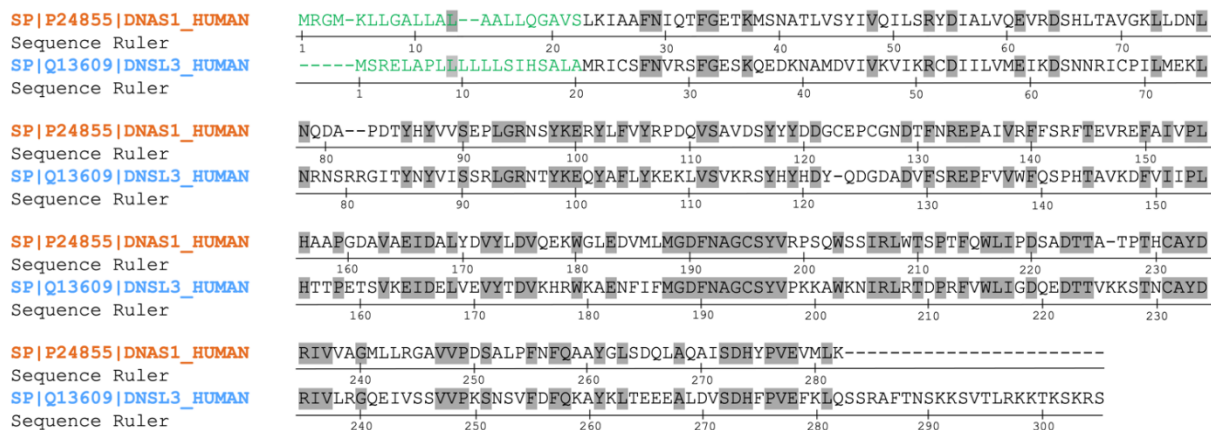
Figure 18. Alignment of human DNase1 and DNase1L3. Protein sequence alignment of human DNase1 (Uniprot sequence ID P24855, orange) and human DNase1L3 (Uniprot sequence ID Q13609, blue), retrieved from the human protein database from Uniprot. The signal peptide is highlighted in green and conserved amino acids are depicted in grey. Figure from (4), in the original paper Supplementary Fig. 1.

Our protein engineering strategy revolved around the systematic exchange of single or multiple adjacent amino acids between two members of the DNase1 family, DNase1 and DNase1L3. Amino acid residue alignment of DNase1 and DNase1L3 amino acid sequences revealed 44% homology between the enzymes (conserved amino acids) (**Fig. 18**). We hypothesized that certain non-conserved amino acids in human DNase1L3 are responsible for the increased chromatin-degrading activity, which are not present in DNase1. Non-conserved amino acid stretches are flanked by a C- and an N-terminal amino acid, termed "N-anchor and C-anchor" here. Here, we transferred non-conserved amino acids between DNase1 (recipient enzyme) and DNase1L3 (donor enzyme) (**Fig. 19**).
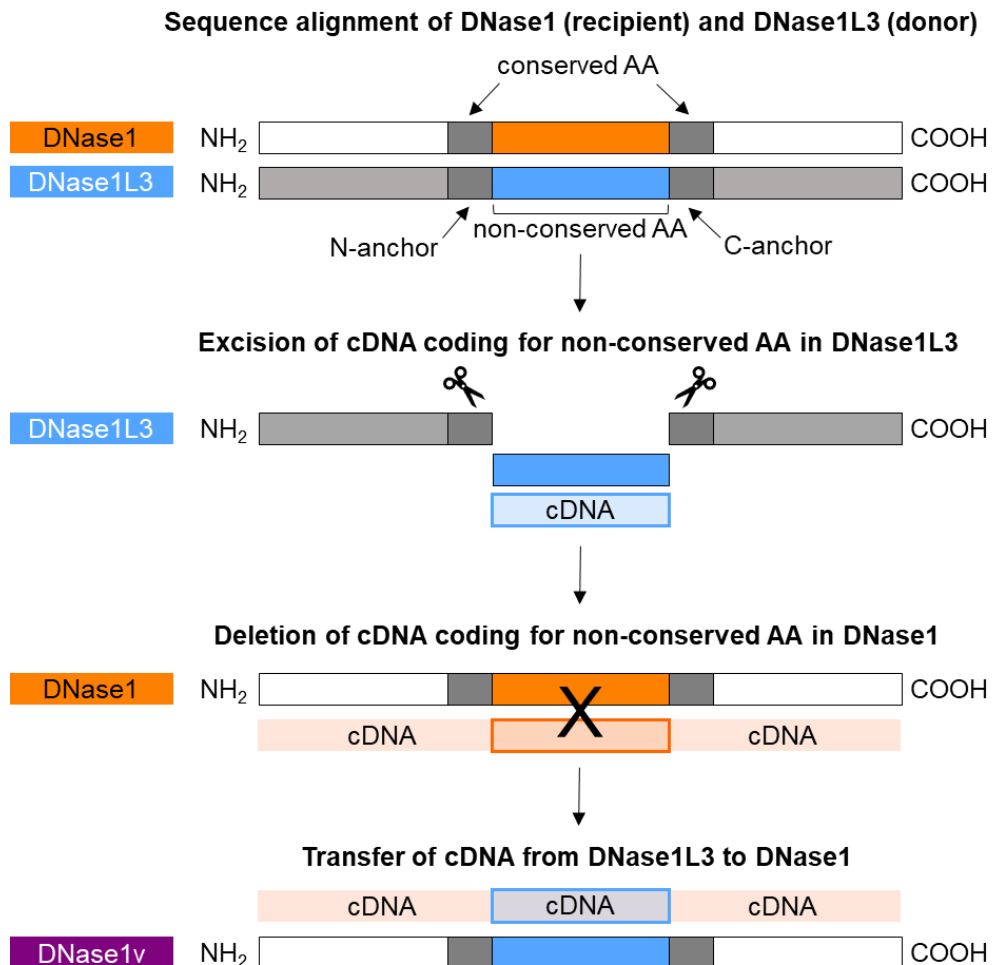
Figure 19. DNase protein engineering gives rise to the design of novel hybrid DNases. Illustration of the employed protein engineering technology. An amino acid (AA) sequence alignment of donor and recipient DNase was performed, and candidate non-conserved AAs were identified for transfer. Complementary DNA (cDNA) encoding for non-conserved AA stretch flanked by conserved AAs (C- and N-anchors) in recipient DNase was replaced with cDNA in donor DNase to generate a library of chimeric recombinant DNases. Adapted figure from (150), in the original patent Fig. 29.

DNase protein engineering consists of several cardinal steps (**Fig. 19**). Firstly, amino acid sequences of the donor and recipient DNase were aligned. We identified non-conserved amino acids suitable for transfer as well as non-conserved regions up- and downstream the transferable region. Next, we excised the complementary DNA (cDNA) encoding for the non-conserved amino acid stretch from the donor enzyme DNase1L3. The respective cDNA sequence was deleted from the recipient enzyme DNase1 and replaced with the donor cDNA from DNase1L3. The cDNA of the chimeric DNase variant (here DNase1v) was synthesized and expressed in recipient model systems deficient in DNase1 and DNase1L3 (e.g., HEK293 cells or *Dnase1/Dnase1l3*$^{-/-}$ mice).

4.3.2 Design of dual-active DNase1 variants

We hypothesized that transfer of specific residues from DNase1L3 into a DNase1 backbone would generate a variant that efficiently degrades both dsDNA and chromatin, leading to efficient clearance of NETs (**Fig. 20A**). To test the substrate specificity of DNase1 and DNase1L3, we generated recombinant proteins and evaluated their activities through (i) dsDNA (isolated from salmon testes) degradation with SRED zymography and (ii) cleavage of chromatin (purified from HEK293 cell nuclei), respectively. The higher the capacity to degrade dsDNA, the larger the diameter of the circle in zymography as determined by densitometric scanning. In samples with lower activity, the loading well appeared as a black dot without a halo (**Fig. 20B**, I and II; upper gels). To assess chromatin degradation, HEK293 cell nuclei were incubated with DNases before DNA isolation and separation by agarose gel electrophoresis. Undigested high-molecular weight DNA shows a distinct band at the top of the gel, whereas degraded low-molecular weight DNA fragments shift downwards, indicating increased chromatin degrading activity.

As expected, recombinant DNase1 effectively cleaved dsDNA in a dose-dependent manner (**Fig. 20B**, I; upper gel). However, DNase1 only had minor activity for degradation of chromatin. Even at the highest amount tested (50 ng), DNase1 only slightly digested the loaded chromatin (**Fig. 20B**, I, lower gel, first lane from the left). Furthermore, chromatin digestion by DNase1 caused an increase in fluorescence of the DNA-intercalating SYBR Safe dye (**Fig. 20B**, I; lower gel; lanes 50 and 5 ng). In contrast, purified DNase1L3 (50 ng) completely degraded chromatin into small fragments, as evidenced by the disappearance of high molecular weight DNA aggregates and the appearance of a typical DNA ladder pattern (**Fig. 20B**, II; lower gel). However, DNase1L3 only showed minimal dsDNA degrading activity (**Fig. 20B**, II; upper gel). Based on zymography and fluorescence data, we found that DNase1 degrades dsDNA approximately 100-fold more efficiently than DNase1L3, while DNase1L3 is approximately 100-fold more potent than DNase1 in degrading chromatin. We also compared the synergistic activities of DNase1 and DNase1L3 in chromatin degradation (**Fig. 20B**, III and IV; lower gels). When co-incubating low amounts of DNase1L3 (5 ng; not sufficient for degrading chromatin completely, **Fig. 20C**, V) with DNase1, chromatin was efficiently digested with ≥ 5 ng purified DNase1 (**Fig. 20C**, IV; lane 1 and 2), indicating a synergistic effect between DNase1 and DNase1L3.

(A)

dsDNA   *chromatin*

I   DNase1 → ++   +

II   DNase1L3 → +   ++

III   DNase1v → +++   +++

(B)

DNase1 [ng]   DNase1L3 [ng]

50   5   0.5   0.05   0.005   50   5   0.5   0.05   0.005

dsDNA — D1 activity

Chromatin — D1L3 activity

Panel: I   II

(C)

DNase1L3 [5 ng]

DNase1 [ng]   DNase1 [ng]

50   5   0.5   0.05   0.005   50   5   0.5   0.05   0.005   0   Buffer

D1 activity

D1L3 activity

Panel: III   IV   V   VI

(D)

Residue	1 10 20 30 40 50 60 70
DNASE1	MRGM-KLLGALLAL--AALLQGAVSLKIAAFNIQTFGETKMSNATLVSYIVQILSRYDIALVQEVRDSHLTAVGKLLDNL
DNASE1[A]	-----MSRELAPLLLLLLSIHSALALKIAAFNIQTFGETKMSNATLVSYIVQILSRYDIALVQEVRDSHLTAVGKLLDNL
DNASE1[B]	MRGM-KLLGALLAL--AALLQGAVSMRICSFNVRSFGESKMSNATLVSYIVQILSRYDIALVQEVRDSHLTAVGKLLDNL
DNASE1[C]	MRGM-KLLGALLAL--AALLQGAVSLKIAAFNIQTFGETKQEDKNAMDVIVQILSRYDIALVQEVRDSHLTAVGKLLDNL
DNASE1[D]	MRGM-KLLGALLAL--AALLQGAVSLKIAAFNIQTFGETKMSNATLVSYIVQILSRYDIALVQEKVIKRCDIILVMEVRDSHLTAVGKLLDNL
DNASE1[E]	MRGM-KLLGALLAL--AALLQGAVSLKIAAFNIQTFGETKMSNATLVSYIVQILSRYDIALVQEIKDSNNRICPILMEKL

Residue	80 90 100 110 120 130 140 150
DNASE1	NQDA--PDTYHYVVSEPLGRNSYKERYLFVYRPDQVSAVDSYYYDDGCEPCGNDTFNREPAIVRFFSRFTEVREFAIVPL
DNASE1[F]	NRNSRRGITYHYVVSEPLGRNSYKERYLFVYRPDQVSAVDSYYYDDGCEPCGNDTFNREPAIVRFFSRFTEVREFAIVPL
DNASE1[G]	NQDA--PDTYNYVISSRLGRNSYKERYLFVYRPDQVSAVDSYYYDDGCEPCGNDTFNREPAIVRFFSRFTEVREFAIVPL
DNASE1[H]	NQDA--PDTYHYVVSEPLGRNTYKEQYAFLYRPDQVSAVDSYYYDDGCEPCGNDTFNREPAIVRFFSRFTEVREFAIVPL
DNASE1[I]	NQDA--PDTYHYVVSEPLGRNSYKERYLFVYKEKLVSVKRSYHYHDGCEPCGNDTFNREPAIVRFFSRFTEVREFAIVPL
DNASE1[J]	NQDA--PDTYHYVVSEPLGRNSYKERYLFVYRPDQVSAVDSYYYDDY-QDGDADVFSREPAIVRFFSRFTEVREFAIVPL
DNASE1[K]	NQDA--PDTYHYVVSEPLGRNSYKERYLFVYRPDQVSAVDSYYYDDGCEPCGNDTFNREPFVVRFFSRFTEVREFAIVPL
DNASE1[L]	NQDA--PDTYHYVVSEPLGRNSYKERYLFVYRPDQVSAVDSYYYDDGCEPCGNDTFNREPAIWFQSPHTAVKDFVIIPL

Residue	160 170 180 190 200 210 220 230
DNASE1	HAAPGDAVAEIDALYDVYLDVQEKWGLEDVMLMGDFNAGCSYVRPSQWSSIRLWTSPTFQWLIPDSADTTA-TPTHCAYD
DNASE1[L] cont.	HTTPETSVKEIDALYDVYLDVQEKWGLEDVMLMGDFNAGCSYVRPSQWSSIRLWTSPTFQWLIPDSADTTA-TPTHCAYD
DNASE1[M]	HAAPGDAVAEIDELVEVYTDVQEKWGLEDVMLMGDFNAGCSYVRPSQWSSIRLWTSPTFQWLIPDSADTTA-TPTHCAYD
DNASE1[N]	HAAPGDAVAEIDALYDVYLDVKHRWKAENFIFMGDFNAGCSYVRPSQWSSIRLWTSPTFQWLIPDSADTTA-TPTHCAYD
DNASE1[O]	HAAPGDAVAEIDALYDVYLDVQEKWGLEDVMLMGDFNAGCSYVPKKAWKNIRLRTDPTFQWLIPDSADTTA-TPTHCAYD
DNASE1[P]	HAAPGDAVAEIDALYDVYLDVQEKWGLEDVMLMGDFNAGCSYVRPSQWSSIRLWTSPRFVWLIGDQEDTTA-TPTHCAYD
DNASE1[Q]	HAAPGDAVAEIDALYDVYLDVQEKWGLEDVMLMGDFNAGCSYVRPSQWSSIRLWTSPTFQWLIPDSADTTVKKSTHCAYD
DNASE1[R]	HAAPGDAVAEIDALYDVYLDVQEKWGLEDVMLMGDFNAGCSYVRPSQWSSIRLWTSPTFQWLIPDSADTTA-TPTNCAYD

Residue	240 250 260 270 280 290 300
DNASE1	RIVVAGMLLRGAVVPDSALPFNFQAAYGLSDQLAQAISDHYPVEVMLK---------------------
DNASE1[R] cont.	RIVLRGQEIVSSVVPKSNSVFNFQAAYGLSDQLAQAISDHYPVEVMLK---------------------
DNASE1[S]	RIVVAGMLLRGAVVPDSALPFDFQKAYKLTEEEALDVSDHYPVEVMLK---------------------
DNASE1[T]	RIVVAGMLLRGAVVPDSALPFNFQAAYGLSDQLAQAISDHFPVEFKLQSSRAFTNSKKSVTLRKKTKSKRS

Figure 20. Strategy for engineering dual-active DNase1/DNase1L3 mutants. (A) Scheme for the generation of dual-active DNase mutants based on the addition of DNase1L3 activity to DNase1.

DNase1 (I, orange) and DNase1L3 (II, blue) differ in their substrate specificities: DNase1 degrades dsDNA more efficiently than chromatin, and *vice versa* chromatin is the preferred substrate for DNase1L3 as compared to dsDNA. The designed dual-active DNase1 variant (DNase1v, III, purple) contains sequences of DNase1 and DNase1L3 and efficiently digests both dsDNA, and chromatin. **(B)** Purified recombinant DNase1 (*panel I*) and DNase1L3 (*panel II*; 50 - 0.005 ng) were either incubated with dsDNA or chromatin isolated from salmon testes or from HEK293 cell nuclei, respectively. Diameters of the dark circles in zymography SRED assays present dsDNA degrading DNase1 activity (upper gel; dsDNA/D1activity). Agarose gel electrophoresis of digested chromatin shows chromatin degrading activity of DNase1L3. High-molecular weight chromatin complexes are cleaved into smaller fragments (lower gel; chromatin/D1L3 activity). **(C)** Co-incubation of DNase1L3 and DNase1shows synergistic DNases activities. dsDNA and chromatin were incubated with increasing levels of DNase1 alone (*panel III*) or together with DNase1L3 (5 ng, *panel IV*), that alone (*panel V*) was not sufficient to degrade chromatin completely. *Panel VI* shows buffer treated dsDNA and chromatin. **(D)** Amino acid sequences of DNase1 and mutated regions of the 20 engineered DNase1 variants (DNase1[A] – DNase1[T], which are detailed in Table 3). Numbering relates to the native DNase1 sequence. Residues conserved between DNase1 and DNase1L3 are depicted in grey and the signal sequence of DNase1 is highlighted in green. Non-conserved residues are highlighted in orange in the DNase1 backbone. DNase1L3 sequence stretches that were swapped into the DNase1 backbone are shown in blue. "cont." indicates that DNase1[L] and DNase1[R] sequences continue from the lines above. D1 – DNase1, D1L3 – DNase1L3. Figure from (4), in the original paper Fig. 1.

We systematically exchanged stretches of non-conserved amino acids in DNase1 with amino acid residues of DNase1L3. Amino acid sequences that were conserved among both DNases were not altered. Sequences of the 20 generated DNase1 variants (DNase1[A] – DNase1[T]) are shown in **Fig. 20D**. Substituted non-conserved residues of DNase1 and DNase1L3 are shown in **Table 3**, e.g., in DNase1[H] variant sites 15 ($N^{96}S^{97}$), 16 (R^{101}), 17 (L^{103}), and 18 (V^{105}) in DNase1 were substituted with corresponding residues 15´ ($N^{96}T^{97}$), 16´ (Q^{101}), 17´ (A^{103}), and 18´ (L^{105}) of DNase1L3.

Table 3. Insertion of non-conserved DNase1L3 amino acids into DNase1 yielded 20 novel enzymatic variants. Non-conserved amino acid stretches of human DNase1 and DNase1L3 flanked by conserved amino acids of the respective enzyme (N- and C-terminal anchors) are listed. Mutations that transfer sequences from DNase1L3 to DNase1 are shown and categorized into 20 different variants (first column from the right; variants A – T). CA = C-terminal anchor; NA = N-terminal anchor. Table from (4), in the original paper Supplementary Table 1.

AA stret-ches	N-terminal anchor (NA) in DNase1	C-terminal anchor (CA) in DNase1	Non-conserved AA DNase1	Non-conserved AA DNase1L3	DNase1 variants
0	N/A	N/A	1-22 (MRGMKLLGALLALAALL QGAVS)	1-20 (MSRELAPLLLLLLSI HSALA)	A
1	SP	F28/N29	23-27 (LKIAA)	21-25 (MRICS)	
2	F28/N29	F33/G34	30-32 (IQT)	28-30 (VRS)	B
3	F33/G34	K37	35-36 (ET)	33-34 (ES)	
4	K37	V48	38-47 (MSNATLVSYI)	36-45 (QEDKNAMDVI)	C
5	V48	R53	49-52 (QILS)	47-50 (KVIK)	
6	R53	D55	54 (Y)	52 (C)	D
7	D55	E61	56-60 (IALVQ)	54-58 (IILVM)	
8	E61	D64	62-63 (VR)	60-61 (IK)	
9	D64	L73	65-72 (SHLTAVGK)	63-70 (SNNRICPI)	E
10	L73	L77/N78	74-76 (LDN)	72-74 (MEK)	
11	L77/N78	Y85	79-84 (QDAPDY)	77-84 (RNSRRGIT)	F
12	Y85	Y87	86 (H)	86 (N)	
13	Y87	S90	88-89 (VV)	88-89 (VI)	G
14	S90	L93/G94/R95	91-92 (EP)	91-92 (SR)	
15	L93/G94/R95	Y98/K99/E100	96-97 (NS)	96-97 (NT)	
16	Y98/K99/E100	Y102	101 (R)	101 (Q)	
17	Y102	F104	103 (L)	103 (A)	H
18	F104	Y106	105 (V)	105 (L)	
19	Y106	Y111/S112	107-110 (RPDQ)	107-110 (KEKL)	
20	Y111/S112	Y117	113-116 (AVDS)	113-116 (VKRS)	
21	Y117	Y119	118 (Y)	118 (H)	I
22	Y119	D121	120 (D)	120 (H)	
23	D121	D129	122-128 (GCEPCGN)	122-127 (YQDGDA)	
24	D129	F131	130 (T)	129 (V)	J
25	F131	R133/E134/P135	132 (N)	131 (S)	
26	R133/E134/P135	V138	136-137 (AI)	135-136 (FV)	K
27	V138	F140	139 (R)	138 (W)	
28	F140	T145	141-144 (FSRF)	140-143 (QSPH)	
29	T145	F150	146-149 (EVRE)	145-148 (AVKD)	
30	F150	I152	151 (A)	150 (V)	
31	I152	P154/L155/H156	153 (V)	152 (I)	L
32	P154/L155/H156	P159	157-158 (AA)	156-157 (TT)	
33	P159	V163	160-162 (GDA)	159-161 (ETS)	
34	V163	E165/I166/D167	164 (A)	163 (K)	
35	E165/I166/D167	L169	168 (A)	167 (E)	
36	L169	V172/Y173	170-171 (YD)	169-170 (VE)	M
37	V172/Y173	D175/V176	174 (L)	173 (T)	

38	D175/V176	W180	177-179 (QEK)	176-178 (KHR)	
39	W180	E183	181-182 (GL)	180-181 (KA)	
40	E183	M187-GDFNAGCSY-V198	184-187 (DVML)	183-187 (NFIF)	N
41	M187-GDFNAGCSY-V198	W203	199-202 (RPSQ)	198-201 (PKKA)	
42	W203	I206/R207/L208	204-205 (SS)	203-204 (KN)	O
43	I206/R207/L208	T210	209 (W)	208 (R)	
44	T210	P212	211 (S)	210 (D)	
45	P212	F214	213 (T)	212 (R)	
46	F214	W216/L217/I218	215 (Q)	214 (V)	
47	W216/L217/I218	D220	219 (P)	218 (G)	P
48	D220	D223/T224/T225	221-222 (SA)	220-221 (QE)	
49	D223/T224/T225	T229	226-228 (ATP)	225-228 (VKKS)	Q
50	T229	C231-AYDRI-V237	230 (H)	230 (N)	
51	C231-AYDRI-V237	G240	238-239 (VA)	238-239 (LR)	
52	G240	V247/V248/P249	241-246 (MLLRGA)	241-246 (QEIVSS)	R
53	V247/V248/P249	S251	250 (D)	250 (K)	
54	S251	F255	252-254 (ALP)	252-254 (NSV)	
55	F255	F257/Q258	256 (N)	256 (D)	
56	F257/Q258	Y261	259-260 (AA)	259-260 (KA)	
57	Y261	L263	262 (G)	262 (K)	S
58	L263	A268	264-267 (SDQL)	264-267 (TEEE)	
59	A268	S272/D273/H274	269-271 (QAI)	269-271 (LDV)	
60	S272/D273/H274	P276/V277/E278	275 (Y)	275 (F)	
61	P276/V277/E278	L281	279-280 (VM)	279-280 (FK)	
62	L281	-	282 (K)	282-305 (QSSRAFTNSKKSVTLRKKTKSKRS)	T

4.3.3 Screening of dual-active DNase1 variants

All DNase1 variants were expressed in HEK293 cells via a mammalian cell transfection protocol. We aimed to identify enzymatic variants of DNase1 that exhibit a dual degradation activity for dsDNA and chromatin. Cell supernatants were systematically screened for their DNase1 and DNase1L3 activity using SRED zymography (**Fig. 21A**, upper gel) and chromatin degradation (**Fig. 21A**, lower gel). DNase1 activities of variants DNase1[A] (101%), DNase1[G] (105%), DNase1[J] (103%), DNase1[K] (114%), DNase1[N] (102%), DNase1[O] (113%), DNase1[Q] (104%) and DNase1[R] (102%) exceeded native DNase1 levels (set to 100%; **Fig. 21B**). DNase1 activities of DNase1[D], DNase1[H], DNase1[I], DNase1[L], and DNase1[T] were decreased compared to native DNase1, implicating that amino acid mutations in these regions reduced DNase1 activity of these variants (**Fig. 21B**). The diminished DNase1 activity may be a result

of reduced binding to the substrate or a decrease in stability in the secondary structure of the protein. Next, we analyzed the variants for their DNase1L3 activity and found that DNase1^E (118%), DNase1^K (119%), and DNase1^O (111%) showed increased chromatin-digesting activities over native DNase1L3 (100%; **Fig. 21C**). Variants with the highest cumulative DNase1 and DNase1L3 activities were chosen for subsequent testing. Of these, DNase1^G (191%), DNase1^K (233%), and DNase1^O (224%) mutants demonstrated a significant enhancement in combined DNase1 and DNase1L3 activities compared to the total levels of the native DNases (**Fig. 21D**).
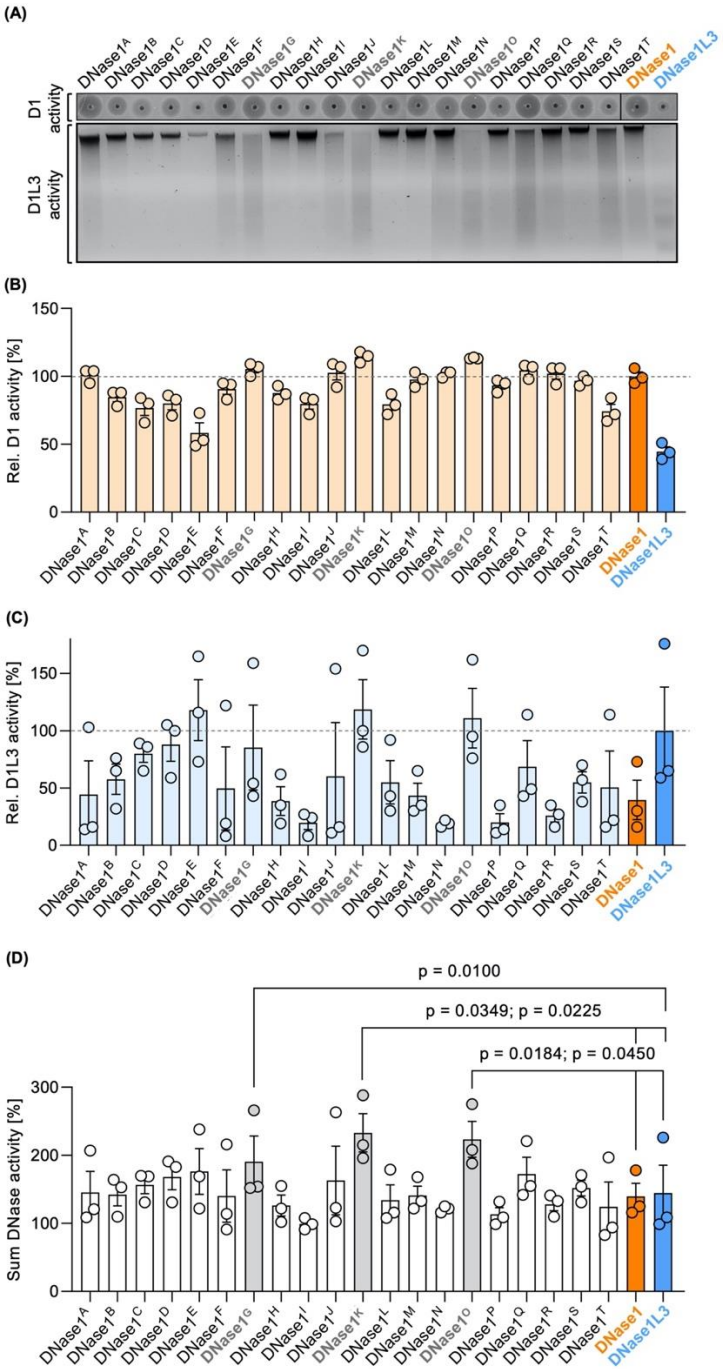
Figure 21. Screening of dual-active DNase1 variants for DNase1 and DNase1L3 activity. (A) dsDNA (upper gel; D1 activity) or chromatin (lower gel; D1L3 activity) was incubated with supernatants of HEK293 cell-derived DNase1 variants, native DNase1 or DNase1L3. DNase1 and DNase1L3 activities of the various DNases were analyzed as in Fig. 20B above. **(B)** Quantification of densitometric scans of the digested dsDNA as a measure for DNase1 activity. Enzymatic activity is given relative to DNase1 (D1) levels set to 100%. **(C)** Residual chromatin signals as a measure for DNase1L3 activity is blotted relative to DNase1L3 (D1L3) activity (100%). **(D)** Sum of DNase1 and DNase1L3 activities derived from C and D. *p*-value by paired one-way ANOVA with Dunnett's multiple comparisons test. Data are mean ± standard error of the mean (SEM), n = 3. D1 – DNase1, D1L3 – DNase1L3. Figure from (4), in the original paper Fig. 2.

4.3.4 Characterization of dual-active variant DNase1^{G,K,O}

Next, we analyzed the synergistic effects of the three mutated variants for their DNase1 and DNase1L3 activities. We substituted 15 amino acid residues from DNase1 with residues from DNase1L3: G (H^{86} by N^{86}; V^{88}V^{89} by V^{88}I^{89} and E^{91}P^{92} by S^{91}R^{92}), K (A^{136}I^{137} by F^{135}V^{136}), and O (R^{199}P^{200}S^{201}Q^{202} by P^{198}K^{199}K^{200}A^{201}; S^{204}S^{205} by K^{203}N^{204} and W^{209} by R^{208}; S^{211} by D^{210}), generating one novel variant DNase1^{G,K,O} (**Fig. 22A**; original DNase1 backbone is in orange and the DNase1L3 sequence in blue). SRED zymography and chromatin degradation assays showed that DNase1^{G,K,O} dose-dependently degraded both dsDNA and chromatin (**Fig. 22B**). DNase1^{G,K,O} exhibited a significantly increased DNase1 activity compared to native DNase1 (116 *vs.* 100%, *p* = 0.0360). DNase1^{G,K,O} also showed a trend towards superior degradation compared to the individual variants DNase1^{G}, DNase1^{K} and DNase1^{O} that each carry mutations in an individual amino acid stretch (**Fig. 22C** upper gel and **22D**; 100%, 113% and 103%). Even though the novel variant only comprises 15 residues of the original DNase1L3 sequence, DNase1^{G,K,O} demonstrated a trend towards higher DNase1L3 activity compared to the native enzyme and variants with individual substitutions (**Fig. 22C** lower gel and **22E**; 110 *vs.* DNase1L3 100%, DNase1^{G} 80%, DNase1^{K} 101% and DNase1^{O} 83%). Particularly, DNase1^{G,K,O} variant displayed significantly higher levels of combined DNase1 and DNase1L3 activities compared to native DNase1 and DNase1L3 (**Fig. 22F**; 225 *vs.* 135% and 165%, *p* = 0.0322 and *p* = 0.0196). Next, we tested the dual-active variant DNase1^{G,K,O} for its stability and activity *in vivo*.
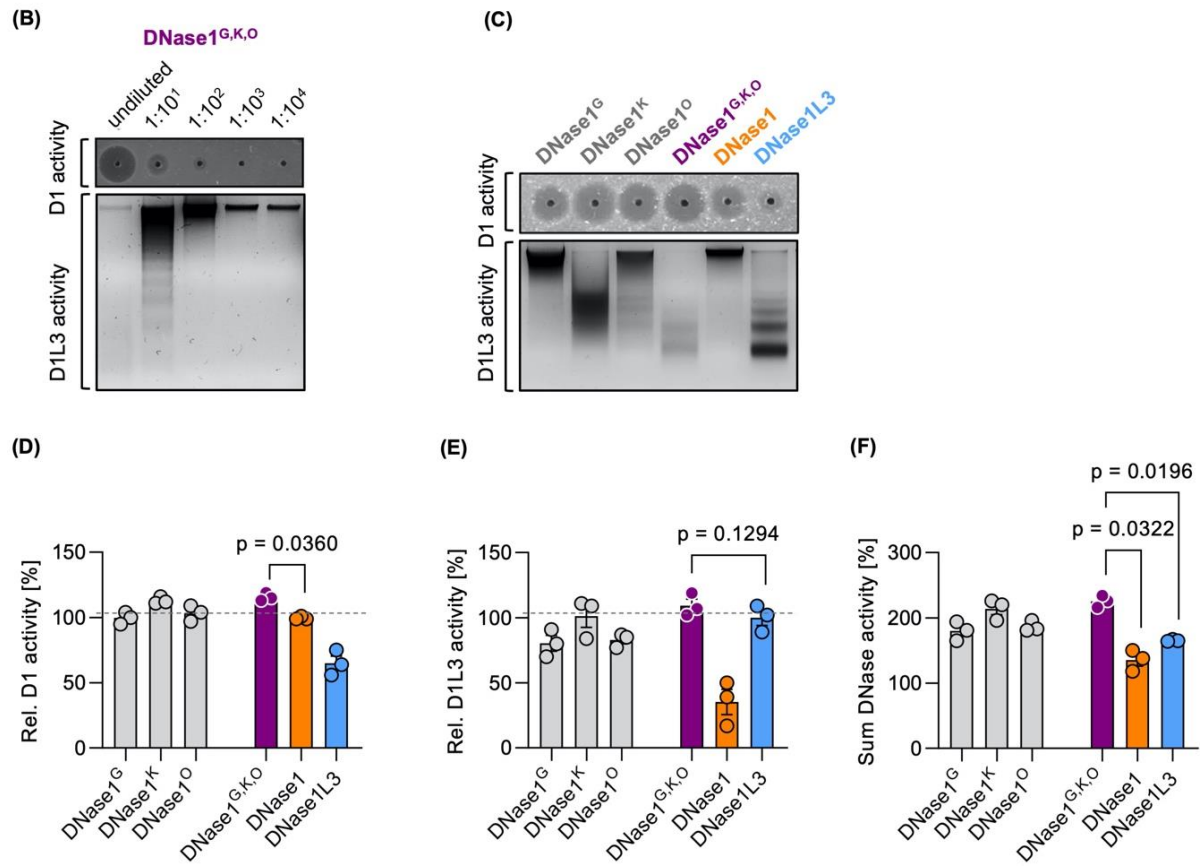
Figure 22. Characterization of dual-active variant DNase1^G,K,O. (**A**) Amino acid sequence of the dual-active variant DNase1^G,K,O that combines the identified DNase1L3-derived mutations of DNase1^G (five residues; positions 86, 88-89, 91-92), DNase1^K (two residues; positions 136-137) and DNase1^O (eight residues; positions 199-202, 204-205, 209, 211). Signal peptide sequence is shown in green. Non-mutated DNase1 sequence is in orange and swapped DNase1L3 derived residues in blue. (**B**) Dose dependency of dsDNA (upper gel; D1 activity) and chromatin (lower gel; D1L3 activity) degrading activity of DNase1^G,K,O. Serial 1:10 dilution of supernatants of transfected HEK293 cells were tested. (**C**) dsDNA (upper gel; D1 activity) and chromatin (lower gel; D1L3 activity) degrading activity of recombinant DNase1^G, DNase1^K, DNase1^O, DNase1^G,K,O variants, DNase1, and DNase1L3. (**D**) Quantification of DNase1, (**E**) DNase1L3 (**E**), and (**F**) combined DNases activities of various DNases from densitometric scans as in (C). Data is given relative to native enzyme activity (100%) in (D) and (E). *p*-value by paired one-way ANOVA with Dunnett's multiple comparisons test. Columns represent mean ± SEM, n = 3. D1 – DNase1, D1L3 – DNase1L3. Figure from (4), in the original paper Fig. 3.

4.3.5 Dual-active DNase1^{G,K,O} variant is stable and functional in serum and bile but not in urine of transgenic mice

After establishing DNase1^{G,K,O} *in vitro*, we transgenically expressed the variant in hepatocytes of *Dnase1/Dnase1l3$^{-/-}$* mice which lack endogenous DNases (92). The aim of our strategy was to evaluate DNase1^{G,K,O} as an *in vivo* tool for targeting NETs. DNase1^{G,K,O}, DNase1, and DNase1L3 were expressed in *Dnase1/Dnase1l3$^{-/-}$* mice using hydrodynamic tail vein injections. After 7 days, the mice were sacrificed, and serum, bile, and urine of the three transgenic mouse lines were collected and analyzed for their dsDNA and chromatin degradation activities. In *Dnase1/Dnase1l3$^{-/-}$* mice, DNase activity was absent (92). Sera from DNase1^{G,K,O} transgenic mice degraded dsDNA and chromatin in a dose-dependent manner (**Fig. 23A**). While DNase1 and DNase1L3 activities were also detected in bile, however at lower levels, no activity was found in urine of DNase1^{G,K,O} transgenic mice (**Fig 23B, C**). DNase1 activity was equivalent in serum and slightly higher in bile in DNase1^{G,K,O} transgenic mice compared to DNase1 expressing mice (100%, **Fig. 23D**). Furthermore, DNase1L3 activity of serum and bile of animals expressing DNase1^{G,K,O} was significantly elevated over DNase1L3 transgenic mice (100%; serum $p < 0.0001$, bile $p = 0.0094$, **Fig. 23E**). DNase1^{G,K,O} transgenic mouse sera surpassed DNase1 activity levels of WT mice by approximately 100-fold, while the DNase1L3 activity was largely increased in WT mouse sera as compared to DNase1^{G,K,O} transgenic mice. In undiluted serum of WT mice (n = 5), DNase1 activity was slightly higher as compared to 100-fold diluted DNase1^{G,K,O} transgenic mouse serum. DNase1L3 activity of DNase1^{G,K,O} transgenic mouse serum was lower compared to undiluted WT serum (n = 2) that completely degraded within 30 min by the applied chromatin (data not shown). Combined DNase1 and DNase1L3 activities in the sera and bile of DNase1^{G,K,O} expressing animals significantly exceeded the levels of each native enzyme DNase1 and DNase1L3, respectively (**Fig. 23F**; 540 *vs.* 228% and 135% in serum, $p < 0.0001$ each; 329 *vs.* 216% and 150% in bile, $p = 0.0255$, $p = 0.0045$, respectively). The data obtained from *in vivo* experiments provides evidence that the dual-active variant DNase1^{G,K,O} is secreted into body fluids and is both stable and functional in serum and bile.
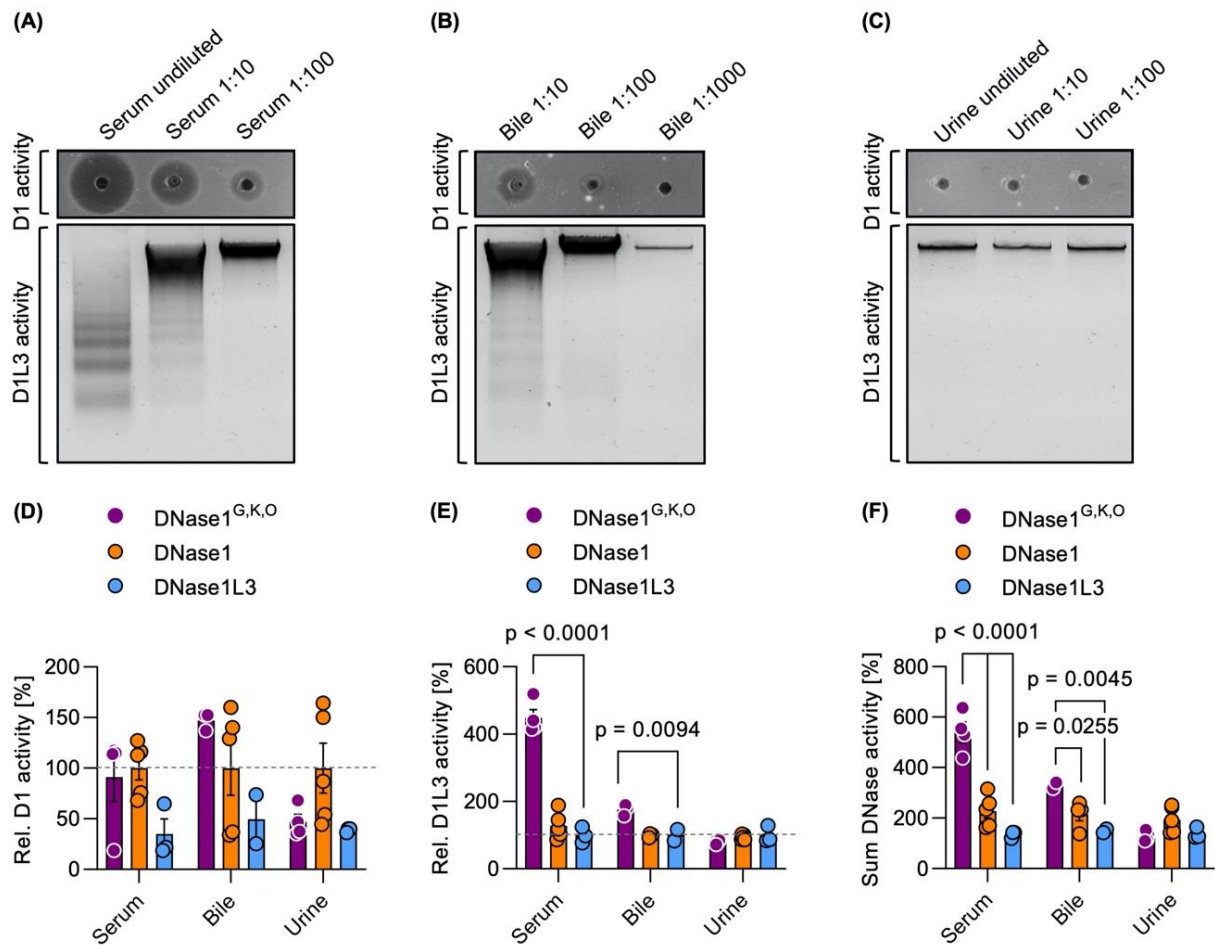
Figure 23. DNase activities in serum, bile, and urine of DNase1^{G,K,O} transgenic mice. We produced mouse lines with transgenic expression of DNase1^{G,K,O}, DNase1 and DNase1L3 in hepatocytes on a *Dnase1/Dnase1l3$^{-/-}$* deficient background. DNase1 (upper gel; D1 activity) and DNase1L3 (lower gel; D1L3 activity) activities in serum (**A**), bile (**B**), and urine (**C**) of DNase1^{G,K,O} transgenic mice were measured by dsDNA and chromatin degradation, respectively. Representative gels of a series of n = 3. DNase1 (**D**), DNase1L3 (**E**) and summarized DNase1 and DNase1L3 (**F**) activities in serum, bile, and urine of DNase1^{G,K,O} (purple) DNase1 (orange) and DNase1L3 (blue) transgenic mice. Activities are normalized to native DNase levels (100%). Data represent mean ± SEM, *p*-value by two-way ANOVA with Dunnett's multiple comparisons test. Each data point represents an individual animal, DNase1^{G,K,O} (n = 4), DNase1 (n = 5), DNase1L3 (n = 3). D1 – DNase1, D1L3 – DNase1L3. Figure from (4), in the original paper Fig. 4.

4.3.6 DNase1^{G,K,O} is superior to DNase1 and DNase1L3 in degrading human NETs
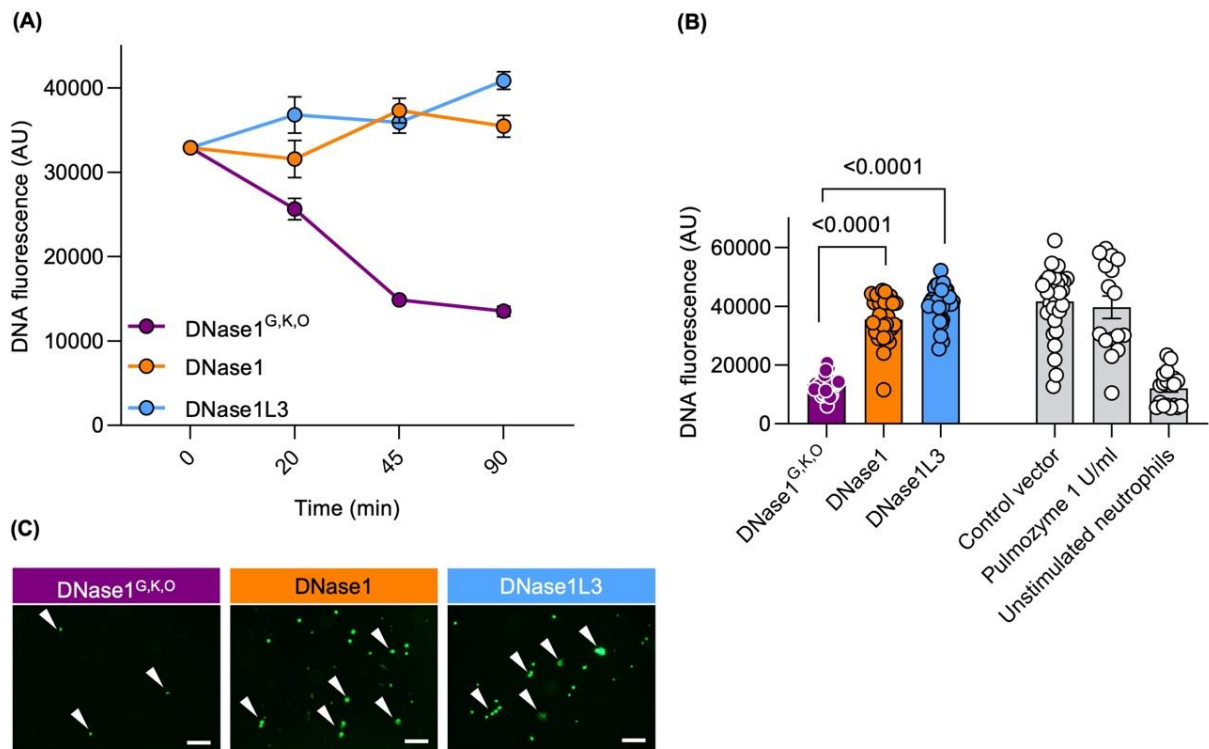
Figure 24. Dual-active DNase1^{G,K,O} efficiently degrades NETs. Human neutrophils were PMA-stimulated to produce NETs. Formed NETs were treated with supernatants of DNase1^{G,K,O}, DNase1, DNase1L3, or of mock vector transfected HEK293 cells. (**A**) Kinetics of DNase1^{G,K,O}, DNase1 and DNase1L3-mediated NET degradation. Data represent mean ± SEM. (**B**) Residual NET fibers upon DNase1^{G,K,O}, DNase1, DNase1L3 incubation (n = 32, each) were quantified by Sytox Green fluorescence at 90 min. Recombinant human DNase1 (1 U/ml, Pulmozyme; n = 16) and baseline fluorescence of unstimulated neutrophils (n = 20) served as controls. Data represent mean ± SEM, *p*-value, Kruskal-Wallis with Dunn's multiple comparisons test. (**C**) Representative fluorescence images of NETs after 90 min DNase treatment. White arrowheads indicate undigested NET remnants. A representative image of n = 3 is shown. Scale bar 100 µm. Figure from (4), in the original paper Fig. 5.

Next, we evaluated the capability of DNase1^{G,K,O} to degrade *ex vivo* generated NETs. Healthy human neutrophils were isolated and activated with 100 nM PMA for 4 h to induce NET formation (151). Formed NETs were digested with supernatants from HEK293 cell-produced DNase1, DNase1L3, or DNase1^{G,K,O}. Supernatants of mock vector transfected cells served as controls. DNase1^{G,K,O} digested NETs in a time-dependent manner, while DNase1 and DNase1L3 were inactive (13,522 mean fluorescence in AU *vs.* 35,465 AU and 40,882 AU at 90 min; *p* < 0.0001 each, **Fig. 24A**). Fluorescence NET signal was lowest after 90 min incubation with DNase cell

supernatants; and this time point was therefore used for further experiments. DNase1[G,K,O] degraded *ex vivo* formed NETs, indicated by changes in the fluorescence of intact DNA fibers (**Fig. 24B**). DNase1[G,K,O] activity abolished the DNA fluorescence signal to levels seen in unstimulated neutrophils (12,078 AU). DNase1 and DNase1L3 cell supernatants showed lower degradation activities compared to DNase1[G,K,O]. In addition, commercially available DNase1 (1 U/ml, Pulmozyme) was inferior to DNase1[G,K,O] in degrading NETs (39,664 AU vs. 13,522 AU; $p < 0.0001$). Representative nucleic acid staining confirmed that the NET-degrading potency of DNase1[G,K,O] exceeded that of DNase1 and DNase1L3 (**Fig. 24C**).

5. Discussion

5.1 NETs in thrombo-inflammation

Polyanions are negatively charged molecules and occur in various forms in nature. Polyanions can exert both pro- or anticoagulant activities. NETs are procoagulant polyanions and serve as a matrix for the accumulation of coagulation factors (65, 70) and platelets (67); promotion of fibrin deposition (67) and local proteolysis of the coagulation suppressor TFPI (69). NETs accumulate in thrombi excised after myocardial infarction, stroke, and peripheral vascular occlusions (152-155). NETs enhanced thrombin generation in platelet-poor plasma via the intrinsic pathway of coagulation. This effect was diminished in FXII- and FXI-deficient plasma (156). In addition to activating FXII, NETs stimulate the extrinsic coagulation pathway by exposing TF on their surface and the digestion of TFPI through the granule proteases NE and cathepsin G (69, 157). The fibrous NET meshwork also aids in the mechanical stabilization of thrombi by hampering the tissue plasminogen activator-driven conversion of plasminogen to plasmin. NETs also form a composite network with fibrin and bind and delay release of fibrinolytic peptides (158, 159). Taken together, a balance between NET formation and degradation is of crucial importance, making them interesting biomarker candidates for a range of thrombotic, inflammatory, and autoimmune pathologies.

We found that NETs trigger FXII-driven coagulation, contributing to the hyperinflammation in severe COVID-19 infections (**Figs. 7b,** and **8d**) (160-162). Furthermore, we discovered activated neutrophils and abundant NET release in serum and thrombi of VITT-associated CVST patients (**Figs. 11,** and **12**). Glucose oxide- or IL-8-stimulated NETs can activate FXII *in vitro* (70). Scanning electron microscopy images of the DNA backbone of NETs formed by platelet-activated neutrophils served as contact activating surface for FXII (65). Contrastingly, Noubouossie and colleagues concluded that assembled NETs, unlike DNA or the individual histone proteins H3 and H4, did not initiate or amplify coagulation *in vitro* (71). They propose that nucleosome units and higher-order supercoiled chromatin have an overall neutral charge because bound (cationic) histones neutralize the negative charge of the DNA. When studying postmortem lung tissue from COVID-19 patients, we detected an increase of FXIIa in

plasma and lung tissue from COVID-19 patients, but not in patients with other pulmonary complications (**Fig. 5**). Areas of colocalization of NETs and FXIIa were detected in lung parenchyma, within the pulmonary vasculature and in fibrin-rich alveolar spaces of COVID-19 lungs, suggesting that NETs act as contact-activating scaffold in COVID-19 lungs (**Fig. 7d**). Whether the negatively charged DNA from NETs directly binds and activates FXII, or if the entire NET structure serves as a contact activation scaffold for FXII (163) remains to be explored.

5.2 The NETs-FXII axis in COVID-19

In this study, we found that NETs and FXIIa are involved in COVID-19-associated thrombo-inflammation. Common COVID-19 complications include ARDS, arrhythmia, acute cardiac injury, heart failure, and acute kidney injury (164). The most prevalent thrombotic complications in COVID-19 patients include DVT with PE and alveolar-capillary microthrombi, in line with our cohort (**Fig. 2a**) (165, 166). These thrombo-embolic events occur frequently in severe COVID-19 cases, despite anticoagulation therapy (167-169). Even after hospital discharge, some individuals might develop thrombosis in the later stages of the disease (170), illustrating the importance of thromboprophylaxis and anticoagulation therapy. The largest study on anticoagulation therapy in COVID-19 reported to date was a multiplatform investigation based on three adaptive randomized trials (ATTACC, ACTIV-4a, and REMAP-CAP). The study investigated the use of therapeutic anticoagulation with heparin vs usual care pharmacologic thromboprophylaxis in critically ill ICU-supported (1,098 patients) and not critically ill COVID-19 patients (2,219 patients) (171, 172). Therapeutic-dose anticoagulation with heparin (dosed according to local hospital policy, practice, and guidelines for treatment of venous thromboembolism) did not improve the primary outcome of survival free of cardiovascular or respiratory organ support in critically ill patients. The bleeding tendency was increased with therapeutic- compared to prophylactic-dose heparin. Contrastingly, moderately ill patients were more likely to achieve a high number of organ support-free days with therapeutic- compared to prophylactic-dose heparin (171, 172). Thus, efficient anticoagulation that spares hemostasis is still warranted and could include pharmacologic targeting of NETs.

COVID-19 is accompanied by procoagulant and inflammatory phenotypes with acute phase reaction, including endotheliitis, endothelial damage, hyperfibrinogenemia, and procoagulant platelets (165, 173-175). Our proteomic analyses of lung tissue revealed enrichment of pathways associated with angiogenesis, which correlates with a study showing that intussusceptive angiogenesis was higher in COVID-19 lungs compared to influenza-infected lungs (**Fig. 3b**) (165). Furthermore, complement system proteins were found to be upregulated in COVID-19 vs control lungs, in line with previously published reports (**Fig. 3b**) (176, 177). We also found pathways related to neutrophil degranulation and activation, as well as platelet degranulation, indicating the activation of thrombo-inflammatory processes. Furthermore, neutrophils have been shown to contain a pool of FXII, distinct from hepatocyte-derived FXII (178). Upon casting of NETs, neutrophil-FXII is likely to get exposed on the NET surface, where contact activation of FXII may occur. Hence, FXII in COVID-19 lungs might originate from neutrophils infiltrated in the pulmonary tissue.

Besides its role as initiator of intrinsic coagulation, FXII catalyzes the generation of bradykinin (BK) (179), an inflammatory mediator of the kinin peptide family that was shown to be involved in COVID-19-related pulmonary edema (180, 181). FXIIa plasma levels were elevated in COVID-19 patients (**Figs. 5, b,** and **c**). The presence of FXIIa in plasma together with the endothelial barrier dysfunctions present in COVID-19 patients might explain the leakage of FXII from blood into subendothelial tissues. FXIIa-produced BK and NET-associated histones perforate endothelial cells, impacting endothelial barrier integrity (182). Kinins can bind to both kinin B1 and B2 receptors but demonstrate receptor selectivity (183). The B1 receptor is absent in healthy tissues and gets expressed upon injury and inflammation, whereas the B2 receptor is ubiquitously expressed and plays a role in vasodilation, smooth muscle contraction and pain regulation (183). Proteomics analysis of COVID-19 lungs showed the elevation of carboxypeptidase N subunit 1, an enzyme catalyzing the conversion of BK to the metabolite and pulmonary inflammatory factor des-Arg9-BK (184). A key assumption is that COVID-19 causes a functional deficiency of the angiotensin converting enzyme 2 (ACE-2) in the lungs, implicating a slower breakdown of bradykinin and des-Arg9-BK (185). If des-Arg9-BK and other active metabolites remain in circulation for an extended period without clearance by ACE-2, pulmonary vascular permeability surges (186). These processes may result in increased pulmonary edema

and inflammation. Our proteomics analysis also revealed that alanine aminopeptidase N (ANPEP) was reduced in COVID-19 lungs compared to other lung pathologies (**Fig. 3a**). ANPEP plays roles in many physiological processes including tumor angiogenesis and metastasis, blood pressure regulation, and lymphocyte chemotaxis, to name a few (187). ANPEP is expressed by diverse cell types including macrophages and granulocytes and plays a role in the final digestion of peptides prior to antigen presentation (188). ANPEP is inhibited by BK and therapeutic analogs (189, 190), and thus increased BK levels in COVID-19 may favor inflammation by repressing ANPEP activity. Together, our proteomic analysis revealed potential new disease-relevant pathological mechanisms implicated in COVID-19. Further studies are warranted to examine the precise role of carboxypeptidase N subunit 1 and ANPEP in the pathophysiology of COVID-19.

5.3 NET clearance in COVID-19

In line with our data showing increased plasma levels of extracellular DNA and MPO as well as an accumulation of H3cit, NE and chromatin in lung tissue (**Figs. 6, a, b, and 7**), other research groups have shown excessive NET formation in blood samples and lung tissues of COVID-19 patients (80, 82, 191). DNases control levels of extracellular DNA, apoptotic bodies, and NETs, to protect the host from cell damage and thrombo-inflammatory complications (92). Increased NET levels and decreased DNase activity correlated with disease severity in thrombotic microangiopathies and sepsis (192). We found that DNase activity, as well as the capacity to degrade *ex vivo* generated NETs was also reduced in COVID-19 plasma compared to healthy donors (**Fig. 8, a-c**). Concordantly, recombinant human DNase1 (Pulmozyme) improved *ex vivo* NET clearance (**Fig. 8d**), indicating the potentially beneficial effects of DNase therapy for COVID-19 patients.

In contrast to acute COVID-19, we found that patients with long COVID syndrome did not show an increase in circulating extracellular DNA, FXII activation, or DNase activity, implicating that levels of these immunothrombotic markers return to baseline after symptoms had receded for at least 6 weeks (**Fig. 10**). This finding suggests that the highest NET burden is present at the onset and throughout the course of infection

with SARS-CoV-2, which can be explained by increased proinflammatory cytokine/chemokine levels and increased recruitment of granulocytes (193).

5.4 GSDMD and PAD4 are dispensable for NET formation

GSDMD was described as key effector molecule in pyroptosis, an inflammatory caspase-dependent programmed cell death process occurring in innate immune cells (194). Upon cleavage of full-length GSDMD by caspases, the N-terminal fragment localizes to the plasma membrane and induces pore formation resulting in cell lysis(195). Recent reports have resulted in divergent results regarding the importance of GSDMD for plasma membrane rupture during NET formation (58, 62, 196, 197). A study found that downstream activation markers of GSDMD, IL-1α, and IL-1β, correlated with disseminated intravascular coagulation scores in sepsis patients (197). Global genetic or pharmacologic inhibition of GSDMD abrogated NET formation and improved survival in a cecal ligation puncture (CLP)-induced sepsis and an LPS-driven endotoxemia model (58). They also found reduced levels of inflammatory cytokines, including IL-1β and tumor necrosis factor (TNF)-α (58). In another recent report, Liu and colleagues (196) generated a neutrophil-specific conditional GSDMD knockout mouse which they tested in a CLP model. Contradicting the findings from Silva and colleagues (58) they found that GSDMD-deficient neutrophils did *not* protect the mice from sepsis. Mice with GSDMD-deficient neutrophils showed increased tissue damage, high levels of proinflammatory cytokines, and a similar level of NET formation compared to WT mice (196). Hence, hyperinflammation and low bactericidal activity may not be GSDMD-driven in this CLP mouse model. We found that GSDMD was not required for NET formation in two independent vaso-occlusive murine models driven by *E. coli*/LPS-induced septicemia or *Csf3*-driven neutrophilia (**Fig. 15**).

As NET release can occur independent of GSDMD (196), the question arises which alternative GSDMD-independent pathways of NET extrusion may exist? GSDMD cleavage and pore formation in other cell types including platelets may indirectly lead to neutrophil activation and NETosis. GSDMD was upregulated in platelets during CLP sepsis (198). Platelets underwent pyroptosis and released their proinflammatory contents including oxidized mitochondrial DNA, which triggered NET release (198), potentially explaining the increased NET release in global GSDMD knockout mice.

NETs can also be released into the extracellular space through the activation of another pore-forming protein mixed lineage kinase domain-like (MLKL) in mice and humans (199-201). While GSDMD cleavage is known to induce pyroptosis, MLKL has been linked to necroptosis driven by ligand binding of ligands to TNF-associated death domain receptors, pattern recognition receptors, and virus sensors, which support the assembly of the receptor-interacting protein kinase-3 (RIPK3)-MLKL complex (194, 202). Recently, an *Mlkl/Gsdmd* knockout model was reported to be significantly better protected from polymicrobial sepsis compared to single knockout mice (203). High plasma levels of MLKL were shown to be associated with the severity and outcome of sepsis in 188 critically-ill patients (204). Another GSDMD-independent way of NET extrusion may be based on the chemical modification of histones, i.e., a decrease of positive charge reduces the counterforces that normally retain the tight packing of the nucleosomes. This in turn increases the entropic pressure and causes the chromatin to swell, until the exerted pressure exceeds a certain threshold, and the plasma membrane ruptures independent of GSDMD activity (205).

We speculate that CLP and the endotoxemia model (58), using a single i.p. dose of 10 µg/g LPS, may induce a more spontaneous and acute reaction *in vivo*, compared to the lower non-lethal doses we use in our septicemia model (**Fig. 15, A-E**). Our LPS/*E. coli* model might trigger a more chronic, slow-acting pathology, dependent on different pathways of membrane rupture. When setting up the septicemia model, we tested daily i.p. injections of 1 µg/g of LPS, however by day 3 only around 20% of the vasculature was occluded in *D1/D1l3$^{-/-}$*, which was not sufficient for a definite lethal result. To improve the model, the mice were treated with one i.v. injection of heat-killed *E. coli* along with the third LPS injection (92).

Furthermore, research on the effects of different stimuli used to trigger NET formation has yielded inconsistent results in the past. These conflicting results may arise from variations in study design, neutrophil isolation protocols, culturing techniques, or concentrations of the stimuli used (206). There is a broad range of microbial and chemical agents known to stimulate *ex vivo* NET formation. NETs generated by separate pathways and activators may vary in their capacity to fight infections or cause cellular damage (207). A study investigating the impact of different stimuli on canonical (LPS priming and ATP or nigericin via NLR family pyrin domain containing 3 (NLRP3))

and noncanonical (Pam3CSK4 priming and LPS via TLR1/2 and caspase-11, respectively) inflammasome activation found that NET formation is independent of GSDMD (62). Neutrophils from WT and *Gsdmd*^{-/-} mice both formed NETs comprised of comparable amounts of dsDNA, generated the same amounts of ROS, and showed equal degranulation, phagocytosis, and extracellular antibacterial killing activities (62). In contrast to our and another report (58), Stojkov and colleagues (62) found NET formation in PMA-stimulated *Gsdmd*^{-/-} neutrophils. However, they activated neutrophils with 100 nM PMA for 8 h, whereas our stimulation was performed with 10 nM PMA for 4 h (**Fig. 17**) (62). Upon chromatin decondensation and nuclear membrane breakdown, the lack of GSDMD may lead to the retention of decondensed chromatin within the intracellular space in our PMA-dependent setting (**Figs. 17, D and E**).

PAD4 catalyzes the citrullination of histones, thereby weakening the affinity between DNA and histones and facilitating chromatin decondensation (43). The role of PAD4 in NET formation has been discussed in the field and reports have shown a plethora of ambiguous findings (131, 208-210). In line with previous reports, we found that PAD4 deficient neutrophils were able to release NETs *ex vivo* upon stimulation with PMA or A23187 (**Fig. 17**) (29). A23187 mobilizes calcium from the endoplasmic reticulum into the cytosol and mitochondria, which then signals via the PI3K/Akt pathway (40). The enrichment of calcium also initiates the formation of non-selective mitochondrial pores (mPTP) and mtROS which might act as an alternative by-passing mechanism for NET formation, irrespective of PAD4 activation (32, 40). ROS and mtROS stimulate the release of different granule proteins, including MPO and NE which cleave F-actin to dissociate the cytoskeleton and move to the nucleus where they can modify chromatin independent from PAD4 (211).

In vivo, PAD4 has also been shown to be dispensable in murine infection models with *K. pneumoniae* (212) and *C. albicans* (30), in line with our septicemia and sterile neutrophilia findings (**Fig. 16**). WT and *Pad4*^{-/-} mice infected intranasally with *K. pneumoniae* to induce pneumonia-derived sepsis showed similar NET-like structures, cell-free DNA levels, bacterial growth, lung inflammation and organ injury (212). Systemic i.v. infection of *Pad4*^{-/-} mice with *C. albicans* resulted in a loss of histone citrullination, however, NET formation and antifungal activity proceeded independent of PAD4 (30). In the same report, PAD inhibitor Cl-amidine-treated murine neutrophils

which were stimulated with calcium ionophore did indeed cast NETs, which we found as well with the PAD4 inhibitor GSK484 (**Fig. 17**). Hence, alternative pathways of chromatin decondensation, e.g., by NE-mediated histone and lamin breakdown, may compensate for the lack of PAD4, enabling the progression of NET formation (213). This report and others question the relative importance of histone citrullination by PAD4 in NET formation (41, 43, 208, 214, 215).

Our study demonstrated that the formation of lethal NET-derived vaso-occlusions in mice during sterile neutrophilia proceeds in the absence of GSDMD and PAD4. In conclusion, it must be noted that GSDMD and PAD4 encompass a complicated role in NET formation and neutrophil cell death and that their proposed roles in these pathways must be revisited.

5.5 Recombinant human DNase1 in disease and therapy

Recombinant human DNase1 (Pulmozyme) is indicated, along with standard therapies, for the management of pediatric and adult patients with CF to improve pulmonary function (120, 216, 217). Inhaled Pulmozyme causes mild adverse effects, with the most common being voice alterations, discomfort in the throat, and rash (218). Due to its beneficial safety profile and effectiveness in CF, Pulmozyme was tested in different pathologies such as cancer (ClinicalTrials.gov identifier: NCT00536952), ischemic stroke (ClinicalTrials.gov identifier: NCT05203224), Alzheimer's disease (219), and primarily respiratory disorders including acute severe asthma (220), empyema thoracis (221), atelectasis (122), and COVID-19 infection (222, 223). A study on empyema thoracis patients showed that intrapleural administration of Pulmozyme significantly improved the passage of pus and reduced its viscosity (221, 224). Pulmozyme has also shown beneficial effects for the refractory treatment of intubated patients with asthma (220, 225).

Besides respiratory conditions, Pulmozyme was also tested in a randomized, double-masked, placebo-controlled phase Ib trial including 17 patients with lupus nephritis (226). SLE and lupus nephritis are characterized by the development of autoantibodies against nuclear antigens such as dsDNA. The formation and deposition of IgG-dsDNA immune complexes in glomeruli contribute to disease pathogenesis and complement

activation. Pulmozyme catalyzes the hydrolysis of extracellular DNA, postpones dsDNA antibody generation, reduces proteinuria, and extends survival in a lupus-prone mouse model (227). A single intravenous dose followed by 10 subcutaneous doses of Pulmozyme proved to be safe in lupus nephritis patients (226). However, disease biomarkers, including dsDNA antibodies, complement factors C3 and C4, and cytokines were comparable between treatment and placebo groups. Thus, treatment with Pulmozyme did not result in better outcomes in lupus nephritis patients (226).

DNase treatment has also been shown to inhibit tumor cell proliferation *in vitro*, prevent blood-borne liver metastasis, and enhance tumor cell clearance in the pulmonary microvasculature of rats (228-230). Indeed, recombinant bovine pancreatic DNase1 fused to a single-chain Fv antibody fragment against human placental alkaline phosphatase performed a dual activity by degrading DNA and binding to the tumor antigen (231). The chimeric molecule displayed both DNA-degrading and antigen-binding activity *in vitro*, exhibiting significant cytotoxicity towards cells expressing the human placental alkaline phosphatase. Taken together, engineered DNases are crucial to digest extracellular DNA and NETs and thus alleviate thrombo-inflammatory conditions.

5.6 Engineered DNase variants as a novel treatment option

We designed a DNase1 variant containing three amino acid stretches, G, K, and O (**Table 3, Figs. 20** and **21**) from DNase1L3, which allowed for the transfer of its chromatin-degrading activity to DNase1. The newly produced DNase1^{G,K,O} variant was stable in serum and bile (**Fig. 23**), and efficiently cleaved both dsDNA and chromatin (**Fig. 22**), as well as *ex vivo* generated NETs (**Fig. 24**). The amino acid stretches G and K comprise the residues H86 – R95 and A136 – V138 which are involved in binding of DNase1 to its inhibitor G-actin. This is relevant in diseases such as CF, where the viscous sputum contains actin and extracellular DNA from dead leukocytes and epithelial cells (232). In 1996, Genentech (San Francisco, CA, USA) developed G-actin-resistant DNase1 variants that reduced the mucus viscosity of CF patients 10- to 50-fold more potently than native DNase1 (233). Experimental studies have also shown that actin-resistant DNase1 variants have a therapeutic benefit in murine models of lupus nephritis (234, 235). Upon substituting actin-binding regions in

DNase1 with the amino acids from DNase1L3 which do not interact with actin, the DNase1^{G,K,O} variant may show an increased activity because it is less prone to inhibition by actin (123). The third substituted amino acid stretch O (P*KK*AW*K*NIRLRTD substituting RPSQWSSIRLWTS, **Table 3, Figs. 20** and **21**), carries three positively charged lysine residues, potentially increasing the DNA-binding affinity and DNA-degrading activity of our DNase1^O variant.

Our findings challenge the current concept that DNase1L3 executes its chromatin-degrading activity via its C-terminal domain (111, 112). Our designed variants display chromatin degradation upon the transfer of non-conserved regions within the core body of the enzyme (**Fig. 22**). Protein structure analyses will offer a more detailed understanding of the mechanistic effects caused by these amino acid substitutions from DNase1L3 to DNase1. We speculate that swapping sequences from one DNase to another generates variants with potentially lower immunogenicity and autoantibody production compared to the addition or exchange of *de novo* synthesized sequences (**Fig. 19**). We detected DNase1^{G,K,O} in serum and bile one week after expression of the variant by hydrodynamic tail vein injection in mice, suggesting that immunogenic effects such as reduced efficacy, anaphylaxis, and autoimmunity of the constructs are minimal (**Fig. 23**). These preliminary data favor further pharmacological studies including the effects of long-term or repeated applications.

The engineered variant DNase1^{G,K,O} offers a promising tool for the interference with NET-associated pathologies of the blood circulatory and biliary system. Treatment with recombinant human DNase1 improved prognosis in murine stroke models by recanalization of occluded vessels (236, 237), motivating therapeutic use of DNase mutants for thromboprotection. The engineered DNase1 variant will potentially allow for a quicker resolution of circulating DNA and NET accumulations, due to its increased enzymatic activity. We speculate that the DNase1^{G,K,O} variant may be therapeutically beneficial in NET-associated thrombo-inflammatory disorders such as DVT, ischemic stroke, and myocardial infarction. Hence, the next step of this project would require testing of the variants in experimental models of thrombo-inflammation. The presence of the DNase1^{G,K,O} variant in bile advocates its potential use for targeting NETs in inflammatory biliary diseases such as primary sclerosing cholangitis. The novel DNase

variant could also be used to target NET-driven occlusive disease models such as septicemia and chronic neutrophilia (92).

Secreted DNases seem to play a crucial role in the digestion of excessive NETs to facilitate the restoration of homeostasis in COVID-19. There have been several clinical trials testing Pulmozyme for the treatment of COVID-19. In a non-randomized, case-controlled phase 3 trial (NCT04402970, "DORNASESARS2") by the University of Missouri-Columbia, mechanically ventilated patients with COVID-19-related ARDS were treated with nebulized Pulmozyme and blood samples were quantified for NETs (222). Treating COVID-19 patients with Pulmozyme improved oxygenation and reduced DNA-MPO complexes in the bronchoalveolar lavage fluid, limited to the time of drug delivery, suggesting that the use of other DNase variants could further increase the NET degradation rate. Based on the effective NET degradation seen with our engineered DNase1^{G,K,O} variant (**Fig. 24**), a positive outcome with DNase1^{G,K,O} for the treatment of respiratory symptoms in COVID-19 can be speculated.

Taken together, I designed a recombinant human DNase1 variant that efficiently degrades both dsDNA and chromatin, serving as a potential therapy for pathologies driven by unresolved inflammation, extracellular DNA, and NETs. We also found that the formation of lethal NET-mediated vascular occlusions occurred independently of histone-citrullinating enzyme PAD4 and pore-forming protein GSDMD in two murine models of thrombo-inflammation. Furthermore, we show that the NETs/FXIIa axis contributes to thrombo-inflammatory events in COVID-19 and VITT but has no role for long COVID. Thus FXII/FXIIa blocking agents and engineered DNases during early onset of disease may offer a therapeutic strategy for interfering with coagulopathy and hyperinflammation in COVID-19 lung pathology and other thrombo-inflammatory disease states.

6. Abstract

Inflammation serves as protection against pathogen invasion and tissue injury but is also a hallmark of various diseases. Neutrophils play a crucial role in inflammation by forming Neutrophil Extracellular Traps (NETs) to combat pathogens. However, excessive NET formation and improper clearance are associated with thrombo-inflammatory disorders. The proteins PAD4, and GSDMD are considered to be critical for NET formation, while DNase1 and DNase1-like 3 (DNase1L3) are crucial for NET degradation in circulation. In our study, we investigated the importance of these factors in two independent *in vivo* NET formation models, sterile neutrophilia, and septicemia. Unexpectedly, mice deficient in *Pad4* and *Gsdmd* did not survive sepsis, while the reference *Myd88* knockout mice, serving as control for our disease models survived. Additionally, *Pad4* and *Gsdmd* deficiencies did not hinder interfere with NET formation during neutrophilia, leading to lethal NET-mediated pulmonary embolism and organ damage. NETs contribute to pulmonary thrombo-inflammation in several diseases including COVID-19. Immunostaining, immunoblotting and proteomics of COVID-19 postmortem lung tissues and plasma revealed FXII expression, activation, and colocalization of FXIIa and NETs. In contrast to acute thrombo-inflammation, we did not detect these effects in long COVID patient plasma, implicating the primary importance of the NETs/FXIIa axis in acute inflammation. Furthermore, we detected NET markers in plasma and cerebral venous sinus thrombi of patients with the SARS-Cov-2 vaccine-induced condition VITT. Impaired NET clearance by DNases contributed to NET accumulation and FXII activation in COVID-19 plasma, which was improved by DNase1 substitution. Consequently, the prevention of the pathological effects of NETs largely depends on efficient degradation by DNases, which led us to the engineering of recombinant human DNase1 variants. Zymography and gel electrophoresis assays showed that the transfer of three amino acid stretches from DNase1L3 to DNase1 resulted in a hyperactive enzymatic variant capable of degrading dsDNA, chromatin, and NETs efficiently.

Collectively, our findings demonstrate the involvement of the NETs/FXIIa axis in COVID-19 and VITT and propose DNase-based interventions to mitigate NET-driven and thrombo-inflammatory pathologies.

7. Zusammenfassung

Neutrophile spielen eine entscheidende Rolle bei Entzündungen, indem sie Neutrophil Extracellular Traps (NETs) bilden, um Pathogene zu bekämpfen. Eine übermäßige NET-Bildung und ein unzureichender Abbau sind jedoch mit thrombo-inflammatorischen Störungen verbunden. Die Proteine PAD4 und GSDMD gelten als entscheidend für die NET-Bildung, während DNase1 und DNase1-like 3 (DNase1L3) für den NET-Abbau im Blutkreislauf notwendig sind. In dieser Studie haben wir den Einfluss von PAD4 und GSDMD für NET-vermittelte Gefäßverschlüsse und Organschäden in der sterilen Neutrophilie und der Septikämie, untersucht. Unerwarteterweise überlebten *Pad4-* und *Gsdmd-*defiziente Mäuse die sterile Neutrophilie und die Septikämie nicht. *Pad4-* und *Gsdmd-*Defizienz reduzierte die NET-Bildung bei Neutrophilie nicht, was zu tödlichen NET-vermittelten Lungenembolien und Organschäden führte. NETs tragen weiterhin zur pulmonalen Thrombo-Inflammation bei COVID-19 bei. Immunfärbungen, Immunblots und Proteomik von postmortalen Lungengeweben und Plasma von COVID-19-Patient*innen zeigten erhöhte FXII-Expression, -Aktivierung und eine Kolokalisation von FXIIa und NETs. In long COVID Plasma konnten wir prokoagulante Effekte nicht nachweisen, was primär auf die Bedeutung der NETs/FXIIa-Achse bei akuten Entzündungen hindeutet. Darüber hinaus wiesen wir NET-Marker im Plasma und in zerebralen venösen Sinusthromben von Patient*innen mit der durch den AstraZeneca SARS-CoV-2-Impfstoff ausgelösten Vakzin-induzierten immunthrombotischen Thrombozytopenie (VITT) nach. Ein gestörter NET-Abbau durch DNase-Defizienz trug zur NET-Akkumulation und FXII-Aktivierung bei, was durch DNase1-Substitution verbessert wurde. Die Verhinderung der pathologischen Auswirkungen von NETs hängt weitgehend von einem effizienten Abbau durch DNasen ab, was uns zur Entwicklung von rekombinanten humanen DNase1-Varianten führte. Zymographie- und Gelelektrophorese-Assays zeigten, dass die Übertragung von drei Aminosäuresequenzen von DNase1L3 auf DNase1 zu einer hyperaktiven enzymatischen Variante führte, die in der Lage ist, dsDNA, Chromatin und NETs effizient abzubauen. Insgesamt zeigen unsere Ergebnisse die Beteiligung der NETs/FXIIa-Achse an thrombo-inflammatorischen Ereignissen bei COVID-19 und schlagen DNase-basierte Interventionen zur Verringerung von Koagulopathien und übermäßigen Entzündungsreaktionen in der Lungenpathologie von COVID-19 vor.

8. List of Abbreviations

ANPEP	Alanine aminopeptidase N
ARDS	Acute respiratory distress syndrome
AU	Arbitrary unit
BK	Bradykinin
BSA	Bovine serum albumin
C. albicans	*Candida albicans*
cDNA	Complementary DNA
ceDNA	Circulating extracellular DNA
CF	Cystic fibrosis
CI	Confidence interval
CLP	Cecal ligation puncture
COVID-19	Coronavirus disease
CRP	C-reactive protein
Csf3	Colony stimulating factor 3
CTRL	Control
CVST	Cerebral venous sinus thrombosis
DMEM	Dulbecco's modified eagle medium
DNA	Deoxyribonucleic acid
DNase 1	Deoxyribonuclease 1
DNase1L3	Deoxyribonuclease 1 like-3
dsDNA	Double stranded DNA
DVT	Deep vein thrombosis
E. coli	*Escherichia coli*
EDTA	Ethylenediaminetetraacetic acid
FOV	Field of view
FXII	Factor XII
FXIIa	Activated FXII
G-CSF	Granulocyte colony stimulating factor
GSDMD	Gasdermin D
H&E	Hematoxylin & Eosin
H3cit	Citrullinated histone H3
HEK cells	Human embryonic kidney cells
IL	Interleukin
IQR	Interquartile range
LPS	Lipopolysaccharide
MPO	Myeloperoxidase
mtROS	Mitochondrial reactive oxygen species
MYD88	Myeloid differentiation primary response 88
NADPH	Nicotinamide adenine dinucleotide phosphate hydrogen
NE	Neutrophil elastase
NETs	Neutrophil Extracellular Traps
NLS	Nuclear localization signal
NSA	Necrosulfonamide
PAD4	Peptidyl arginine deaminase 4
PBS	Phosphate buffered saline
PCR	Polymerase chain reaction
PE	Pulmonary embolism
PF4	Platelet factor 4
PMA	Phorbol myristate acetate

RNA	Ribonucleic acid
ROS	Reactive oxygen species
RT	Room temperature
SARS-CoV-2	Severe acute respiratory syndrome coronavirus 2
SLE	Systemic lupus erythematosus
SRED	Single radial enzyme diffusion
TLR	Toll-like receptor
UKE	University Medical Center Hamburg
VITT	Vaccine-induced immune thrombotic thrombocytopenia
vWF	von Willebrand factor
WT	Wild-type

9. References

1. Englert H, Rangaswamy C, Deppermann C, Sperhake JP, Krisp C, Schreier D, et al. Defective NET clearance contributes to sustained FXII activation in COVID-19-associated pulmonary thrombo-inflammation. EBioMedicine. 2021;67:103382.
2. Fogarty H, Townsend L, Morrin H, Ahmad A, Comerford C, Karampini E, et al. Persistent endotheliopathy in the pathogenesis of long COVID syndrome. J Thromb Haemost. 2021;19(10):2546-53.
3. Greinacher A, Selleng K, Palankar R, Wesche J, Handtke S, Wolff M, et al. Insights in ChAdOx1 nCoV-19 vaccine-induced immune thrombotic thrombocytopenia. Blood. 2021;138(22):2256-68.
4. Englert H, Gobel J, Khong D, Omidi M, Wolska N, Konrath S, et al. Targeting NETs using dual-active DNase1 variants. Front Immunol. 2023;14:1181761.
5. Soehnlein O, Steffens S, Hidalgo A, Weber C. Neutrophils as protagonists and targets in chronic inflammation. Nat Rev Immunol. 2017;17(4):248-61.
6. Ragab D, Salah Eldin H, Taeimah M, Khattab R, Salem R. The COVID-19 Cytokine Storm; What We Know So Far. Front Immunol. 2020;11:1446.
7. Navab M, Gharavi N, Watson AD. Inflammation and metabolic disorders. Curr Opin Clin Nutr Metab Care. 2008;11(4):459-64.
8. Summers C, Rankin SM, Condliffe AM, Singh N, Peters AM, Chilvers ER. Neutrophil kinetics in health and disease. Trends Immunol. 2010;31(8):318-24.
9. Lawrence SM, Corriden R, Nizet V. The Ontogeny of a Neutrophil: Mechanisms of Granulopoiesis and Homeostasis. Microbiol Mol Biol Rev. 2018;82(1).
10. Pruchniak MP, Arazna M, Demkow U. Life of neutrophil: from stem cell to neutrophil extracellular trap. Respir Physiol Neurobiol. 2013;187(1):68-73.
11. van Grinsven E, Textor J, Hustin LSP, Wolf K, Koenderman L, Vrisekoop N. Immature Neutrophils Released in Acute Inflammation Exhibit Efficient Migration despite Incomplete Segmentation of the Nucleus. J Immunol. 2019;202(1):207-17.
12. Hollenstein U, Homoncik M, Stohlawetz PJ, Marsik C, Sieder A, Eichler HG, et al. Endotoxin down-modulates granulocyte colony-stimulating factor receptor (CD114) on human neutrophils. J Infect Dis. 2000;182(1):343-6.
13. Gordon S, Taylor PR. Monocyte and macrophage heterogeneity. Nat Rev Immunol. 2005;5(12):953-64.
14. Brinkmann V, Reichard U, Goosmann C, Fauler B, Uhlemann Y, Weiss DS, et al. Neutrophil extracellular traps kill bacteria. Science. 2004;303(5663):1532-5.
15. Urban CF, Ermert D, Schmid M, Abu-Abed U, Goosmann C, Nacken W, et al. Neutrophil extracellular traps contain calprotectin, a cytosolic protein complex involved in host defense against Candida albicans. PLoS Pathog. 2009;5(10):e1000639.
16. Dwyer M, Shan Q, D'Ortona S, Maurer R, Mitchell R, Olesen H, et al. Cystic fibrosis sputum DNA has NETosis characteristics and neutrophil extracellular trap release is regulated by macrophage migration-inhibitory factor. J Innate Immun. 2014;6(6):765-79.
17. Marcos V, Zhou-Suckow Z, Onder Yildirim A, Bohla A, Hector A, Vitkov L, et al. Free DNA in cystic fibrosis airway fluids correlates with airflow obstruction. Mediators Inflamm. 2015;2015:408935.

18. Hakkim A, Furnrohr BG, Amann K, Laube B, Abed UA, Brinkmann V, et al. Impairment of neutrophil extracellular trap degradation is associated with lupus nephritis. Proc Natl Acad Sci U S A. 2010;107(21):9813-8.

19. Khandpur R, Carmona-Rivera C, Vivekanandan-Giri A, Gizinski A, Yalavarthi S, Knight JS, et al. NETs are a source of citrullinated autoantigens and stimulate inflammatory responses in rheumatoid arthritis. Sci Transl Med. 2013;5(178):178ra40.

20. Xiao Y, Cong M, Li J, He D, Wu Q, Tian P, et al. Cathepsin C promotes breast cancer lung metastasis by modulating neutrophil infiltration and neutrophil extracellular trap formation. Cancer Cell. 2021;39(3):423-37 e7.

21. Yang L, Liu Q, Zhang X, Liu X, Zhou B, Chen J, et al. DNA of neutrophil extracellular traps promotes cancer metastasis via CCDC25. Nature. 2020;583(7814):133-8.

22. Borissoff JI, Joosen IA, Versteylen MO, Brill A, Fuchs TA, Savchenko AS, et al. Elevated levels of circulating DNA and chromatin are independently associated with severe coronary atherosclerosis and a prothrombotic state. Arterioscler Thromb Vasc Biol. 2013;33(8):2032-40.

23. Jimenez-Alcazar M, Napirei M, Panda R, Kohler EC, Kremer Hovinga JA, Mannherz HG, et al. Impaired DNase1-mediated degradation of neutrophil extracellular traps is associated with acute thrombotic microangiopathies. J Thromb Haemost. 2015;13(5):732-42.

24. Mangold A, Alias S, Scherz T, Hofbauer M, Jakowitsch J, Panzenbock A, et al. Coronary neutrophil extracellular trap burden and deoxyribonuclease activity in ST-elevation acute coronary syndrome are predictors of ST-segment resolution and infarct size. Circ Res. 2015;116(7):1182-92.

25. Takei H, Araki A, Watanabe H, Ichinose A, Sendo F. Rapid killing of human neutrophils by the potent activator phorbol 12-myristate 13-acetate (PMA) accompanied by changes different from typical apoptosis or necrosis. J Leukoc Biol. 1996;59(2):229-40.

26. Behnen M, Leschczyk C, Moller S, Batel T, Klinger M, Solbach W, et al. Immobilized immune complexes induce neutrophil extracellular trap release by human neutrophil granulocytes via FcgammaRIIIB and Mac-1. J Immunol. 2014;193(4):1954-65.

27. Warnatsch A, Ioannou M, Wang Q, Papayannopoulos V. Inflammation. Neutrophil extracellular traps license macrophages for cytokine production in atherosclerosis. Science. 2015;349(6245):316-20.

28. Martinod K, Fuchs TA, Zitomersky NL, Wong SL, Demers M, Gallant M, et al. PAD4-deficiency does not affect bacteremia in polymicrobial sepsis and ameliorates endotoxemic shock. Blood. 2015;125(12):1948-56.

29. Kenny EF, Herzig A, Kruger R, Muth A, Mondal S, Thompson PR, et al. Diverse stimuli engage different neutrophil extracellular trap pathways. Elife. 2017;6.

30. Guiducci E, Lemberg C, Kung N, Schraner E, Theocharides APA, LeibundGut-Landmann S. Candida albicans-Induced NETosis Is Independent of Peptidylarginine Deiminase 4. Front Immunol. 2018;9:1573.

31. Hakkim A, Fuchs TA, Martinez NE, Hess S, Prinz H, Zychlinsky A, et al. Activation of the Raf-MEK-ERK pathway is required for neutrophil extracellular trap formation. Nat Chem Biol. 2011;7(2):75-7.

32. Vorobjeva N, Galkin I, Pletjushkina O, Golyshev S, Zinovkin R, Prikhodko A, et al. Mitochondrial permeability transition pore is involved in oxidative burst and NETosis of human neutrophils. Biochim Biophys Acta Mol Basis Dis. 2020;1866(5):165664.

33. Vorobjeva NV, Chernyak BV. NETosis: Molecular Mechanisms, Role in Physiology and Pathology. Biochemistry (Mosc). 2020;85(10):1178-90.

34. Rosazza T, Warner J, Sollberger G. NET formation - mechanisms and how they relate to other cell death pathways. FEBS J. 2021;288(11):3334-50.

35. Yipp BG, Kubes P. NETosis: how vital is it? Blood. 2013;122(16):2784-94.

36. Pilsczek FH, Salina D, Poon KK, Fahey C, Yipp BG, Sibley CD, et al. A novel mechanism of rapid nuclear neutrophil extracellular trap formation in response to Staphylococcus aureus. J Immunol. 2010;185(12):7413-25.

37. Yipp BG, Petri B, Salina D, Jenne CN, Scott BN, Zbytnuik LD, et al. Infection-induced NETosis is a dynamic process involving neutrophil multitasking in vivo. Nat Med. 2012;18(9):1386-93.

38. Clark SR, Ma AC, Tavener SA, McDonald B, Goodarzi Z, Kelly MM, et al. Platelet TLR4 activates neutrophil extracellular traps to ensnare bacteria in septic blood. Nat Med. 2007;13(4):463-9.

39. Etulain J, Martinod K, Wong SL, Cifuni SM, Schattner M, Wagner DD. P-selectin promotes neutrophil extracellular trap formation in mice. Blood. 2015;126(2):242-6.

40. Douda DN, Khan MA, Grasemann H, Palaniyar N. SK3 channel and mitochondrial ROS mediate NADPH oxidase-independent NETosis induced by calcium influx. Proc Natl Acad Sci U S A. 2015;112(9):2817-22.

41. Li P, Li M, Lindberg MR, Kennett MJ, Xiong N, Wang Y. PAD4 is essential for antibacterial innate immunity mediated by neutrophil extracellular traps. J Exp Med. 2010;207(9):1853-62.

42. Neeli I, Khan SN, Radic M. Histone deimination as a response to inflammatory stimuli in neutrophils. J Immunol. 2008;180(3):1895-902.

43. Wang Y, Li M, Stadler S, Correll S, Li P, Wang D, et al. Histone hypercitrullination mediates chromatin decondensation and neutrophil extracellular trap formation. J Cell Biol. 2009;184(2):205-13.

44. Tsourouktsoglou TD, Warnatsch A, Ioannou M, Hoving D, Wang Q, Papayannopoulos V. Histones, DNA, and Citrullination Promote Neutrophil Extracellular Trap Inflammation by Regulating the Localization and Activation of TLR4. Cell Rep. 2020;31(5):107602.

45. Metzler KD, Goosmann C, Lubojemska A, Zychlinsky A, Papayannopoulos V. A myeloperoxidase-containing complex regulates neutrophil elastase release and actin dynamics during NETosis. Cell Rep. 2014;8(3):883-96.

46. Papayannopoulos V, Metzler KD, Hakkim A, Zychlinsky A. Neutrophil elastase and myeloperoxidase regulate the formation of neutrophil extracellular traps. J Cell Biol. 2010;191(3):677-91.

47. Akira S, Takeda K. Toll-like receptor signalling. Nat Rev Immunol. 2004;4(7):499-511.

48. Martin MU, Wesche H. Summary and comparison of the signaling mechanisms of the Toll/interleukin-1 receptor family. Biochim Biophys Acta. 2002;1592(3):265-80.

49. Pacquelet S, Johnson JL, Ellis BA, Brzezinska AA, Lane WS, Munafo DB, et al. Cross-talk between IRAK-4 and the NADPH oxidase. Biochem J. 2007;403(3):451-61.

50. West AP, Brodsky IE, Rahner C, Woo DK, Erdjument-Bromage H, Tempst P, et al. TLR signalling augments macrophage bactericidal activity through mitochondrial ROS. Nature. 2011;472(7344):476-80.

51. Kawasaki T, Kawai T. Toll-like receptor signaling pathways. Front Immunol. 2014;5:461.

52. Liu Z, Gan L, Xu Y, Luo D, Ren Q, Wu S, et al. Melatonin alleviates inflammasome-induced pyroptosis through inhibiting NF-kappaB/GSDMD signal in mice adipose tissue. J Pineal Res. 2017;63(1).

53. Sharma D, Kanneganti TD. The cell biology of inflammasomes: Mechanisms of inflammasome activation and regulation. J Cell Biol. 2016;213(6):617-29.

54. Shi J, Zhao Y, Wang K, Shi X, Wang Y, Huang H, et al. Cleavage of GSDMD by inflammatory caspases determines pyroptotic cell death. Nature. 2015;526(7575):660-5.

55. Kamajaya LJ, Boucher D. Gasdermin D Cleavage Assay Following Inflammasome Activation. Methods Mol Biol. 2022;2459:39-49.

56. Sborgi L, Ruhl S, Mulvihill E, Pipercevic J, Heilig R, Stahlberg H, et al. GSDMD membrane pore formation constitutes the mechanism of pyroptotic cell death. EMBO J. 2016;35(16):1766-78.

57. Silva CMS, Wanderley CWS, Veras FP, Goncalves AV, Lima MHF, Toller-Kawahisa JE, et al. Gasdermin-D activation by SARS-CoV-2 triggers NET and mediate COVID-19 immunopathology. Crit Care. 2022;26(1):206.

58. Silva CMS, Wanderley CWS, Veras FP, Sonego F, Nascimento DC, Goncalves AV, et al. Gasdermin D inhibition prevents multiple organ dysfunction during sepsis by blocking NET formation. Blood. 2021;138(25):2702-13.

59. Xie J, Zhu CL, Wan XJ, Zhao ZZ, Meng Y, Li P, et al. GSDMD-mediated NETosis promotes the development of acute respiratory distress syndrome. Eur J Immunol. 2023;53(1):e2250011.

60. Chen KW, Monteleone M, Boucher D, Sollberger G, Ramnath D, Condon ND, et al. Noncanonical inflammasome signaling elicits gasdermin D-dependent neutrophil extracellular traps. Sci Immunol. 2018;3(26).

61. Sollberger G, Choidas A, Burn GL, Habenberger P, Di Lucrezia R, Kordes S, et al. Gasdermin D plays a vital role in the generation of neutrophil extracellular traps. Sci Immunol. 2018;3(26).

62. Stojkov D, Claus MJ, Kozlowski E, Oberson K, Scharen OP, Benarafa C, et al. NET formation is independent of gasdermin D and pyroptotic cell death. Sci Signal. 2023;16(769):eabm0517.

63. Jorch SK, Kubes P. An emerging role for neutrophil extracellular traps in noninfectious disease. Nat Med. 2017;23(3):279-87.

64. Stark K, Massberg S. Interplay between inflammation and thrombosis in cardiovascular pathology. Nat Rev Cardiol. 2021;18(9):666-82.

65. von Bruhl ML, Stark K, Steinhart A, Chandraratne S, Konrad I, Lorenz M, et al. Monocytes, neutrophils, and platelets cooperate to initiate and propagate venous thrombosis in mice in vivo. J Exp Med. 2012;209(4):819-35.

66. Stark K. Platelet-neutrophil crosstalk and netosis. Hemasphere. 2019;3(Suppl).

67. Fuchs TA, Brill A, Duerschmied D, Schatzberg D, Monestier M, Myers DD, Jr., et al. Extracellular DNA traps promote thrombosis. Proc Natl Acad Sci U S A. 2010;107(36):15880-5.

68. Semeraro F, Ammollo CT, Morrissey JH, Dale GL, Friese P, Esmon NL, et al. Extracellular histones promote thrombin generation through platelet-dependent mechanisms: involvement of platelet TLR2 and TLR4. Blood. 2011;118(7):1952-61.

69. Massberg S, Grahl L, von Bruehl ML, Manukyan D, Pfeiler S, Goosmann C, et al. Reciprocal coupling of coagulation and innate immunity via neutrophil serine proteases. Nat Med. 2010;16(8):887-96.

70. Oehmcke S, Morgelin M, Herwald H. Activation of the human contact system on neutrophil extracellular traps. J Innate Immun. 2009;1(3):225-30.

71. Noubouossie DF, Whelihan MF, Yu YB, Sparkenbaugh E, Pawlinski R, Monroe DM, et al. In vitro activation of coagulation by human neutrophil DNA and histone proteins but not neutrophil extracellular traps. Blood. 2017;129(8):1021-9.

72. World Health Organization. WHO Coronavirus (COVID-19) Dashboard n.d. [Available from: https://covid19.who.int/.

73. Chen G, Wu D, Guo W, Cao Y, Huang D, Wang H, et al. Clinical and immunological features of severe and moderate coronavirus disease 2019. J Clin Invest. 2020;130(5):2620-9.

74. Tang N, Li D, Wang X, Sun Z. Abnormal coagulation parameters are associated with poor prognosis in patients with novel coronavirus pneumonia. J Thromb Haemost. 2020;18(4):844-7.

75. Zhou F, Yu T, Du R, Fan G, Liu Y, Liu Z, et al. Clinical course and risk factors for mortality of adult inpatients with COVID-19 in Wuhan, China: a retrospective cohort study. Lancet. 2020;395(10229):1054-62.

76. Aid M, Busman-Sahay K, Vidal SJ, Maliga Z, Bondoc S, Starke C, et al. Vascular Disease and Thrombosis in SARS-CoV-2-Infected Rhesus Macaques. Cell. 2020;183(5):1354-66 e13.

77. Goshua G, Pine AB, Meizlish ML, Chang CH, Zhang H, Bahel P, et al. Endotheliopathy in COVID-19-associated coagulopathy: evidence from a single-centre, cross-sectional study. Lancet Haematol. 2020;7(8):e575-e82.

78. Mancini I, Baronciani L, Artoni A, Colpani P, Biganzoli M, Cozzi G, et al. The ADAMTS13-von Willebrand factor axis in COVID-19 patients. J Thromb Haemost. 2021;19(2):513-21.

79. Rossaint J, Herter JM, Van Aken H, Napirei M, Doring Y, Weber C, et al. Synchronized integrin engagement and chemokine activation is crucial in neutrophil extracellular trap-mediated sterile inflammation. Blood. 2014;123(16):2573-84.

80. Veras FP, Pontelli MC, Silva CM, Toller-Kawahisa JE, de Lima M, Nascimento DC, et al. SARS-CoV-2-triggered neutrophil extracellular traps mediate COVID-19 pathology. J Exp Med. 2020;217(12).

81. Barnes BJ, Adrover JM, Baxter-Stoltzfus A, Borczuk A, Cools-Lartigue J, Crawford JM, et al. Targeting potential drivers of COVID-19: Neutrophil extracellular traps. J Exp Med. 2020;217(6).

82. Zuo Y, Yalavarthi S, Shi H, Gockman K, Zuo M, Madison JA, et al. Neutrophil extracellular traps in COVID-19. JCI Insight. 2020;5(11).

83. Agency EM. COVID-19 Vaccine AstraZeneca: PRAC investigating cases of thromboembolic events - vaccine's benefits currently still outweigh risks - Update 2021 [Available from: https://www.ema.europa.eu/en/news/covid-19-vaccine-astrazeneca-prac-investigating-cases-thromboembolic-events-vaccines-benefits.

84. Greinacher A, Langer F, Makris M, Pai M, Pavord S, Tran H, et al. Vaccine-induced immune thrombotic thrombocytopenia (VITT): Update on diagnosis and management considering different resources. J Thromb Haemost. 2022;20(1):149-56.

85. Greinacher A, Thiele T, Warkentin TE, Weisser K, Kyrle PA, Eichinger S. Thrombotic Thrombocytopenia after ChAdOx1 nCov-19 Vaccination. N Engl J Med. 2021;384(22):2092-101.

86. Manda-Handzlik A, Demkow U. Neutrophils: The Role of Oxidative and Nitrosative Stress in Health and Disease. Adv Exp Med Biol. 2015;857:51-60.

87. Haider P, Kral-Pointner JB, Mayer J, Richter M, Kaun C, Brostjan C, et al. Neutrophil Extracellular Trap Degradation by Differently Polarized Macrophage Subsets. Arterioscler Thromb Vasc Biol. 2020;40(9):2265-78.

88. Majer O, Liu B, Barton GM. Nucleic acid-sensing TLRs: trafficking and regulation. Curr Opin Immunol. 2017;44:26-33.

89. Santa P, Garreau A, Serpas L, Ferriere A, Blanco P, Soni C, et al. The Role of Nucleases and Nucleic Acid Editing Enzymes in the Regulation of Self-Nucleic Acid Sensing. Front Immunol. 2021;12:629922.

90. Soni C, Reizis B. Self-DNA at the Epicenter of SLE: Immunogenic Forms, Regulation, and Effects. Front Immunol. 2019;10:1601.

91. Roers A, Hiller B, Hornung V. Recognition of Endogenous Nucleic Acids by the Innate Immune System. Immunity. 2016;44(4):739-54.

92. Jimenez-Alcazar M, Rangaswamy C, Panda R, Bitterling J, Simsek YJ, Long AT, et al. Host DNases prevent vascular occlusion by neutrophil extracellular traps. Science. 2017;358(6367):1202-6.

93. Li N, Zheng X, Chen M, Huang L, Chen L, Huo R, et al. Deficient DNASE1L3 facilitates neutrophil extracellular traps-induced invasion via cyclic GMP-AMP synthase and the non-canonical NF-kappaB pathway in diabetic hepatocellular carcinoma. Clin Transl Immunology. 2022;11(4):e1386.

94. Laukova L, Konecna B, Janovicova L, Vlkova B, Celec P. Deoxyribonucleases and Their Applications in Biomedicine. Biomolecules. 2020;10(7).

95. Farrera C, Fadeel B. Macrophage clearance of neutrophil extracellular traps is a silent process. J Immunol. 2013;191(5):2647-56.

96. Delgado-Rizo V, Martinez-Guzman MA, Iniguez-Gutierrez L, Garcia-Orozco A, Alvarado-Navarro A, Fafutis-Morris M. Neutrophil Extracellular Traps and Its Implications in Inflammation: An Overview. Front Immunol. 2017;8:81.

97. Fischer H, Szabo S, Scherz J, Jaeger K, Rossiter H, Buchberger M, et al. Essential role of the keratinocyte-specific endonuclease DNase1L2 in the removal of nuclear DNA from hair and nails. J Invest Dermatol. 2011;131(6):1208-15.

98. Kawane K, Fukuyama H, Kondoh G, Takeda J, Ohsawa Y, Uchiyama Y, et al. Requirement of DNase II for definitive erythropoiesis in the mouse fetal liver. Science. 2001;292(5521):1546-9.

99. Nishimoto S, Kawane K, Watanabe-Fukunaga R, Fukuyama H, Ohsawa Y, Uchiyama Y, et al. Nuclear cataract caused by a lack of DNA degradation in the mouse eye lens. Nature. 2003;424(6952):1071-4.

100. Zhou Y, Xu Z, Liu Z. Impact of Neutrophil Extracellular Traps on Thrombosis Formation: New Findings and Future Perspective. Front Cell Infect Microbiol. 2022;12:910908.

101. Keyel PA. Dnases in health and disease. Dev Biol. 2017;429(1):1-11.

102. Baker KP, Baron WF, Henzel WJ, Spencer SA. Molecular cloning and characterization of human and murine DNase II. Gene. 1998;215(2):281-9.

103. Evans CJ, Aguilera RJ. DNase II: genes, enzymes and function. Gene. 2003;322:1-15.

104. Laskowski Sr. M. 12 Deoxyribonuclease I. In: Boyer PD, editor. The Enzymes. 4: Elsevier; 1971. p. 289-311.

105. Melgar E, Goldthwait DA. Deoxyribonucleic acid nucleases. II. The effects of metals on the mechanism of action of deoxyribonuclease I. J Biol Chem. 1968;243(17):4409-16.

106. Shiokawa D, Tanuma S. Characterization of human DNase I family endonucleases and activation of DNase gamma during apoptosis. Biochemistry. 2001;40(1):143-52.
107. Napirei M, Karsunky H, Zevnik B, Stephan H, Mannherz HG, Moroy T. Features of systemic lupus erythematosus in Dnase1-deficient mice. Nat Genet. 2000;25(2):177-81.
108. Napirei M, Ricken A, Eulitz D, Knoop H, Mannherz HG. Expression pattern of the deoxyribonuclease 1 gene: lessons from the Dnase1 knockout mouse. Biochem J. 2004;380(Pt 3):929-37.
109. Liu QY, Pandey S, Singh RK, Lin W, Ribecco M, Borowy-Borowski H, et al. DNaseY: a rat DNaseI-like gene coding for a constitutively expressed chromatin-bound endonuclease. Biochemistry. 1998;37(28):10134-43.
110. Shiokawa D, Ohyama H, Yamada T, Tanuma S. Purification and properties of DNase gamma from apoptotic rat thymocytes. Biochem J. 1997;326 (Pt 3):675-81.
111. Sisirak V, Sally B, D'Agati V, Martinez-Ortiz W, Ozcakar ZB, David J, et al. Digestion of Chromatin in Apoptotic Cell Microparticles Prevents Autoimmunity. Cell. 2016;166(1):88-101.
112. Wilber A, Lu M, Schneider MC. Deoxyribonuclease I-like III is an inducible macrophage barrier to liposomal transfection. Mol Ther. 2002;6(1):35-42.
113. Ozcakar ZB, Foster J, 2nd, Diaz-Horta O, Kasapcopur O, Fan YS, Yalcinkaya F, et al. DNASE1L3 mutations in hypocomplementemic urticarial vasculitis syndrome. Arthritis Rheum. 2013;65(8):2183-9.
114. Al-Mayouf SM, Sunker A, Abdwani R, Abrawi SA, Almurshedi F, Alhashmi N, et al. Loss-of-function variant in DNASE1L3 causes a familial form of systemic lupus erythematosus. Nat Genet. 2011;43(12):1186-8.
115. Almlof JC, Nystedt S, Leonard D, Eloranta ML, Grosso G, Sjowall C, et al. Whole-genome sequencing identifies complex contributions to genetic risk by variants in genes causing monogenic systemic lupus erythematosus. Hum Genet. 2019;138(2):141-50.
116. Hartl J, Serpas L, Wang Y, Rashidfarrokhi A, Perez OA, Sally B, et al. Autoantibody-mediated impairment of DNASE1L3 activity in sporadic systemic lupus erythematosus. J Exp Med. 2021;218(5).
117. Yasutomo K, Horiuchi T, Kagami S, Tsukamoto H, Hashimura C, Urushihara M, et al. Mutation of DNASE1 in people with systemic lupus erythematosus. Nat Genet. 2001;28(4):313-4.
118. Fuchs HJ, Borowitz DS, Christiansen DH, Morris EM, Nash ML, Ramsey BW, et al. Effect of aerosolized recombinant human DNase on exacerbations of respiratory symptoms and on pulmonary function in patients with cystic fibrosis. The Pulmozyme Study Group. N Engl J Med. 1994;331(10):637-42.
119. Harms HK, Matouk E, Tournier G, von der Hardt H, Weller PH, Romano L, et al. Multicenter, open-label study of recombinant human DNase in cystic fibrosis patients with moderate lung disease. DNase International Study Group. Pediatr Pulmonol. 1998;26(3):155-61.
120. Mainz JG, Schien C, Schiller I, Schadlich K, Koitschev A, Koitschev C, et al. Sinonasal inhalation of dornase alfa administered by vibrating aerosol to cystic fibrosis patients: a double-blind placebo-controlled cross-over trial. J Cyst Fibros. 2014;13(4):461-70.
121. Fisher J, Mohanty T, Karlsson CAQ, Khademi SMH, Malmstrom E, Frigyesi A, et al. Proteome Profiling of Recombinant DNase Therapy in Reducing NETs

and Aiding Recovery in COVID-19 Patients. Mol Cell Proteomics. 2021;20:100113.

122. Hendriks T, de Hoog M, Lequin MH, Devos AS, Merkus PJ. DNase and atelectasis in non-cystic fibrosis pediatric patients. Crit Care. 2005;9(4):R351-6.

123. McCord JJ, Engavale M, Masoumzadeh E, Villarreal J, Mapp B, Latham MP, et al. Structural features of Dnase1L3 responsible for serum antigen clearance. Commun Biol. 2022;5(1):825.

124. Napirei M, Ludwig S, Mezrhab J, Klockl T, Mannherz HG. Murine serum nucleases--contrasting effects of plasmin and heparin on the activities of DNase1 and DNase1-like 3 (DNase1l3). FEBS J. 2009;276(4):1059-73.

125. Shiokawa D, Shika Y, Tanuma S. Identification of two functional nuclear localization signals in DNase gamma and their roles in its apoptotic DNase activity. Biochem J. 2003;376(Pt 2):377-81.

126. Shak S, Capon DJ, Hellmiss R, Marsters SA, Baker CL. Recombinant human DNase I reduces the viscosity of cystic fibrosis sputum. Proc Natl Acad Sci U S A. 1990;87(23):9188-92.

127. Napirei M, Wulf S, Eulitz D, Mannherz HG, Kloeckl T. Comparative characterization of rat deoxyribonuclease 1 (Dnase1) and murine deoxyribonuclease 1-like 3 (Dnase1l3). Biochem J. 2005;389(Pt 2):355-64.

128. Nishikawa A, Shiokawa D, Umemori K, Hayashi H, Tanuma S. Occurrence of DNase gamma-like apoptotic endonucleases in hematopoietic cells in Xenopus laevis and their relation to metamorphosis. Biochem Biophys Res Commun. 1997;231(2):305-8.

129. Edler C, Schroder AS, Aepfelbacher M, Fitzek A, Heinemann A, Heinrich F, et al. Dying with SARS-CoV-2 infection-an autopsy study of the first consecutive 80 cases in Hamburg, Germany. Int J Legal Med. 2020;134(4):1275-84.

130. Mizuta R, Araki S, Furukawa M, Furukawa Y, Ebara S, Shiokawa D, et al. DNase gamma is the effector endonuclease for internucleosomal DNA fragmentation in necrosis. PLoS One. 2013;8(12):e80223.

131. Hemmers S, Teijaro JR, Arandjelovic S, Mowen KA. PAD4-mediated neutrophil extracellular trap formation is not required for immunity against influenza infection. PLoS One. 2011;6(7):e22043.

132. Aga E, Katschinski DM, van Zandbergen G, Laufs H, Hansen B, Muller K, et al. Inhibition of the spontaneous apoptosis of neutrophil granulocytes by the intracellular parasite Leishmania major. J Immunol. 2002;169(2):898-905.

133. Remy S, Chenouard V, Tesson L, Usal C, Menoret S, Brusselle L, et al. Generation of gene-edited rats by delivery of CRISPR/Cas9 protein and donor DNA into intact zygotes using electroporation. Sci Rep. 2017;7(1):16554.

134. Kim MJ, Ahituv N. The hydrodynamic tail vein assay as a tool for the study of liver promoters and enhancers. Methods Mol Biol. 2013;1015:279-89.

135. Wichmann D, Sperhake JP, Lutgehetmann M, Steurer S, Edler C, Heinemann A, et al. Autopsy Findings and Venous Thromboembolism in Patients With COVID-19: A Prospective Cohort Study. Ann Intern Med. 2020;173(4):268-77.

136. Hottz ED, Azevedo-Quintanilha IG, Palhinha L, Teixeira L, Barreto EA, Pao CRR, et al. Platelet activation and platelet-monocyte aggregate formation trigger tissue factor expression in patients with severe COVID-19. Blood. 2020;136(11):1330-41.

137. Manne BK, Denorme F, Middleton EA, Portier I, Rowley JW, Stubben C, et al. Platelet gene expression and function in patients with COVID-19. Blood. 2020;136(11):1317-29.

138. Worm M, Kohler EC, Panda R, Long A, Butler LM, Stavrou EX, et al. The factor XIIa blocking antibody 3F7: a safe anticoagulant with anti-inflammatory activities. Ann Transl Med. 2015;3(17):247.

139. Larsson M, Rayzman V, Nolte MW, Nickel KF, Bjorkqvist J, Jamsa A, et al. A factor XIIa inhibitory antibody provides thromboprotection in extracorporeal circulation without increasing bleeding risk. Sci Transl Med. 2014;6(222):222ra17.

140. Group RC, Horby P, Lim WS, Emberson JR, Mafham M, Bell JL, et al. Dexamethasone in Hospitalized Patients with Covid-19. N Engl J Med. 2021;384(8):693-704.

141. Bussani R, Schneider E, Zentilin L, Collesi C, Ali H, Braga L, et al. Persistence of viral RNA, pneumocyte syncytia and thrombosis are hallmarks of advanced COVID-19 pathology. EBioMedicine. 2020;61:103104.

142. Fox SE, Akmatbekov A, Harbert JL, Li G, Quincy Brown J, Vander Heide RS. Pulmonary and cardiac pathology in African American patients with COVID-19: an autopsy series from New Orleans. Lancet Respir Med. 2020;8(7):681-6.

143. Sanchez van Kammen M, Heldner MR, Brodard J, Scutelnic A, Silvis S, Schroeder V, et al. Frequency of Thrombocytopenia and Platelet Factor 4/Heparin Antibodies in Patients With Cerebral Venous Sinus Thrombosis Prior to the COVID-19 Pandemic. JAMA. 2021;326(4):332-8.

144. O'Brien XM, Biron BM, Reichner JS. Consequences of extracellular trap formation in sepsis. Curr Opin Hematol. 2017;24(1):66-71.

145. Deguine J, Barton GM. MyD88: a central player in innate immune signaling. F1000Prime Rep. 2014;6:97.

146. Kawai T, Adachi O, Ogawa T, Takeda K, Akira S. Unresponsiveness of MyD88-deficient mice to endotoxin. Immunity. 1999;11(1):115-22.

147. Evavold CL, Ruan J, Tan Y, Xia S, Wu H, Kagan JC. The Pore-Forming Protein Gasdermin D Regulates Interleukin-1 Secretion from Living Macrophages. Immunity. 2018;48(1):35-44 e6.

148. He WT, Wan H, Hu L, Chen P, Wang X, Huang Z, et al. Gasdermin D is an executor of pyroptosis and required for interleukin-1beta secretion. Cell Res. 2015;25(12):1285-98.

149. Hoppenbrouwers T, Autar ASA, Sultan AR, Abraham TE, van Cappellen WA, Houtsmuller AB, et al. In vitro induction of NETosis: Comprehensive live imaging comparison and systematic review. PLoS One. 2017;12(5):e0176472.

150. Fuchs TAJ-A, M.; Göbel, J.; Englert, H., inventor; Neutrolis Therapeutics, Inc., assignee. Engineered DNase Enzymes and Use in Therapy. US2019.

151. Panda R, Krieger T, Hopf L, Renne T, Haag F, Rober N, et al. Neutrophil Extracellular Traps Contain Selected Antigens of Anti-Neutrophil Cytoplasmic Antibodies. Frontiers in immunology. 2017;8:439.

152. Brill A, Fuchs TA, Savchenko AS, Thomas GM, Martinod K, De Meyer SF, et al. Neutrophil extracellular traps promote deep vein thrombosis in mice. J Thromb Haemost. 2012;10(1):136-44.

153. de Boer OJ, Li X, Teeling P, Mackaay C, Ploegmakers HJ, van der Loos CM, et al. Neutrophils, neutrophil extracellular traps and interleukin-17 associate with the organisation of thrombi in acute myocardial infarction. Thromb Haemost. 2013;109(2):290-7.

154. Ducroux C, Desilles JP, Ho-Tin-Noe B. Response by Ducroux et al to Letter Regarding Article, "Thrombus Neutrophil Extracellular Traps Content Impair tPA-Induced Thrombolysis in Acute Ischemic Stroke". Stroke. 2018;49(7):e266.

155. Farkas AZ, Farkas VJ, Gubucz I, Szabo L, Balint K, Tenekedjiev K, et al. Neutrophil extracellular traps in thrombi retrieved during interventional treatment of ischemic arterial diseases. Thromb Res. 2019;175:46-52.

156. Gould TJ, Vu TT, Swystun LL, Dwivedi DJ, Mai SH, Weitz JI, et al. Neutrophil extracellular traps promote thrombin generation through platelet-dependent and platelet-independent mechanisms. Arterioscler Thromb Vasc Biol. 2014;34(9):1977-84.

157. Folco EJ, Mawson TL, Vromman A, Bernardes-Souza B, Franck G, Persson O, et al. Neutrophil Extracellular Traps Induce Endothelial Cell Activation and Tissue Factor Production Through Interleukin-1alpha and Cathepsin G. Arterioscler Thromb Vasc Biol. 2018;38(8):1901-12.

158. Longstaff C, Varju I, Sotonyi P, Szabo L, Krumrey M, Hoell A, et al. Mechanical stability and fibrinolytic resistance of clots containing fibrin, DNA, and histones. J Biol Chem. 2013;288(10):6946-56.

159. Varju I, Longstaff C, Szabo L, Farkas AZ, Varga-Szabo VJ, Tanka-Salamon A, et al. DNA, histones and neutrophil extracellular traps exert anti-fibrinolytic effects in a plasma environment. Thromb Haemost. 2015;113(6):1289-98.

160. Chua RL, Lukassen S, Trump S, Hennig BP, Wendisch D, Pott F, et al. COVID-19 severity correlates with airway epithelium-immune cell interactions identified by single-cell analysis. Nat Biotechnol. 2020;38(8):970-9.

161. Liao M, Liu Y, Yuan J, Wen Y, Xu G, Zhao J, et al. Single-cell landscape of bronchoalveolar immune cells in patients with COVID-19. Nat Med. 2020;26(6):842-4.

162. Meizlish ML, Pine AB, Bishai JD, Goshua G, Nadelmann ER, Simonov M, et al. A neutrophil activation signature predicts critical illness and mortality in COVID-19. Blood Adv. 2021;5(5):1164-77.

163. Healy LD, Puy C, Itakura A, Chu T, Robinson DK, Bylund A, et al. Colocalization of neutrophils, extracellular DNA and coagulation factors during NETosis: Development and utility of an immunofluorescence-based microscopy platform. J Immunol Methods. 2016;435:77-84.

164. Vakili K, Fathi M, Pezeshgi A, Mohamadkhani A, Hajiesmaeili M, Rezaei-Tavirani M, et al. Critical complications of COVID-19: A descriptive meta-analysis study. Rev Cardiovasc Med. 2020;21(3):433-42.

165. Ackermann M, Verleden SE, Kuehnel M, Haverich A, Welte T, Laenger F, et al. Pulmonary Vascular Endothelialitis, Thrombosis, and Angiogenesis in Covid-19. N Engl J Med. 2020;383(2):120-8.

166. Middeldorp S, Coppens M, van Haaps TF, Foppen M, Vlaar AP, Muller MCA, et al. Incidence of venous thromboembolism in hospitalized patients with COVID-19. J Thromb Haemost. 2020;18(8):1995-2002.

167. Langer F, Kluge S, Klamroth R, Oldenburg J. Coagulopathy in COVID-19 and Its Implication for Safe and Efficacious Thromboprophylaxis. Hamostaseologie. 2020;40(3):264-9.

168. Llitjos JF, Leclerc M, Chochois C, Monsallier JM, Ramakers M, Auvray M, et al. High incidence of venous thromboembolic events in anticoagulated severe COVID-19 patients. J Thromb Haemost. 2020;18(7):1743-6.

169. Malas MB, Naazie IN, Elsayed N, Mathlouthi A, Marmor R, Clary B. Thromboembolism risk of COVID-19 is high and associated with a higher risk of mortality: A systematic review and meta-analysis. EClinicalMedicine. 2020;29:100639.

170. Patell R, Bogue T, Koshy A, Bindal P, Merrill M, Aird WC, et al. Postdischarge thrombosis and hemorrhage in patients with COVID-19. Blood. 2020;136(11):1342-6.

171. Investigators A, Investigators AC-a, Investigators R-C, Lawler PR, Goligher EC, Berger JS, et al. Therapeutic Anticoagulation with Heparin in Noncritically Ill Patients with Covid-19. N Engl J Med. 2021;385(9):790-802.

172. Investigators R-C, Investigators AC-a, Investigators A, Goligher EC, Bradbury CA, McVerry BJ, et al. Therapeutic Anticoagulation with Heparin in Critically Ill Patients with Covid-19. N Engl J Med. 2021;385(9):777-89.

173. Althaus K, Marini I, Zlamal J, Pelzl L, Singh A, Haberle H, et al. Antibody-induced procoagulant platelets in severe COVID-19 infection. Blood. 2021;137(8):1061-71.

174. Ranucci M, Ballotta A, Di Dedda U, Baryshnikova E, Dei Poli M, Resta M, et al. The procoagulant pattern of patients with COVID-19 acute respiratory distress syndrome. J Thromb Haemost. 2020;18(7):1747-51.

175. Teuwen LA, Geldhof V, Pasut A, Carmeliet P. Author Correction: COVID-19: the vasculature unleashed. Nat Rev Immunol. 2020;20(7):448.

176. Magro C, Mulvey JJ, Berlin D, Nuovo G, Salvatore S, Harp J, et al. Complement associated microvascular injury and thrombosis in the pathogenesis of severe COVID-19 infection: A report of five cases. Transl Res. 2020;220:1-13.

177. Skendros P, Mitsios A, Chrysanthopoulou A, Mastellos DC, Metallidis S, Rafailidis P, et al. Complement and tissue factor-enriched neutrophil extracellular traps are key drivers in COVID-19 immunothrombosis. J Clin Invest. 2020;130(11):6151-7.

178. Stavrou EX, Fang C, Bane KL, Long AT, Naudin C, Kucukal E, et al. Factor XII and uPAR upregulate neutrophil functions to influence wound healing. J Clin Invest. 2018;128(3):944-59.

179. Renne T, Stavrou EX. Roles of Factor XII in Innate Immunity. Front Immunol. 2019;10:2011.

180. van de Veerdonk FL, Kouijzer IJE, de Nooijer AH, van der Hoeven HG, Maas C, Netea MG, et al. Outcomes Associated With Use of a Kinin B2 Receptor Antagonist Among Patients With COVID-19. JAMA Netw Open. 2020;3(8):e2017708.

181. van de Veerdonk FL, Netea MG, van Deuren M, van der Meer JW, de Mast Q, Bruggemann RJ, et al. Kallikrein-kinin blockade in patients with COVID-19 to prevent acute respiratory distress syndrome. Elife. 2020;9.

182. Pereira LF, Marco FM, Boimorto R, Caturla A, Bustos A, De la Concha EG, et al. Histones interact with anionic phospholipids with high avidity; its relevance for the binding of histone-antihistone immune complexes. Clin Exp Immunol. 1994;97(2):175-80.

183. Lau J, Rousseau J, Kwon D, Benard F, Lin KS. A Systematic Review of Molecular Imaging Agents Targeting Bradykinin B1 and B2 Receptors. Pharmaceuticals (Basel). 2020;13(8).

184. de Maat S, de Mast Q, Danser AHJ, van de Veerdonk FL, Maas C. Impaired Breakdown of Bradykinin and Its Metabolites as a Possible Cause for Pulmonary Edema in COVID-19 Infection. Semin Thromb Hemost. 2020;46(7):835-7.

185. Angeli F, Zappa M, Reboldi G, Trapasso M, Cavallini C, Spanevello A, et al. The pivotal link between ACE2 deficiency and SARS-CoV-2 infection: One year later. Eur J Intern Med. 2021;93:28-34.

186. Mendes GMM, Do Nascimento IJB, Marazzi-Diniz PH, Da Silveira IB, Itaborahy MF, Viana LE, et al. The des-Arg(9)-bradykinin/B1R axis: Hepatic damage in COVID-19. Front Physiol. 2022;13:1080837.

187. Mina-Osorio P. The moonlighting enzyme CD13: old and new functions to target. Trends Mol Med. 2008;14(8):361-71.

188. Luan Y, Xu W. The structure and main functions of aminopeptidase N. Curr Med Chem. 2007;14(6):639-47.

189. Bawolak MT, Fortin JP, Vogel LK, Adam A, Marceau F. The bradykinin B2 receptor antagonist icatibant (Hoe 140) blocks aminopeptidase N at micromolar concentrations: off-target alterations of signaling mediated by the bradykinin B1 and angiotensin receptors. Eur J Pharmacol. 2006;551(1-3):108-11.

190. Xu Y, Wellner D, Scheinberg DA. Substance P and bradykinin are natural inhibitors of CD13/aminopeptidase N. Biochem Biophys Res Commun. 1995;208(2):664-74.

191. Middleton EA, He XY, Denorme F, Campbell RA, Ng D, Salvatore SP, et al. Neutrophil extracellular traps contribute to immunothrombosis in COVID-19 acute respiratory distress syndrome. Blood. 2020;136(10):1169-79.

192. Fuchs TA, Kremer Hovinga JA, Schatzberg D, Wagner DD, Lammle B. Circulating DNA and myeloperoxidase indicate disease activity in patients with thrombotic microangiopathies. Blood. 2012;120(6):1157-64.

193. Al-Kuraishy HM, Al-Gareeb AI, Al-Hussaniy HA, Al-Harcan NAH, Alexiou A, Batiha GE. Neutrophil Extracellular Traps (NETs) and Covid-19: A new frontiers for therapeutic modality. Int Immunopharmacol. 2022;104:108516.

194. Chen X, He WT, Hu L, Li J, Fang Y, Wang X, et al. Pyroptosis is driven by non-selective gasdermin-D pore and its morphology is different from MLKL channel-mediated necroptosis. Cell Res. 2016;26(9):1007-20.

195. Mulvihill E, Sborgi L, Mari SA, Pfreundschuh M, Hiller S, Muller DJ. Mechanism of membrane pore formation by human gasdermin-D. EMBO J. 2018;37(14).

196. Liu F, Ghimire L, Balasubramanian A, Hsu AY, Zhang Z, Yu H, et al. Neutrophil-specific depletion of gasdermin D does not protect against murine sepsis. Blood. 2023;141(5):550-4.

197. Yang X, Cheng X, Tang Y, Qiu X, Wang Y, Kang H, et al. Bacterial Endotoxin Activates the Coagulation Cascade through Gasdermin D-Dependent Phosphatidylserine Exposure. Immunity. 2019;51(6):983-96 e6.

198. Su M, Chen C, Li S, Li M, Zeng Z, Zhang Y, et al. Gasdermin D-dependent platelet pyroptosis exacerbates NET formation and inflammation in severe sepsis. Nat Cardiovasc Res. 2022;1(8):732-47.

199. D'Cruz AA, Speir M, Bliss-Moreau M, Dietrich S, Wang S, Chen AA, et al. The pseudokinase MLKL activates PAD4-dependent NET formation in necroptotic neutrophils. Sci Signal. 2018;11(546).

200. Desai J, Kumar SV, Mulay SR, Konrad L, Romoli S, Schauer C, et al. PMA and crystal-induced neutrophil extracellular trap formation involves RIPK1-RIPK3-MLKL signaling. Eur J Immunol. 2016;46(1):223-9.

201. Schreiber A, Rousselle A, Becker JU, von Massenhausen A, Linkermann A, Kettritz R. Necroptosis controls NET generation and mediates complement activation, endothelial damage, and autoimmune vasculitis. Proc Natl Acad Sci U S A. 2017;114(45):E9618-E25.

202. Kolbrink B, Riebeling T, Kunzendorf U, Krautwald S. Plasma Membrane Pores Drive Inflammatory Cell Death. Front Cell Dev Biol. 2020;8:817.

203. Chen H, Li Y, Wu J, Li G, Tao X, Lai K, et al. RIPK3 collaborates with GSDMD to drive tissue injury in lethal polymicrobial sepsis. Cell Death Differ. 2020;27(9):2568-85.
204. Yoo H, Im Y, Ko RE, Lee JY, Park J, Jeon K. Association of plasma level of high-mobility group box-1 with necroptosis and sepsis outcomes. Sci Rep. 2021;11(1):9512.
205. Neubert E, Meyer D, Rocca F, Gunay G, Kwaczala-Tessmann A, Grandke J, et al. Chromatin swelling drives neutrophil extracellular trap release. Nat Commun. 2018;9(1):3767.
206. de Bont CM, Koopman WJH, Boelens WC, Pruijn GJM. Stimulus-dependent chromatin dynamics, citrullination, calcium signalling and ROS production during NET formation. Biochim Biophys Acta Mol Cell Res. 2018;1865(11 Pt A):1621-9.
207. Konig MF, Abusleme L, Reinholdt J, Palmer RJ, Teles RP, Sampson K, et al. Aggregatibacter actinomycetemcomitans-induced hypercitrullination links periodontal infection to autoimmunity in rheumatoid arthritis. Sci Transl Med. 2016;8(369):369ra176.
208. Lewis HD, Liddle J, Coote JE, Atkinson SJ, Barker MD, Bax BD, et al. Inhibition of PAD4 activity is sufficient to disrupt mouse and human NET formation. Nat Chem Biol. 2015;11(3):189-91.
209. Saha P, Yeoh BS, Xiao X, Golonka RM, Singh V, Wang Y, et al. PAD4-dependent NETs generation are indispensable for intestinal clearance of Citrobacter rodentium. Mucosal Immunol. 2019;12(3):761-71.
210. Silva JC, Rodrigues NC, Thompson-Souza GA, Muniz VS, Neves JS, Figueiredo RT. Mac-1 triggers neutrophil DNA extracellular trap formation to Aspergillus fumigatus independently of PAD4 histone citrullination. J Leukoc Biol. 2020;107(1):69-83.
211. Vorobjeva NV. Neutrophil Extracellular Traps: New Aspects. Moscow Univ Biol Sci Bull. 2020;75(4):173-88.
212. Claushuis TAM, van der Donk LEH, Luitse AL, van Veen HA, van der Wel NN, van Vught LA, et al. Role of Peptidylarginine Deiminase 4 in Neutrophil Extracellular Trap Formation and Host Defense during Klebsiella pneumoniae-Induced Pneumonia-Derived Sepsis. J Immunol. 2018;201(4):1241-52.
213. Thiam HR, Wong SL, Qiu R, Kittisopikul M, Vahabikashi A, Goldman AE, et al. NETosis proceeds by cytoskeleton and endomembrane disassembly and PAD4-mediated chromatin decondensation and nuclear envelope rupture. Proc Natl Acad Sci U S A. 2020;117(13):7326-37.
214. Kusunoki Y, Nakazawa D, Shida H, Hattanda F, Miyoshi A, Masuda S, et al. Peptidylarginine Deiminase Inhibitor Suppresses Neutrophil Extracellular Trap Formation and MPO-ANCA Production. Front Immunol. 2016;7:227.
215. Martinod K, Demers M, Fuchs TA, Wong SL, Brill A, Gallant M, et al. Neutrophil histone modification by peptidylarginine deiminase 4 is critical for deep vein thrombosis in mice. Proc Natl Acad Sci U S A. 2013;110(21):8674-9.
216. Amin R, Subbarao P, Lou W, Jabar A, Balkovec S, Jensen R, et al. The effect of dornase alfa on ventilation inhomogeneity in patients with cystic fibrosis. Eur Respir J. 2011;37(4):806-12.
217. Sawicki GS, Chou W, Raimundo K, Trzaskoma B, Konstan MW. Randomized trial of efficacy and safety of dornase alfa delivered by eRapid nebulizer in cystic fibrosis patients. J Cyst Fibros. 2015;14(6):777-83.
218. Yang C, Chilvers M, Montgomery M, Nolan SJ. Dornase alfa for cystic fibrosis. Cochrane Database Syst Rev. 2016;4:CD001127.

219. Tetz V, Tetz G. Effect of deoxyribonuclease I treatment for dementia in end-stage Alzheimer's disease: a case report. J Med Case Rep. 2016;10(1):131.

220. Patel A, Harrison E, Durward A, Murdoch IA. Intratracheal recombinant human deoxyribonuclease in acute life-threatening asthma refractory to conventional treatment. Br J Anaesth. 2000;84(4):505-7.

221. Bobek V, Majewski A, Kolostova K, Rzechonek A, Lischke R, Schutzner J, et al. Intrapleural administration of DNase alone for pleural empyema. Int J Clin Exp Med. 2015;8(11):22011-5.

222. Holliday ZM, Earhart AP, Alnijoumi MM, Krvavac A, Allen LH, Schrum AG. Non-Randomized Trial of Dornase Alfa for Acute Respiratory Distress Syndrome Secondary to Covid-19. Front Immunol. 2021;12:714833.

223. Toma A, Darwish C, Taylor M, Harlacher J, Darwish R. The Use of Dornase Alfa in the Management of COVID-19-Associated Adult Respiratory Distress Syndrome. Crit Care Res Pract. 2021;2021:8881115.

224. Simpson G, Roomes D, Heron M. Effects of streptokinase and deoxyribonuclease on viscosity of human surgical and empyema pus. Chest. 2000;117(6):1728-33.

225. Durward A, Forte V, Shemie SD. Resolution of mucus plugging and atelectasis after intratracheal rhDNase therapy in a mechanically ventilated child with refractory status asthmaticus. Crit Care Med. 2000;28(2):560-2.

226. Davis JC, Jr., Manzi S, Yarboro C, Rairie J, McInnes I, Averthelyi D, et al. Recombinant human Dnase I (rhDNase) in patients with lupus nephritis. Lupus. 1999;8(1):68-76.

227. Macanovic M, Sinicropi D, Shak S, Baughman S, Thiru S, Lachmann PJ. The treatment of systemic lupus erythematosus (SLE) in NZB/W F1 hybrid mice; studies with recombinant murine DNase and with dexamethasone. Clin Exp Immunol. 1996;106(2):243-52.

228. Alcazar-Leyva S, Ceron E, Masso F, Montano LF, Gorocica P, Alvarado-Vasquez N. Incubation with DNase I inhibits tumor cell proliferation. Med Sci Monit. 2009;15(2):CR51-5.

229. Sugihara S, Yamamoto T, Tanaka H, Kambara T, Hiraoka T, Miyauchi Y. Deoxyribonuclease treatment prevents blood-borne liver metastasis of cutaneously transplanted tumour cells in mice. Br J Cancer. 1993;67(1):66-70.

230. Tokita K, Sugihara S, Hiraoka T, Miyauchi Y, Kambara T, Yamamoto T. Effects of serine protease and deoxyribonuclease on intravascular tumor cell arrest in rat blood-borne lung metastasis. Invasion Metastasis. 1995;15(1-2):46-59.

231. Linardou H, Epenetos AA, Deonarain MP. A recombinant cytotoxic chimera based on mammalian deoxyribonuclease-I. Int J Cancer. 2000;86(4):561-9.

232. Kater A, Henke MO, Rubin BK. The role of DNA and actin polymers on the polymer structure and rheology of cystic fibrosis sputum and depolymerization by gelsolin or thymosin beta 4. Ann N Y Acad Sci. 2007;1112:140-53.

233. Ulmer JS, Herzka A, Toy KJ, Baker DL, Dodge AH, Sinicropi D, et al. Engineering actin-resistant human DNase I for treatment of cystic fibrosis. Proc Natl Acad Sci U S A. 1996;93(16):8225-9.

234. Manderson AP, Carlucci F, Lachmann PJ, Lazarus RA, Festenstein RJ, Cook HT, et al. The in vivo expression of actin/salt-resistant hyperactive DNase I inhibits the development of anti-ssDNA and anti-histone autoantibodies in a murine model of systemic lupus erythematosus. Arthritis Res Ther. 2006;8(3):R68.

235. Mouchess M SE, Chan S, Bingbing D, Tam C, Cao Y, et al. A rationally engineered DNase1-Fc fusion protein ameliorates autoimmune glomerulonephritis. J Immunol. 2019;202(1).

236. De Meyer SF, Suidan GL, Fuchs TA, Monestier M, Wagner DD. Extracellular chromatin is an important mediator of ischemic stroke in mice. Arteriosclerosis, thrombosis, and vascular biology. 2012;32(8):1884-91.

237. Pena-Martinez C, Duran-Laforet V, Garcia-Culebras A, Ostos F, Hernandez-Jimenez M, Bravo-Ferrer I, et al. Pharmacological Modulation of Neutrophil Extracellular Traps Reverses Thrombotic Stroke tPA (Tissue-Type Plasminogen Activator) Resistance. Stroke. 2019;50(11):3228-37.

10. Statement of contribution by others

Experiments for the publication "Defective NET clearance contributes to sustained FXII activation in COVID-19-associated pulmonary thrombo-inflammation" were performed together with Dr. Chandini Rangaswamy (shared first authorship). Proteomics measurements of COVID-19 plasma and lung tissue presented here were performed by Dr. Christoph Krisp. Microscopic imaging of COVID-19 and VITT lungs was partly performed by Dr. Maike Frye. The anti-FXII immunoblot of COVID-19 plasma was performed by Sandra Konrath, MSc. Measurements of circulating extracellular DNA, H3cit and MPO levels in serum of VITT patients were performed by Dr. Chandini Rangaswamy.

Injections, scoring, and organ retrieval of mice subjected to septicemia and sterile neutrophilia (2nd results part) were performed together with Dr. Mylène Divivier, Dr. Chandini Rangaswamy, and Josephine Göbel. Murine lungs were paraffin-embedded, sectioned, and H&E-stained by Kristin Hartmann (Mouse Pathology Core Facility, UKE). Irm Hermans-Borgmeyer and Uwe Borgmeyer (Center for Molecular Neurobiology, UKE) generated the CRISPR-Cas9 knockout mouse *Gsdmd/D1/D1l3$^{-/-}$*.

11. List of peer-reviewed publications and patents

5) **Englert, H.**, Göbel, J., Khong, D., Omidi, M., Wolska, N., Konrath, S., Frye, M, Mailer, R. K., Beerens, M., Gerwers, J. C., Preston, R. J. S., Odeberg, J., Butler, L. M., Maas, C., Stavrou, E. X., Fuchs, T. A., Renné, T. *Targeting NETs using dual-active DNase1 variants*. Front. Immunol. 2023 May;14:1181761. doi: 10.3389/fimmu.2023.1181761.

6) Konrath, S., Mailer, R. K., Beerens, M., **Englert, H.**, Frye, M., Kuta, P., Preston, R. J. S., Maas, C., Butler, L. M., Roest, M., de Laat, B., Renné, T. *Intrinsic coagulation pathway-mediated thrombin generation in mouse whole blood*. Front Cardiovasc Med. 2022 Nov;9:1008410. doi: 10.3389/fcvm.2022.1008410.

7) Plochg, B. F. J., **Englert, H.**, Rangaswamy, C., Konrath, S., Malle, M., Lampalzer, S., Beisel, C., Wollin, S., Frye, M., Aberle, J., Kluwe, J., Renné, T., Mailer, R. K. *Liver damage promotes pro-inflammatory T-cell responses against apolipoprotein B-100*. J Intern Med. 2022 May;291(5):648-664. doi: 10.1111/joim.13434.

8) Wallis, S., Wolska, N., **Englert, H.**, Posner, M., Upadhyay, A., Renné, T., Eggleston, I., Bagby, S., Pula, G. *A peptide from the staphylococcal protein Efb binds P-selectin and inhibits the interaction of platelets with leukocytes*. J Thromb Haemost. 2022 Mar;20(3):729-741. doi: 10.1111/jth.15613.

9) Greinacher, A., Selleng, K., Palankar, R., Wesche, J., Handtke, S., Wolff, M., Aurich, K., Lalk, M., Methling, K., Völker, U., Hentschker, C., Michalik, S., Steil, L., Reder, A., Schönborn, L., Beer, M., Franzke, K., Büttner, A., Fehse, B., Stavrou, E. X., Rangaswamy, C., Mailer, R. K., **Englert, H.**, Frye, M., Thiele, T., Kochanek, S., Krutzke, L., Siegerist, F., Endlich, N., Warkentin, T. E., Renné, T. *Insights in ChAdOx1 nCoV-19 vaccine-induced immune thrombotic thrombocytopenia*. Blood. 2021 Dec 2;138(22):2256-2268. doi: 10.1182/blood.2021013231.

10) Fogarty, H., Townsend, L., Morrin, H., Ahmad, A., Comerford, C., Karampini, E., **Englert, H.**, Byrne, M., Bergin, C., O'Sullivan, J. M., Martin-Loeches, I., Nadarajan, P., Bannan, C., Mallon, P. W., Curley, G. F., Preston, R. J. S., Rehill, A. M., McGonagle, D., Ni Cheallaigh, C., Baker, R. I., Renné, T., Ward, S. E., O'Donnell, J. S., Irish COVID-19 Vasculopathy Study (iCVS) investigators. *Persistent*

endotheliopathy in the pathogenesis of long COVID syndrome. J Thromb Haemost. 2021 Oct;19(10):2546-2553. doi: 10.1111/jth.15490.

11) **<u>Englert, H.</u>**, Rangaswamy, C., Deppermann, C., Sperhake, J. P., Krisp, C., Schreier, D., Gordon, E., Konrath, S., Haddad, M., Pula, G., Mailer, R. K., Schlüter, H., Kluge, S., Langer, F., Püschel, K., Panousis, K., Stavrou, E. X., Maas, C., Renné, T., Frye, M. *Defective NET clearance contributes to sustained FXII activation in COVID-19-associated pulmonary thrombo-inflammation.* EBioMedicine. 2021 May;67:103382. doi: 10.1016/j.ebiom.2021.103382.

12) Rangaswamy, C., Mailer, R. K., **<u>Englert, H.</u>**, Konrath, S., Renné, T. *The contact system in liver injury.* Semin Immunopathol. 2021 Aug;43(4):507-517. doi: 10.1007/s00281-021-00876-7.

13) Rangaswamy, C., **<u>Englert, H.</u>**, Deppermann, C., Renné, T. *Polyanions in Coagulation and Thrombosis: Focus on Polyphosphate and Neutrophils Extracellular Traps.* J Thromb Haemost. 2021 Aug;121(8):1021-1030. doi: 10.1055/a-1336-0526.

14) Fuchs, T. A., Jiménez-Alcázar, M., Göbel, J., **<u>Englert, H</u>**. Engineered DNase Enzymes and Use in Therapy. 2019. Neutrolis, Inc. US patent application US WO2019/036719 A2, international publication date 21 February 2019.

12. Acknowledgements

13. Curriculum Vitae

Education

PhD Student   **Mar 2018 – present**

University Medical Center Hamburg, Institute for Clinical Chemistry and Laboratory Medicine – Hamburg, Germany

MSc in Biomedical Sciences   **Sep 2014 – Oct 2016**

VU University Amsterdam – Amsterdam, The Netherlands

• Specializations: 1. Immunology 2. Management, Policy Analysis, and Entrepreneurship in Health and Life Sciences

BSc in Biochemistry and Cell Biology   **Sep 2011 – June 2014**

Jacobs University Bremen – Bremen, Germany

• BSc thesis rotation in microbiology and microbial biotechnology labs

Abitur / High School Diploma   **June 2011**

IGS-Mainz Bretzenheim – Mainz, Germany

• Student exchange at Duchess Park High School, Prince George, BC, Canada, 2007

Relevant Experience

Freelance Consultant   **Mar 2018 – June 2019**

Neutrolis - Cambridge, Massachusetts, United States

• Laboratory research on the development of recombinant DNase variants as well as preparation of company and investor decks

Business Analyst   **Oct 2016 – Feb 2018**

Catenion GmbH – Berlin, Germany

• International management consultancy devoted to developing competitive R&D strategies for pharma and biotech

• Leading approaches to key aspects of R&D strategy such as asset and indication analyses, risk assessments, due diligence, M&A, and drug portfolio management

Global Medical Affairs Intern   **Feb 2016 – Aug 2016**

Bayer Pharma AG, Global Medical Affairs, Pulmonary Hypertension – Berlin, Germany

• Optimization of medical, legal, and regulatory documents for Riociguat (Adempas); organization of Medical Science Liaison (MSL) newsletter, meetings and congresses

Research Intern   **Feb 2015 – July 2015**

University Medical Center Hamburg, Institute for Clinical Chemistry and Laboratory Medicine – Hamburg, Germany

• Design of novel biomarker assay based on neutrophil cell death-specific proteome

Conferences

• International Symposium Neutrophil from 3 – 6 December 2022, Mexico City, Mexico

• 30th Congress of the International Society on Thrombosis and Haemostasis (ISTH) from 9 – 13 July 2022, in London, England, UK

• 66th Annual Meeting of the Society of Thrombosis and Haemostasis Research (GTH e.V.) from 1 – 4 March 2022, in Leipzig, Germany

• International Symposium Neutrophil from 31 May – 1 June 2021, Online Meeting Conference

• 5th International Synthetic & Systems Biology Summer School from 25 – 29 July 2018, in Siena, Tuscany, Italy

Fellowships and Volunteering

• Deutsche Forschungsgesellschaft (DFG) -founded PhD research (as a part of the clinical research unit 306/CRU 306)

• Recipient of a student scholarship (Sep 2012 – Sep 2016) from the German scholarship foundation Friedrich-Naumann-Stiftung für die Freiheit for academic excellence and social commitment

• MIN Welcome Buddy mentor for international PhD students at Uni Hamburg PIASTA (since July 2019)

Languages

German – native speaker, **English** – fluent, **Dutch** - conversational

14. Eidesstattliche Versicherung

Ich versichere ausdrücklich, dass ich die Arbeit selbständig und ohne fremde Hilfe verfasst, andere als die von mir angegebenen Quellen und Hilfsmittel nicht benutzt und die aus den benutzten Werken wörtlich oder inhaltlich entnommenen Stellen einzeln nach Ausgabe (Auflage und Jahr des Erscheinens), Band und Seite des benutzten Werkes kenntlich gemacht habe.

Ferner versichere ich, dass ich die Dissertation bisher nicht einem Fachvertreter an einer anderen Hochschule zur Überprüfung vorgelegt oder mich anderweitig um Zulassung zur Promotion beworben habe.

Ich erkläre mich einverstanden, dass meine Dissertation vom Dekanat der Medizinischen Fakultät mit einer gängigen Software zur Erkennung von Plagiaten überprüft werden kann.

Unterschrift: ....